Response to Referee comments for acp-2021-420

A climatology of trade-wind cumulus cold pools and their link to mesoscale cloud organization, by Raphaela Vogel, Heike Konow, Hauke Schulz, and Paquita Zuidema

We thank the three referees for their insightful comments and their positive evaluation of our manuscript. The referees raise a few important issues that we are happy to learn about and to address in our revision. The specific comments of the referees are addressed step-by-step below, with our responses inserted in red font.
Additional comments from referees 1 & 2 in the annotated manuscript are added as supplement. Please note that we also included a tracked-changes version of the manuscript, with the changes indicated in blue and red (for crossed out sentences).

Anonymous Referee #1

Very detailed analysis of valuable observations of cold pools in trade wind regions. I appreciate the extensive analysis, combining different measurements and allowing to compare and link cloud properties to cold pool properties. I find however, this last point could be strengthened more.

Main critique points:

1. a bit more answering the "why" about correlations found, especially between cloud cover statistics and cold pool properties in conclusion would make the study more valuable (reference to theoretical or simulation studies).
Throughout the results and discussion sections, we added more discussion and physical interpretation of the relationships and correlations found, also in response to the specific questions in the annotated manuscript. We also relate our results more thoroughly to the previous literature on tropical oceanic cold pools, and formulate more specific hypotheses.

Regarding the variation of cloud statistics with the cold pool characteristics, we now state more explicit hypotheses regarding the connection between cold-pool strength and proximity to the potential parent convection:
"Overall, Figure 4 indicates that clouds and rain are nearer tmin in the strongest cold pools, and nearer tmax for the weakest cold pools. A potential explanation for this observation is that stronger cold pools are running further ahead of their stronger parent convection, while the weaker parent convection of the weaker cold pools might have already dissipated. [...]."

Another example is that we added a comparison to cloud-base updraft vertical velocities from the literature to argue that the gust-front vertical velocities are very likely strong enough to trigger new convection (see also main comment 6).

2. The point that cold pools are responsible for extending the daily cycle of shallow convection into the afternoon is made very prominent (abstract, result section, conclusions). However I am missing some more mechanistic explanation here. I cannot really follow the reasoning in Sec. 3.3, since the precipitation reference cited does not exclude cold pool effects. Can you extend a bit more here? Are you inferring that the cold pools are strong enough to trigger new convection later in the day (as in deep convection regions) or are you rather saying that the cold pools slow down convection and thereby stretch the convectively active time period over a longer time due to their inhibitive effects?
We argue that cold pools help extend the diel cycle of shallow convection through the triggering of new convection later in the day. As clarified in the revised manuscript, we think

that our cold pools are strong enough to trigger new convection and subsequent cold pools into the early afternoon (see also comment 6 below). We clarified this paragraph as follows:

"The period of enhanced cold-pool occurrence between 23-15 LT and its peak at 14 LT extend much further into the day compared to the period of enhanced mean background rain rate between about 03-06 LT during RICO and EUREC4A (Nuijens et al. 2009, Radtke et al. 2021), suggesting that cold pools help extend the diel cycle of shallow convection into the early afternoon. Also the diel cycle of cloud cover seems to be slightly extended in cold-pool periods, with CCtot decreasing below the diel mean about 4 h later compared to the climatological CC. The likely reason for the extension of convection into the afternoon is that the cold pools are successful in triggering new convection, which can again induce new cold pools that trigger further convection. Thereby, cold pools reinforce each other, which is supported by the shorter median interval between subsequent cold pools of 121 min between 07-14 LT compared to 182 min between 22-04 LT.

The importance of cold pools in triggering new convection is well established in the literature and can occur through mechanic lifting or moisture accumulations, both of which are favoured when multiple cold pools collide (Rotunno et al., 1988; Tompkins, 2001; Feng et al., 2015; Torri and Kuang, 2019; Meyer and Haerter, 2020). Rochetin et al. (2021) also found a diel cycle of cold-pool occurrence near Barbados in realistic LES with the ICON model at 2.5 km grid spacing, however, without the pronounced extension into the afternoon observed at BCO (see their Figure 16D). This might be due to gust front vertical velocities being poorly-resolved at kilometre-scale resolutions, which leads to too little convective triggering and deficits in rain and convective organization as simulations over Germany show (Hirt and Craig, 2021)."

3. Cold pool detection: it seems that the algorithm detects also very long-lasting temperature deviations that are more likely connected to meso-scale cold fronts than cold pools (Fig 2., Fish). How did you make sure that no frontal temperature drops were detected as cold pools? Did such outliers only occur in connection with the Fish pattern? Please also extend a bit on how these outliers could be avoided in your algorithm?
It is true that the Fish pattern is tightly linked to trailing cold fronts of extratropical origins (Aemisegger et al., 2021; Schulz et al., 2021), and the cold pools in the Fish case also have a more frontal character with longer-lasting showers and downdrafts compared to the other patterns. However, also in the case of the Fish cold pools, we think the temperature drop is mostly associated with the evaporating precipitation that drives strong downdrafts (and not with cold-air advection), and thus in line with our cold-pool definition and comparable to the other cold pools. In the example case of Figure 2, this is evident from the quickly recovering temperature as soon as the rain associated with the first cold pool stopped. We therefore see it as benefit of the algorithm that such Fish cold pools are reliably detected, an impression that is also shared by the second referee.
Nevertheless, we cannot exclude that the frontal system contributed slightly to the temperature difference, and the adjusted discussion of the Fish example case is as follows:

"The Fish day features a 6h long cold pool associated with steady and intense rain (maximum RR of 11.6mmh−1), continued strong downdrafts and very large humidity throughout its entire duration. The temperature fully recovers within about 20 min of the cold-pool end, and 3 h later two subsequent pronounced cold pools follow that are again characterized by continued precipitation and downdrafts. The satellite image shows the fish-bone like cloud band typically associated with the Fish pattern, which is strongly connected to trailing cold fronts of extratropical origins (Aemisegger et al., 2021; Schulz et al., 2021). The more front-like character of the Fish cold pools with steady showers and downdrafts is clearly evident. ***While most of the cooling is expected to stem from the evaporating precipitation, we cannot rule out a small cooling contribution related to a larger-scale temperature contrast between South and North of the Fish cloud band (see also Schulz et al., 2021).***"

When we tested the algorithm, we found that the requirement of an abrupt temperature is usually enough to exclude cases of more slowly decreasing temperature associated with fronts. And while we didn't check all cases, we do think that such outliers are limited to the Fish pattern.

4. Both the result and conclusion sections lack some background information regarding hypotheses and motivation about the choice of observables and tested correlations (e.g., testing the variation of cold pool properties with other variables, such as CTH).
We answered this comment together with main comment 1, please refer to this answer for comment 4.

5. The Result section about cold pool properties conditioned on the different cloud types should be rewritten, since it's a bit hard to read (sentence structure).
We restructured the discussion of Figure 4 and more explicitly distinguish the different cloud type classifications discussed (e.g. LCL vs. precipitating cloud segments). As we also clarified certain ambiguities with definitions of the cloud variables, the discussion should now be more accessible.

6. Convection triggering: I would appreciate some general reflection on whether you think that the measured weak updrafts (strengths of below 1m/s) that travel with the cold pool front (i.e., are not stationary) are sufficient to trigger convection?
The gust-front vertical velocities found in this study are much larger compared to the average cloud-base (updraft) vertical velocities associated with trade cumuli (e.g. as published by Sakradzija and Klingebiel 2020 or Klingebiel et al. 2021 based on BCO Doppler radar observations). We don't think that the missing stationarity is an issue for the triggering, as there is always a strong background flow in the trades and the fronts nevertheless represent coherent features that are sustained for some time.
We thus expect the cold pools to be sufficient to trigger new convection at the front. We added a few sentences to clarify this:

"The median w_max450 at the gust front edge (see Table 1) is with 1 m s−1 much larger than the averaged hourly in-cloud vertical velocities near cloud base measured by the BCO Doppler radar, which has a peak density at 0.2 m s−1 and maxima of 0.6 m s−1 (Klingebiel et al., 2021). 1 m s−1 also marks the upper tail of cloud-base averaged updraft vertical velocities (see Figure 4b of Sakradzija and Klingebiel, 2020). This suggests that the gust-front vertical velocity maxima are very relevant for triggering new convection in the trade cumulus regime. "

7. Section 4 is a very interesting section, since the cold pool properties conditioned on the mesoscale situation is the main new part in this study. The text is however difficult to read, some simplifying sentence structure would be beneficial, mostly l. 435 ff. The text would further benefit from being purely descriptive relating the conditional statistics to the cloud properties of the respective patterns. E.g., how is the lower cold pool fraction of Gravel compared to Flower related to the cloud and cold pool properties in the two situations? Try to connect the different panels in Figure 7.
We completely restructured the paragraphs discussing Figures 7 and 8 to focus on the most important results and to omit details that could distract the reader. We also moved the paragraphs discussing the four example days to Section 2.5.

Furthermore, we add some more explanations relating the patterns-specific cloud and cold pool properties:
"The climatological differences in CTH of the patterns correspond very well with their differences in the cold-pool fraction (Figure 7b), with Sugar having clearly the shallowest mean C T H and the lowest cold-pool fraction, separated by a step-change from Gravel, followed closely by Flowers and Fish. The two patterns with the largest cold-pool fraction, Fish and

Flowers, also have the largest mean cloud object sizes (Bony et al., 2020), suggesting that cloud size and cold-pool occurrence are positively correlated (Schlemmer and Hohenegger, 2014).”

Comments to Sections:

1. Introduction:

- missing: difference climatology (overview) winter vs. summer trades

We know explicitly mention that we focus most of the analyses on the winter season, and added the following sentence at the end of the second-from-last paragraph:

“To focus on trade cumulus cold pools, we limit most of our analysis to the winter regime from December to April, as in summer the intertropical convergence zone is often close to Barbados and convection is much deeper (Brueck et al. 2015).”

- review about cold pools in shallow convection a bit short: there are more papers that should be cited and summarised (e.g., Glassmeier and Feingold, 2017)

Apart from more through coparisons to the literature throughout the manuscript (see answer to main comment 1), we also included more stratocumulus papers in the introduction, focusing on the relationship of cold pools/rain and the mesoscale organization pattern. The third paragraph of the introduction now reads:

“For the pattern Fish with its very large-scale fish-bone structures that are tightly linked to extratropical dry intrusions (Aemisegger et al., 2021; Schulz et al., 2021), cold pools are likely to give the cloudy part its skeletal structure, while the overall system is forced by the large-scale dynamics into its linear alignment. ***Observations of drizzling stratocumulus often show cold pools being dragged along with a larger system without initiating its mesoscale organization (Wilbanks et al., 2015).*** *Contrastingly, for the Gravel pattern, the large-scale influence may be less important and also more homogeneous. Thus, cold pools likely play an important role in creating and maintaining this pattern****, similar to the strong influence of rain (and indirectly also cold pools) on the transition from closed- to open-cell stratocumulus (Xue et al., 2008; Wang and Feingold, 2009; Glassmeier and Feingold, 2017).*** *Before we can understand the different roles that cold pools play in these patterns, we need to understand whether and how cold-pool characteristics differ among them.”*

2. Methodology:

- Some ambiguities with definitions of cloud variables (see comments in text)

We clarified these ambiguities in the text, together with similar comments from referee 2. See also our answers to these comments in the annotated manuscript.

- How are the “overall” cloud variables defined: as the mean over all pixels in a cloud entity? Please clarify.

We applied many changes to this paragraph and we now only mention the overall cloud-base height (cbh_{ID}), which refers to the lowest cloud-base height of a cloud object. We changed the sentence in question as follows:

“To focus on clouds connected to the trade-wind layer, only cloud objects with a lowest cloud-base height (cbh_{ID}) smaller than 4 km are considered in the analysis.”

- There is some confusion about the definition of CBH: is it a time series, indicating the cloud base height of the lowest cloud at each time step (this is how I understand the definition on l. 96), which however stands in contrast to using the “lowest CBH” as stated in the legend of Figure 2?

Yes, CBH is a timeseries indicating the height of the lowest cloudy pixel of a 1-min averaged radar profile. The same is true for the first part of the Gravel day in Figure 2, with the exception

that the data used is from the ceilometer in this case (as the radar wasn't running). We changed the legend to:
"On the Gravel day the radar did not work prior to 12 LT and the first ceilometer cloud base (CBH_1) is shown instead."

- vertical velocity (l. 117): are these pixel-by-pixel values or mean values over one radar profile or timeseries?

These are 1-min averaged values over several lidar profiles. We clarified as follows:
"We derive 1-min timeseries of both the average vertical velocity in the sub-cloud layer..."

- What is morphological closing?

Morphological closing is an image processing method that removes noise e.g. due to measurement interruptions.
The sentence is clarified by adding some more context:
[..] morphological closing is applied to remove noise from measurement interruptions.

- Splitting of cloud cover: Based on what are the threshold values for CBH chosen? Based on what is this distinction made, I assume the overall cloud variables and not the pixel-by-pixel cloud base? Can you give some more details?

We use the same thresholds as in Nuijens et al. 2014 and Klingebiel et al. 2021 to distinguish precipitating clouds from LCL clouds and clouds further aloft. The distinction is made based on the profile-by-profile cloud base in the main text. In Appendix A, we also show the same split up based on the overall cbh_ID, which adds complementary information.

We added a bit more detail and restructured the sentences to:

"Following Nuijens et al. (2014), CC is further split up into contributions from cloud segments with different CBH, which represent cloudiness near the lifting-condensation level (CClcl; 300 m < CBH ≤ 1 km), and cloudiness aloft such as stratiform layers or edges of deeper cumuli (CCaloft; 1 km < CBH ≤ 4 km). We also introduce a third category of precipitating cloud segments if CBH ≤ 300 m (CCprcp, same threshold as in Klingebiel et al., 2021). A given 1-min HF profile can only count to one of the three categories, such that e.g. a 2km deep cloud with a CBH<300m will only be counted in the CCprcp category. Note that the above classification into the different CBH categories does not consider the cloud objects and all HF profiles are classified independently. A similar analysis accounting for the cloud objects by classifying CC contributions of different cloud types by their cbhID is shown in Appendix A."

- Why does the SNR have a unit, shouldn't it be without unit (l.112)? what is meant by smaller; shouldn't larger absolute values (i.e., smaller than -18.3dB) mean better SNR?

dB is a logarithmic dimensionless unit. It is computed from the intensity as follows: SNR=10*log10(intensity-1)
The larger the SNR, the better the measurement quality. This is the reason for which we discard measurements with an SNR smaller than -18.3dB.

- Figure 2.3, Fish example: how do you interpret the detected cold pool existing over more than 6h. I don't think this temperature anomaly should be detected as cold pool but rather represents some meso-scale (cold) front as also indicated by the satellite snapshot? (see major point regarding cold pool detection algorithm)

Please refer to our answer for the major point regarding cold pool detection algorithm above.

- Winter vs. summer trades: the logic derived why to use winter trade statistics makes sense. However, based on what is it decided whether or not to consider only winter trades (l. 195: "for most of the analysis…")? Can you be more specific here?

The main motivation for focusing on the winter trades is that trade cumuli predominate in winter. In summer, the ITCZ is often in close proximity of Barbados and convection is much deeper. As mentioned in L203-207, we could have achieved the goal to focus on trade cumulus cold pools only by excluding periods of deep convection, but at the expense of many more excluded cold pools (as the radar wasn't running about half of the time).

We added some more motivation regarding the winter focus in the Introduction (see also our answer related to the same comment under '1. Introduction' above).

- noprevWI criterion (Sec. 2.5): The definition of the criterion is ambiguous (l. 203): do you mean that there could be a cold pool detected in the preceding hour, but it has to be terminated, or that no cold pool can be present? How does that conflict with your discussion about the ambiguity of the algorithm about determining the cold pool end?

Yes, there could be a cold pool in the prior hour, but the temperature has to be recovered by at least deltaT/e. This doesn't conflict with the previous discussion, as cold pools are only referred to as recovered in case their t_end is well defined (see L 159).

3. Results:

- Horizontal wind anomaly (l. 242): the value of 1.14m/s seems very low, specifically since you're measuring the combination of cold pool propagation speed and its internal circulation. Do you have any thoughts on that?

The value is quite low as it is computed from the 10-min filtered wind speed data. We now added the unfiltered wind speed maxima in Table 1 and they are more than twice as large for the median anomaly (2.81 m/s). This value is in line with values from RICO and EUREC4A (Zuidema et al. 2012, Touzé-Peiffer et al. 2021).

- You state that the front duration explains a lot of the variation in temperature anomaly. Is the front duration correlated with horizontal wind anomaly, such that longer duration can be translated to spatially wider cold pool front, such that your finding can be expressed as that colder (stronger) cold pools have wider fronts? Do you have an understanding, what causes differences in the front duration? Is it correlated with it correlated with the rain duration or intensity?

The rain duration is indeed an important predictor of the cold pool strength and explains even more variability in ΔT (R^2=0.364) than the downdraft strength (R^2=0.23). The rain duration is well correlated with the front duration (R=0.47) and explains considerably more variability in ΔT then the accumulated rain in the front, suggesting that the rain intensity might be less important, or also not as well sampled. On the other hand, the front duration is not very strongly correlated with the wind speed anomaly (R=0.32), indicating that stronger cold pools are not necessarily wider cold pools.

We adjusted the paragraph as follows:
"The rain duration in the front is the diagnostic that explains most variability in ΔT (R2=0.364), partly because it is well correlated (R=0.47) with the front duration, which itself explains a comparable amount of variability in ΔT (R^2=0.357). That the accumulated rain amount in the front explains less variability in ΔT (R2=0.23) than the rain duration indicates that the rain intensity is of secondary importance. Another important predictor of ΔT is the downdraft strength wminSCL (R2=0.23), which together with the front duration explains 50% of the variability in ΔT for the noprevWI set."

- Temperature recovery time of 16min (l. 277): how can I see this numerical value from the figure (or elsewhere)? How did you derive it?

This is not evident from the figure and we added "(not shown)". It is computed by averaging the recovery time (i.e. time until temperature recovered by dT/e) of all recovering cold pools (i.e. cold pools that recover by dT/e before the next temperature drop).

- Humidity recovery (l. 28): I do not fully understand your reasoning here. Are you speaking about enhanced surface fluxes in the cold pool interior that are trapped in the boundary layer?

Here we mostly refer to the shallowness of the mixed layer inside cold pools (see Rochetin et al., 2021 and Touzé-Pfeiffer et al., 2021). So the surface latent heat fluxes are distributed over a shallower layer, which allows for a faster recovery of the humidity.
We added: ... 'anmalously' [shallow mixed layer] to clarify this.

- Updraft strength: I am not sure I agree with your conclusion on l. 312 about the convection triggering. Do you think updraft strengths of below 1m/s that travel with the cold pool front (i.e., are not stationary) are sufficient to trigger convection?

Yes, we think that these vertical velocities are relevant for triggering new convection, as they are much larger than typical in-cloud vertical velocities at cloud base. This is an important point that we clarify in the revised manuscript as follows:

"The median w_max450 at the gust front edge (see Table 1) is with 1 m s−1 much larger than the averaged hourly in-cloud vertical velocities near cloud base measured by the BCO Doppler radar, which has a peak density at 0.2 m s−1 and maxima of 0.6 m s−1 (Klingebiel et al., 2021). 1 m s−1 also marks the upper tail of cloud-base averaged updraft vertical velocities (see Figure 4b of Sakradzija and Klingebiel, 2020). This suggests that the gust-front vertical velocity maxima are very relevant for triggering new convection in the trade cumulus regime."

- Comparison to DYNAMO (l. 320ff): please complement the qualitative comparison with quantitative indications / statements.

We made the comparison more quantitative as follows:
"[...], just with slightly larger mean across-front temperature and humidity decreases (−1.3 K and −0.6 g kg−1 during DYNAMO compared to −1.15 K and −0.25 g kg−1 at BCO) and larger mid-front wind speed increases (about 1.5 m s−1 compared to 1 m s−1) during DYNAMO due to the deeper convection. Furthermore, during DYNAMO the increases in specific humidity at the beginning of the front are hardly present, and the wind speed remains elevated by 0.4 m s−1 in the wake of the DYNAMO cold pools (de Szoeke et al., 2017), whereas at BCO the wind speed decreases below the value at tmax in the wake."

- Figure 3: connection between variables (within cold pool) should be discussed more in text

The connection between the different variables is now discussed more prominently in different sections, and also in Section 3.1, where we added the following sentence:
"[The strongest cold pools last longer, follow each other more quickly (lower ∆tnextcp), and are associated with deeper clouds, more rain, stronger downdrafts, humidity drops and wind gusts, and larger positive vertical velocities at the beginning of the front compared to weaker cold pools]. This agrees well with the conceptual picture of deeper clouds producing more rain and having a larger potential for rain evaporation, which drives stronger downdrafts that bring down more dry air from further aloft, and which induces a stronger cooling and a stronger gust front that is associated with stronger rising motion at its leading edge."

- Figure 4b: Is a decrease in CBH an indicator of different cloud type? Why is the CC larger for stronger compared to weaker cold pools? Are parent clouds that formed the weaker cold pools already dissipated?

Figure 4b shows the composite mean CBH and as such reflects that a large portion of the front of cold pools is associated with very shallow CBH below 500m, indicative of the abundance of precipitating clouds (as confirmed by Figure 4d).
Stronger cold pools are associated with above average contributions of precipitating clouds and clouds aloft (4d,e). We also hypothesize that this is due to the parent convection of

stronger cold pools moving over BCO, while the parent convection of weaker cold pools might have already dissipated. We added the following discussion:

“Overall, Figure 4 indicates that clouds and rain are nearer t_min in the strongest cold pools, and nearer t_max for the weakest cold pools. A potential explanation for this observation is that stronger cold pools are running further ahead of their stronger parent convection, while the weaker parent convection of the weaker cold pools might have already dissipated. However, drawing such conclusions from single-point observations is tricky, as the influence of the life cycle stage and the overall cold- pool strength on the observed cold-pool characteristics cannot be disentangled. Nevertheless, some information about different cloud types populating the cold-pool front or wake can be derived by analysing the CC contributions grouped by the overall CBH of the segmented cloud objects (see Appendix A and Section 2.1). We find that the peak in CC_lcl at t_max is mainly due to edges of precipitating clouds that have a CBH > 300m. Assuming that this cloud population represents the clouds evident as mesoscale arcs in satellite imagery, this suggests that the cloudiness at the gust front is mostly characterized by well-developed precipitating clouds. [...].”

- Figure 4c: How do you interpret that the cloud cover increases immediately over the cold pool front and rain is falling during front passage? Are the cold pool fronts close to the rain cell, almost as if the meso-scale arcs form squall-line like structures with the cold pools propagating right ahead of the arc? Do you relate the precipitation falling “over” the front to the parent rain cell (that produced the cold pool) or can it be attributed to a new rain cell that was triggered by the cold pool?

As already explained in the previous answer, we hypothesize that the precipitation falling over the end of the front is mostly related to the parent convection triggering the cold pool. We plan to investigate this in more detail in the future with the aid of GOES-16 ABI satellite images, which might help collocate the clouds sampled at BCO with the broader view of the entire cold pool seen from space.

- Figure 5: How can the pretty pronounced negative values in U-U(t_max) in the wake of the cold pool fronts be interpreted?

The winter season at Barbados is characterized by very steady easterlies. So the positive wind speed anomalies inside the cold-pool front show that cold pools are mostly pushing forward with the wind in the front, whereas the negative anomalies in the wake suggests they on average tend to push backward into the wind after t_{min}. We already discuss this in what is now L342ff:
"As the cold pools spread into a strong background easterly flow (mean wind direction at t_max is 86°, not shown), the wind speed anomalies show that the cold pools on average push forward into the wind until tmax, and backward after tmin. For some cold pools, t_min might thus mark the center of the divergent flow and indicate that the parent convection passed over BCO."

And mention this potential explanation again in the discussion of Figure 5:
“Notable is again the occurrence of pronounced negative values of the wind speed anomaly after tmin, which suggests that some cold pools push backward into the mean wind.”

- Comparison to “average” winter trades: please complement text with numerical values and references (l. 360, 361)

The reference here is to the climatological average of all winter months of the period 2012-2021, computed from the radar data used throughout the paper. To make this more clear and quantitative, we changed the paragraph to:

"Figure 4a-f also indicate the respective mean CTH, CBH and CCs for all the winter months of the period 2012-2021. They show that cold-pool periods are much cloudier than the average winter conditions at BCO, with the average in-front CC being twice as large as the 10-year

climatological mean. Cold-pool periods also have much deeper clouds than the climatological mean of about 2 km, which is expected as it needs deeper precipitating clouds to form cold pools. The enhanced CC in the wake of cold pools compared to the long-term mean is nevertheless surprising, as convection might be expected to be suppressed in the cold-pool wake. "

- Figure 6a: Not being familiar with trade shallow convection diurnal cycle: can you extend a bit on how the strong increase in cold pool frequency right before midnight can be explained (Fig. 6a)? Is it related to the increased CTH during the night, leading to an increase in rain intensity and thus increased frequency (and strength) of cold pools? Please extend a bit.

Yes, this is the reason.
"There are clearly fewer cold pools and a lower hourly cold-pool frequency between 16-22 LT compared to the rest of the day. Just before midnight, the cold-pool frequency strongly increases in response to the night-time increase in cloud cover, cloud depth and rain rate (see green lines in panels e-i and Vial et al. (2019)). The cold-pool occurrence remains strongly elevated between 2 LT and 15LT, with a peak at 14 LT."

- Daily Cycle: are there any conclusions be drawn regarding the causal structure of the cold pool - cloud coupling? Would you, combining the reasoning in paragraph 3.3 and the observed diurnal cycle, conclude that the cold pool - cloud coupling is mainly a "one way street", where the cold pools are strongly influenced by the clouds (strength etc.), while there is a minor feedback from the cold pools back to the clouds pointing to a negligible cloud triggering effect due to cold pools?

No, we wouldn't conclude that. In contrast, we argue that cold pools help extend the diel cycle of shallow convection through the triggering of new convection. As clarified in the revised manuscript, we think that cold pools are strong enough to trigger new convection and subsequent cold pools into the early afternoon. Please refer to main comment 3 for our adjustments in the manuscript.

- Figure 6b, c: Panels b, c show large jumps in the mean timeseries right at 19-20:00. Is that an artefact of the splitting of the time series at that hour?

No, this isn't an artifact of splitting the time series. In Figure 6, we didn't apply a running average too smooth the timeseries and large jumps are also apparent at other times (e.g., between 1-3LT in panel g for w_min.SCL.

- Figure 6: in contrast to the previous paragraph, where stronger cold pools are associated with higher CTH, this correlation doesn't show up here: higher CTH 20:00-08:00 vs. (slightly) stronger cold pools 08:00-17:00. How should that be understood?

It is indeed a bit surprising that the cold-pool strength is not enhanced during the night when the CTH but also the rain rate tend to be enhanced. In the next section we argue that this is linked to daytime cold pools being mostly associated with the Fish pattern, which tend to be stronger than cold pools from the other patterns.

4. Relationship to mesoscale pattern

- Figure 8: The same arrangement of sub-panels according to the variables as in Fig. 4 would be helpful for easier comparison. Why aren't you showing all variables shown in Fig. 4?

We didn't show all panels of Figure 4, as much of this information is already contained in the box plot, and we only wanted to highlight the most important aspects.

- Figure 8e-h: colorbar missing

We added the color bar also in this figure and removed the reference to Figure 4.

- What are the main findings of Fig. 8? Can you highlight this more in the text?

We restructured the discussion of Fig. 8 to highlight the main findings more concisely. The paragraphs now read:

"Figure 8 shows the differences in the temporal structures of cloud properties associated with the cold-pool passages for the four patterns. Fish and Flowers have the largest CC (8a) due to larger contributions of CCaloft (8c), which are associated with frequent stratiform layers near 1.5-2 km (8f,h). C Clcl (8b) and C Cprcp (not shown) instead are fairly similar among the patterns. The CC of Fish cold pools hardly changes across the cold-pool passage, whereas the onset of the cold-pool front is much more clearly evident for the Gravel and even more for the Sugar CC (also see the time-height composites in Figure 8e-h). The CC in the wake of Sugar cold-pools also decreases most rapidly back to its pre-front value. Fish tends to have the deepest mean CTH associated with the cold-pool periods, closely followed by Gravel and Flowers. Again, the mean CTH of Gravel and Sugar cold pools increase most rapidly in the front compared to the other patterns.

For all patterns, the cold-pool periods are characterized by significantly deeper clouds and larger CC compared to the pattern average (indicated by the dashed lines on the far-left of 8a-d). Nevertheless, the climatological differences in CC, CCaloft and CTH among the different patterns (Schulz et al., 2021; Vial et al., 2021; Bony et al., 2020) also remain during cold-pool periods, indicating the robustness of the pattern-specific cloud macrophysical properties."

- Number of cold pools (Figs. 7a, 9a): wouldn't it make sense to show some kind of normalised number of cold pools that allows to understand how the cold pools "density" varies among the different mesoscale patterns? E.g., normalising the number of cold pools shown (which is, if I understand correctly, the sum of all detected cold pools given a certain weather situation?) by the relative occurrence of the cloud pattern.

Normalizing the cold pool number by the pattern occurrence frequency is indeed very important, as the pattern frequencies are very different. This is what is shown in Figures 7b and 9c. To make sure the readers understand that we make this distinction, we restructured the paragraphs to highlight the most important aspects and left away a lot of the more detailed explanations.

- Fig. 8, 9: how is the number of cold pools related to the number of clouds (entities) in the different trade cumuli patterns?

We didn't look at this explicitly, but as Fish and Flowers tend to be associated with larger mean object sizes (see Bony et al. 2020) but fewer cloud objects, and as Fish and Flowers have the largest cold-pool frequencies, we'd expect a slight anti-correlation between the number of clouds and the number of cold pools.

5. Conclusions:

Summer cold pools: How do the weaker updrafts fit with stronger temperature drops?

This is indeed somewhat surprising, and we don't have a good explanation for it. The wind shear is different in the summer vs. the winter trades (Brueck et al. 2015 JAS), such that the weaker updrafts might be related to wind shear effects on the vortical circulation. A more in-depth analysis of the circulation in the cold-pool front might provide an answer, something we plan for the future.

Please also note the supplement to this comment:
https://acp.copernicus.org/preprints/acp-2021-420/acp-2021-420-RC1-supplement.pdf
We answered all supplementary comments directly in the annotated manuscript.

Anonymous Referee #2

The authors present a careful study of thousands of cold pools from a long and detailed record of observations from the Barbados Cloud Observatory. As well as the excellent statistics from a data set of this size, vertical profiles of hydrometeor fraction are a novel an interesting addition to the study. Summer cold pools resemble those previously found for deep convection, while winter trade wind conditions have cold pools with positive water vapor anomalies at the head of their fronts. Cold pool occurrence and shape are also diagnosed according to the diel cycle and cloud pattern classification (Sugar, Gravel, Flowers, Fish) of Stevens et al. 2020.

The paper presents long and detailed analysis. At times I would have liked it to state the results more succinctly, yet overall I found it interesting, and readers will be able to find a great of deal of detail when they want it. I recommend publication with minor revisions. In the annotated PDF I have included some minor comments on the science and line edits intended to improve clarity and readability.

We thank the referee for the positive assessment. In response to the comments of all three referees, we added some more physical explanations and hypotheses to interpret the correlations found. We also put the results more in context of the previous literature. Furthermore, we shortened and sharpened certain parts that were somewhat lengthy, which will ease the reading.

Please also note the supplement to this comment:
https://acp.copernicus.org/preprints/acp-2021-420/acp-2021-420-RC2-supplement.pdf
We answered all the specific comments directly in the annotated manuscript.

Anonymous Referee #3

The paper presents a climatology of trade-wind cumuli based on more than ten years of data from the Barbados Cloud Observatory. Moreover, it makes an attempt to link the cold-pool characteristics to the mesoscale cloud organization. The paper is well written, logically organized and presents very interesting results. It is very nice to see a cold-pool climatology based on observational data over such a long time span. I only have some minor comments.

- Doppler Lidar data: did the authors encounter any issues with the data retrieved by the Doppler Lidar during rainy periods? Often, these periods are discarded from the records. Moreover, the aerosol load can be reduced significantly after rainy periods, deteriorating the signal quality.

Doppler lidar vertical velocity retrievals are usually very reliable also in rainy periods, see e.g. Zhu et al. 2021 (GRL, doi: 10.1029/2020GL090682). We didn't encounter problems with the Doppler lidar retrievals in rainy periods and didn't discard data due to a potential rain contamination. Both the composite temporal structure in Figure 3h and also the vertical velocity profiles at the bottom of the radar reflectivity panels of the example cases in Figure 2 indicate that the negative vertical velocities are well sampled in rainy periods (note e.g. the pronounced downdrafts and apparently good data quality during the strongly precipitating period of the Fish day between 05-11:30LT).

The points you raise might nevertheless be an issue in some cases, like potentially in the Flowers example case around 13LT, where the SNR is too low during the rainy period and also right after (potentially due to reduced aerosol loading). So we added a few sentences discussing these issues in Section 2.1:

"Doppler lidar vertical velocities are commonly considered reliable also in rainy periods (see e.g. Zhu et al. 2021). We did not encounter problems with the Doppler lidar retrievals in rainy periods and Figure 2 and Figure 3h later show that the negative vertical velocities associated with downdrafts are generally well captured."

- Cold-pool detection algorithm and analyzed near-surface variables: I was missing surface-pressure in the list of analyzed variables. Already in the cold-pool detection algorithm it could be included as an additional criterion to identify a cold pool, but it would definitely be worth adding it to the list of analyzed variables. Increases in surface pressure in connection with the cold pool can give a hint on the spreading cold-air mass. While wind speed is shown, wind direction could be a further interesting candidate.

For the cold-pool detection, we decided to focus on the temperature drop alone in order not to bias the moisture signal of the cold pool. We agree that the surface pressure or also the buoyancy could already be included in the cold-pool detection. We checked how the results depend on using theta_v instead of temperature, but only found very minor quantitative differences (not shown).

In the course of the study, we analyzed the changes in wind direction and surface pressure and motivated by your comment, we now also include the maximum pressure anomaly (Δp_{max}) and the mean wind direction change ($\Delta wdir_{mean}$) in Table 1. The figure below shows that the cold-pool associated changes in the surface pressure anomalies (pres.SRF) and mean wind direction (wdir.SRF) are also pronounced. As Figure 3 already has eight panels, we decided not to include additional wind direction and surface pressure panels.

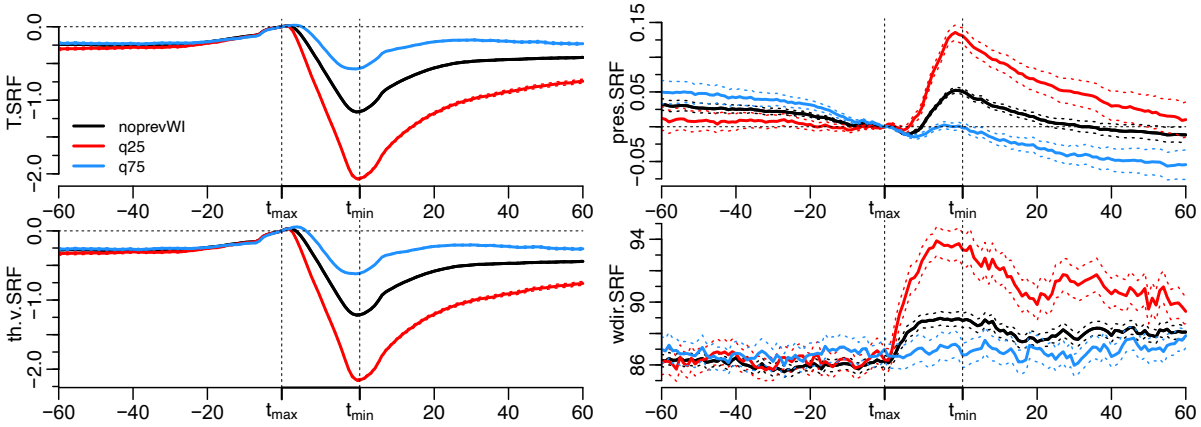

- Mesoscale cloud organization: The neural-network based classification on the brightness temperature from the GOES-16 Satellite is an interesting dataset to classify mesoscale cloud organization, and the catchy names of the identified patterns are intriguing. Yet, to have a more general classification and to add information to this one single dataset I suggest to widen the classification to more classical approaches such as e.g. spectral analyses (e.g. Wood and Harmann, 2006).
Extending the analysis to another classification method is a good suggestion. However, the Wood and Hartmann (2006) classification doesn't work well for trade cumulus with cloud layers deeper than ~2 km, as the *cellular but disorganized* category strongly dominates in the trade-wind regions and hardly any open and practically no closed cell organizations occur (see Muhlbauer et al., 2014 ACP). In general, there are no well-established methods for characterizing trade cumulus mesoscale organization at the moment. An effort to systematically compare different classification methods is currently undertaken by Isabel McCoy, Hauke Schulz, Leif Denby and others. Such a comparison will help gear a future study to include also other classifications of trade cumulus organization.

In a recent study (Vial, Vogel and Schulz, 2021 QJRMS), we compared the diurnal cycles of the four organization patterns using two different automated classification methods: the same neural-network classification as used here and also an independent classification of the four patterns based on the Iorg clustering index and the object size ("Iorg/S" method, following Bony et al., 2020 GRL). The two independent methods yielded qualitatively similar results, which improves confidence in the pattern classification. Here we only focus on the neural network labels, as the Iorg/S method can only be used on relatively large domains (e.g. 10°x10°) and not for a specific location such as the BCO.

Technical comments:

- Table 1: please specify ΔTunfil. Specified!
- Caption to Table 1: I suggest to replace "How the ..." with "The computation of the diagnostics". Changed, thanks for the suggestion.
- Line 235: add full stop after "mentioned" changed
- Line 265: replace "like" with "such as". changed
- Line 328: another study that has looked at the moisture origin within cold pools in detail is Schlemmer and Hohenegger (2016). We added the citation as follows:
"The initial increase in humidity at the edge of the front at BCO might be explained by enhanced surface fluxes due to the strengthening winds (Langhans2015,Torri2016), by moisture advection (Schlemmer and Hohenegger, 2016), or by an accumulation of moisture from evaporation..."

https://doi.org/10.5194/acp-2021-420
Preprint. Discussion started: 1 June 2021
© Author(s) 2021. CC BY 4.0 License.

Atmospheric Chemistry and Physics Discussions

A climatology of trade-wind cumulus cold pools and their link to mesoscale cloud organization

Raphaela Vogel[1], Heike Konow[2], Hauke Schulz[3], and Paquita Zuidema[4]

[1]LMD/IPSL, Sorbonne Université, CNRS, Paris, France
[2]Meteorological Institute, Universität Hamburg, Hamburg, Germany
[3]Max Planck Institute for Meteorology, Hamburg, Germany
[4]Rosenstiel School of Marine and Atmospheric Science, University of Miami, Miami, FL, USA

Correspondence: Raphaela Vogel (raphaela.vogel@lmd.ipsl.fr)

Abstract. We present a climatology of trade cumulus cold pools and their associated meteorological perturbations based on more than ten years of in-situ and remote sensing data from the Barbados Cloud Observatory. Cold pools are identified by abrupt drops in surface temperature, and the mesoscale organization pattern is classified by a neural network algorithm based on GOES-16 ABI infrared images. We find cold pools to be ubiquitous in the winter trades—they are present about 7.8% of the time and occur on 73% of days. Cold pools with stronger temperature drops (ΔT) are associated with deeper clouds, stronger precipitation, downdrafts and humidity drops, stronger wind gusts and updrafts at the onset of the front, and larger cloud cover compared to weaker cold pools. The downdraft strength together with the cold-pool front duration explains 50% of the variability in ΔT.

The mesoscale organization pattern has a strong influence on the occurrence frequency of cold pools. Fish has the largest cold-pool fraction (12.8% of time), followed by Flowers and Gravel (9.9% and 7.2%), and lastly Sugar (1.6%). Fish cold pools are also significantly stronger and longer-lasting compared to the other patterns, while Gravel cold pools are associated with significantly stronger updrafts and deeper cloud-top height maxima. The daily cycle of the occurrence frequency of Gravel, Flowers, and Fish can explain a large fraction of the daily cycle in the cold-pool occurrence, as well as the pronounced extension of the daily cycle of shallow convection into the early afternoon by cold pools. Overall, we find cold-pool periods to be 90% cloudier relative to the average winter trades. Also the wake of cold pools is characterized by above-average cloudiness, suggesting that mesoscale arcs enclosing broad clear-sky areas are an exception. A better understanding of how cold pools interact with and shape their environment could therefore be valuable to understand cloud cover variability in the trades.

1 Introduction

Satellite images in the trades usually show very beautiful and diverse cloud structures over the dark blue ocean. Recurrent features in these images are mesoscale arcs of cumuli that encircle either clear-sky areas or extensive stratiform cloud decks.

https://doi.org/10.5194/acp-2021-420
Preprint. Discussion started: 1 June 2021
© Author(s) 2021. CC BY 4.0 License.

Atmospheric Chemistry and Physics Discussions

The mesoscale arcs result from spreading cold pools that have favourable conditions at their gust front for triggering new convection. Convective cold pools are generated by the evaporation of precipitation into unsaturated downdrafts, spreading out at the surface as a density current. Cold pools are not only important for the triggering of new and often deeper convection (Schlemmer and Hohenegger, 2014; Feng et al., 2015; Rowe and Houze Jr., 2015), but might also play a role in regulating cloud cover in this regime responsible for much of the uncertainty in climate sensitivity (Bony and Dufresne, 2005; Vial et al., 2013). Here we use ground-based in-situ and remote sensing data from the Barbados Cloud Observatory (BCO) to study the climatology of trade-wind cumulus cold pools and to investigate its link to the pattern of mesoscale cloud organization.

Many studies addressing oceanic cold pools have focused on deep convection (Zuidema et al., 2017). In the trades, detailed case studies for two weeks of the *Rain in Cumulus over the Ocean* (RICO) campaign have advanced our understanding of cold pools from shallow convection (Zuidema et al., 2012). They showed that the deepest clouds and strongest radar signals occurred in the moistest tercile of water vapour paths, and that precipitation-driven downdrafts can introduce additional gradients in the thermodynamic structure. More recently, analyses of data from the *Elucidating the Role of Clouds-Circulation Coupling in Climate* (EUREC^{4}A) field campaign (Bony et al., 2017; Stevens et al., 2021), which took place in January and February 2020 upstream Barbados, reveal that cold pools are frequent in the winter trades and can be well-detected from soundings due to their very shallow mixed layers (Touzè-Peiffer et al., 2021). What is missing is a longterm climatology of trade cumulus cold pools, along with a description of the changes in cloud properties and sub-cloud layer dynamics associated with the cold-pool passages. Such a climatology is particularly pertinent given the need for a reference dataset for comparison against increasingly-available high-resolution simulations (Stevens et al., 2019; Rochetin et al., 2021).

Renewed interest in trade cumulus cold pools is also motivated by recent advances in characterizing patterns of mesoscale cloud organization. Stevens et al. (2020) classified 900 satellite images in the North Atlantic trades and identified four prominent patterns of mesoscale cloud organization—Sugar, Gravel, Flowers and Fish. The horizontal structure of the latter three patterns is intrinsically linked to the occurrence of mesoscale arcs and hence cold pools. The four patterns differ not only in their horizontal structure, but also in cloud cover, cloud depth and precipitation (Bony et al., 2020; Schulz et al., 2021; Vial et al., 2021). These differences likely also manifest in different cold-pool characteristics. Furthermore, cold pools might play different roles in creating and maintaining these patterns. For the pattern Fish with its very large-scale fish-bone structures that are tightly linked to extratropical dry intrusions (Aemisegger et al., 2021; Schulz et al., 2021), cold pools are likely to give the cloudy part its skeletal structure, ~~but~~ the overall system is forced by the large-scale into its linear alignment. Contrastingly, for the Gravel pattern, the large-scale influence may be less important and also more heterogeneous, such that the cold pools likely play an important role in creating and maintaining this pattern. Before we can understand the different roles that cold pools play in these patterns, we need to understand whether and how cold-pool characteristics differ among them.

This paper presents the first longterm climatology of trade-wind cumulus cold pools and addresses the following research questions:

1. How frequent are cold pools in the trade cumulus regime, and with which changes in the surface meteorology, cloudiness and vertical velocity are they associated?

https://doi.org/10.5194/acp-2021-420
Preprint. Discussion started: 1 June 2021
© Author(s) 2021. CC BY 4.0 License.

Atmospheric Chemistry and Physics Discussions

2. How do cold-pool characteristics covary with the pattern of mesoscale organization?

We use more than ten years of surface meteorology and ground-based remote sensing data from the BCO (Stevens et al., 2016). Clouds, their precipitation and therefore likely also cold pools at the BCO were shown to be representative across the trades (Medeiros and Nuijens, 2016). Cold pools are identified by abrupt drops in surface temperature, and the pattern of mesoscale organization is classified by a neural network algorithm based on infrared satellite images (Schulz et al., 2021).

~~The next section~~ presents the data sources and explains the cold-pool detection algorithm and the selection criteria. In Section 3, we present the cold-pool climatology and analyse the temporal structure of ~~the~~ cold-pool passages and ~~its~~ associated changes in meteorology and cloudiness. Section 4 discusses differences between the cold-pool properties of the different mesoscale organization patterns. Conclusions are presented in Section 5.

2 Data and Methods

2.1 BCO data

We use in-situ and ground-based remote sensing data from the BCO (Stevens et al., 2016), which is operated by the Max Planck Institute for Meteorology together with the Caribbean Institute for Meteorology and Hydrology since April 2010. The BCO is located atop a 17 m cliff on an eastward promontory of Barbados called Deebles Point (13.16°N, 59.43°W), and samples nearly undisturbed Atlantic trade-wind conditions. We use surface meteorology and micro-rain radar (MRR) data ~~from~~ January 2011, cloud radar data ~~from~~ January 2012, and Doppler lidar data from March 2016 until March 2021. All data is aggregated into 1-min averages. The instruments used and meteorological variables derived are explained in the following. More details about the BCO and its instrumentation can be found in Nuijens et al. (2014) and Stevens et al. (2016).

Surface meteorology

A Vaisala WXT520 sensor mounted on a 5 m mast measures temperature, relative humidity, barometric pressure, wind speed and wind direction. We discard temperature measurements exceeding 35°C and pressure measurements lower than 980 hPa, as they are outside the expected range of variability at the BCO.

Micro-rain radar (MRR)

The MRR is a vertically-pointing frequency-modulated continuous-wave radar operating at 24 GHz (K band). The MRR has a sampling frequency of 10 s (here averaged to 1 min) and a range gate of 30 m up to a height of 3 km. Rain rates lower than 0.03 $\mathrm{mm\,h^{-1}}$ are below the noise level and set to zero. We derive the mean rain rate (RR) and the rain intensity (R_{int}; i.e. the rain rate during periods of rain) in a given period from data at 325 m above ground (the lowest level with reliable data). The MRR is also used to compute the rain frequency (R_{freq}), which is set to 1 when a $RR > 0.05\,\mathrm{mm\,h^{-1}}$ is measured in at least five range gates in the lowest 3 km (following Nuijens et al., 2014). A few instances with unrealistically large RR exceeding 200 $\mathrm{mm\,h^{-1}}$ are set to NA.

Cloud radar

https://doi.org/10.5194/acp-2021-420
Preprint. Discussion started: 1 June 2021
© Author(s) 2021. CC BY 4.0 License.

Atmospheric Chemistry and Physics Discussions

Vertical profiles of hydrometeors (i.e. cloud and rain droplets) at approx. 30 m vertical resolution are derived from two 35.5 GHz (Ka-Band) Doppler cloud radars. Radar returns with an equivalent radar reflectivity lower than −50 dBZ are removed to eliminate signal from sea salt aerosol (Klingebiel et al., 2019). To identify individual 2D cloud entities, a cloud segmentation algorithm is applied (Konow, 2020). Radar reflectivity is converted to a binary mask and morphological closing is applied. The resulting mask is used to segment cloud entities ~~with~~ connected components analysis with 8-connectivity. A minimum cloud size of four pixels is applied, everything smaller than four pixels is discarded as clutter. For the resulting cloud entities, the overall cloud-base height (cbh_{ID}), overall cloud-top height and the cloud length (i.e. the duration times the wind extrapolated from the surface to cloud base assuming a power law) are determined. To focus on clouds connected to the sub-cloud and trade-wind layer, cloud entities with a cbh_{ID}>4 km are excluded.

From the remaining clouds, we derive timeseries of the hydrometeor fraction, the lowest cloud-base height (CBH) and the highest cloud-top height (CTH) for every radar profile. The cloud cover is further split up into contributions from precipitating cloud segments if $CBH \leq 300$ m (CC_{prcp}), from cloudiness near the lifting-condensation level (CC_{lcl}; 300 m $< CBH \leq$ 1 km), and from cloudiness aloft (CC_{aloft}; 1 km $< CBH \leq 4$ km). The latter two categories were also used in many previous studies (e.g Nuijens et al., 2014; Vial et al., 2019). A given radar profile can only count to one of the three categories, such that e.g. a 2 km deep cloud with a CBH<300 m will only be counted in the CC_{prcp} category. Note that the above classification into the different CBH categories does not ~~account for the information of~~ the cloud entity and all radar profiles are classified independently. A similar analysis accounting for the cloud entity by classifying cloud cover contributions of different cloud types by their cbh_{ID} is shown in Appendix A.

From the cloud radar we also derive a deep-cloud mask, which is set to 1 if a radar signal between 4.5–8 km is detected. With this deep-cloud mask, periods of active deep convection reaching above the melting level can be omitted, while periods with only cirrus-clouds are retained.

Doppler lidar

The vertical velocity in the sub-cloud layer is measured by two Halo Photonics Streamline Pro Doppler wind lidar systems at 30 m vertical resolution. The Doppler lidars measure vertical velocities of up to $\pm 20\,\mathrm{m\,s^{-1}}$ with a 1500 nm laser in altitudes from about 50 m to 1 km, depending on the atmospheric conditions and the aerosol loading. The precision is $<20\,\mathrm{cm\,s^{-1}}$ for a signal-to-noise ratio (SNR) of -17 dB. Measurements with a SNR smaller than -18.3 dB are discarded. Data from the first system that was operated in vertically-pointing mode with a temporal resolution of 1.3 s is used from March 2016 to October 2019. A second system is operated in horizontally-scanning mode since February 2019 and has a temporal resolution of 3 s, with 2 out of 7 profiles measured in vertically-pointing mode. Vertical data from this second lidar is used from November 2019 to March 2021.

We derive both the average vertical velocity in the sub-cloud layer (SCL) as the mean over 15 range gates from 75-495 m (w_{SCL}), and the vertical velocity near the sub-cloud layer top at 450 m as the mean over the four range gates from 405-495 m (w_{450}).

https://doi.org/10.5194/acp-2021-420
Preprint. Discussion started: 1 June 2021
© Author(s) 2021. CC BY 4.0 License.

Atmospheric Chemistry and Physics Discussions

2.2 Machine learning classification of mesoscale cloud organization patterns

The pattern of mesoscale cloud organization at BCO for the period January 2018 to March 2021 is classified by a neural network algorithm applied to infrared satellite images from the Geostationary Operational Environmental Satellite 16 (GOES-16). We use 30-minute brightness temperature retrievals from the 10.35μm-channel at a spatial resolution of 2 km from the Advanced Baseline Imager (ABI) Level 1b data product (GOES-R Calibration Working Group and GOES-R Series Program, 2017), over a large domain including Barbados (45°W-66°W, 9.3°N-23.3°N).

The neural network based on the Retinanet algorithm (Lin et al., 2017) has been initially trained on and applied to visible images in Rasp et al. (2020), and later retrained and applied to infrared images by Schulz et al. (2021). The use of infrared images also allows study of the diurnal cycle of the mesoscale organization (Vial et al., 2021). The classifications of the neural network are rectangles of various sizes that belong to either the Sugar, Gravel, Flowers or Fish pattern. We select every classified rectangle that overlaps with the BCO location. Periods without a classification are labelled as 'No'. For conditioning on cold pools, the 30-min data is downscaled to 1-min by using a given pattern for the 15 min before to after the classification time. If a given pattern is present for more than 75% of the duration of a cold pool, the pattern is attributed to this cold pool.

At any given time, multiple rectangles of different sizes of the same and of different patterns can occur. Multiple rectangles of the same pattern are combined and counted only once, while multiple rectangles of different patterns are counted separately. This leads to timesteps being classified e.g. as both Gravel and Flowers. Excluding situations with multiple patterns only marginally influences the results, but reduces the sample size considerably (as previously noted in Vial et al., 2021). Ambiguities in the classification can be physical—for example due to regime transitions or similarities between patterns—or related to ambiguities introduced to the neural network by disagreement in the human classifications. The occurrence of multiple patterns can be reduced if a stricter threshold is used for the agreement score representing the confidence of the neural network prediction (here set to 0.4 as in Schulz et al., 2021; Vial et al., 2021), but this again reduces the sample size.

2.3 Cold-pool detection algorithm

We detect cold pools by identifying abrupt drops in the surface temperature timeseries following Vogel (2017). We first filter the 1-min averaged temperature timeseries with an 11-minute running average. We then classify all temperature drops $\delta T = T_{\mathrm{fil}}(t) - T_{\mathrm{fil}}(t-1) < -0.05$ K (per minute) in the filtered timeseries as a cold-pool candidate (see Figure 1 for an illustration). For every candidate cold pool, we detect the time of the cold-pool front onset ($t_{\max}$), the time of the minimum temperature ($t_{\min}$), and the end of the cold pool (t_{end}) as follows:

1. $t_{\max}$: the onset of the cold-pool front $t_{\max}$ is defined as the last instance of $\delta T > 0$ K within 20 min before the initial abrupt temperature drop. If the temperature is falling continuously in this period, $t_{\max}$ is chosen as the time of the maximum temperature (that is, 20 min before the abrupt temperature drop). We refer to the smoothed temperature at $t_{\max}$ as $T_{\max}$.

https://doi.org/10.5194/acp-2021-420
Preprint. Discussion started: 1 June 2021
© Author(s) 2021. CC BY 4.0 License.

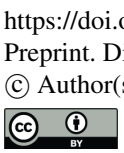

Atmospheric Chemistry and Physics Discussions

2. $t_{\min}$: the time of the minimum filtered temperature $T_{\min}$ marks the end of the cold-pool front and is identified as the minimum of contiguous temperature minima. Subsequent candidate cold pools with $\delta T < -0.05\,\mathrm{K}$ occurring within 20 min of the previous minimum are combined if the temperature does not rise by more than 0.5 K above the previous minimum in between.

3. t_{end}: the end of a cold pool is defined either as the minimum of (a) the time when the filtered temperature first exceeds its minimum by $\Delta T/e$, where $\Delta T = T_{\max} - T_{\min}$, or (b) the onset of the next cold pool. If using condition (a) or (b) leads to any temperature between $t_{\min}$ and t_{end} to be smaller than $T_{\min} - 0.1\,\mathrm{K}$, then t_{end} is defined as (c) the time when the filtered temperature first decreases again after increasing for some time following $t_{\min}$. Cold pools with t_{end} defined by (a) are referred to as recovered.

The period between $t_{\max}$ and $t_{\min}$ is referred to as the cold-pool front, and the period between $t_{\min}$ and t_{end} as the cold-pool wake.

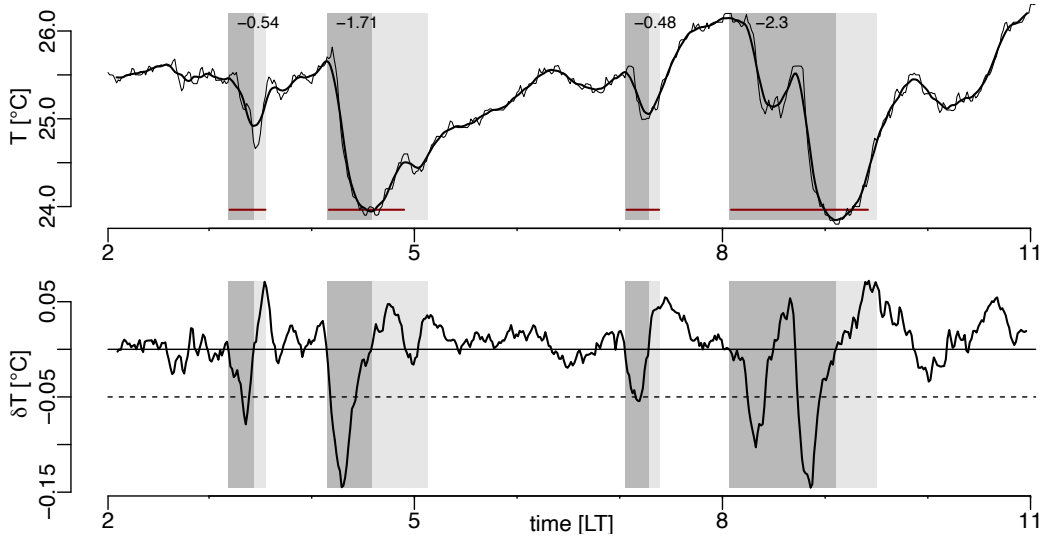

Figure 1. Illustration of the cold-pool detection algorithm. (top) 11-min filtered T_{fil} (thick line) and 1-min raw surface temperature (thin line), and (bottom) filtered temperature difference δT, along with the threshold of -0.05 K used (dashed). The detected cold-pool fronts and wakes are indicated in dark grey ($t_{\max}$ to $t_{\min}$) and light grey ($t_{\min}$ to t_{end}), with the corresponding ΔT indicated at the top. The dark red lines in the top panel show the analysis periods used for computing the diagnostics (see Section 2.5).

Our cold-pool detection algorithm is similar to the one used by de Szoeke et al. (2017), but with the important modification that we only identify cold pools for situations with abrupt temperature drops. With our algorithm we thus both filter out turbulent fluctuations and advective or diurnal patterns of temperature variability. The threshold of $\delta T < -0.05\,\mathrm{K}$ is subjectively chosen based on visual impression and represents distinct variations in temperature. For an 11-min averaging window, a δT of −0.05 K corresponds to about 2% of the data. Figure 2 shows example cold pools for all patterns and illustrates ~~the workings~~ of the algorithm. In next subsection we briefly discuss the strengths and weaknesses of the algorithm based on these examples.

https://doi.org/10.5194/acp-2021-420
Preprint. Discussion started: 1 June 2021
© Author(s) 2021. CC BY 4.0 License.

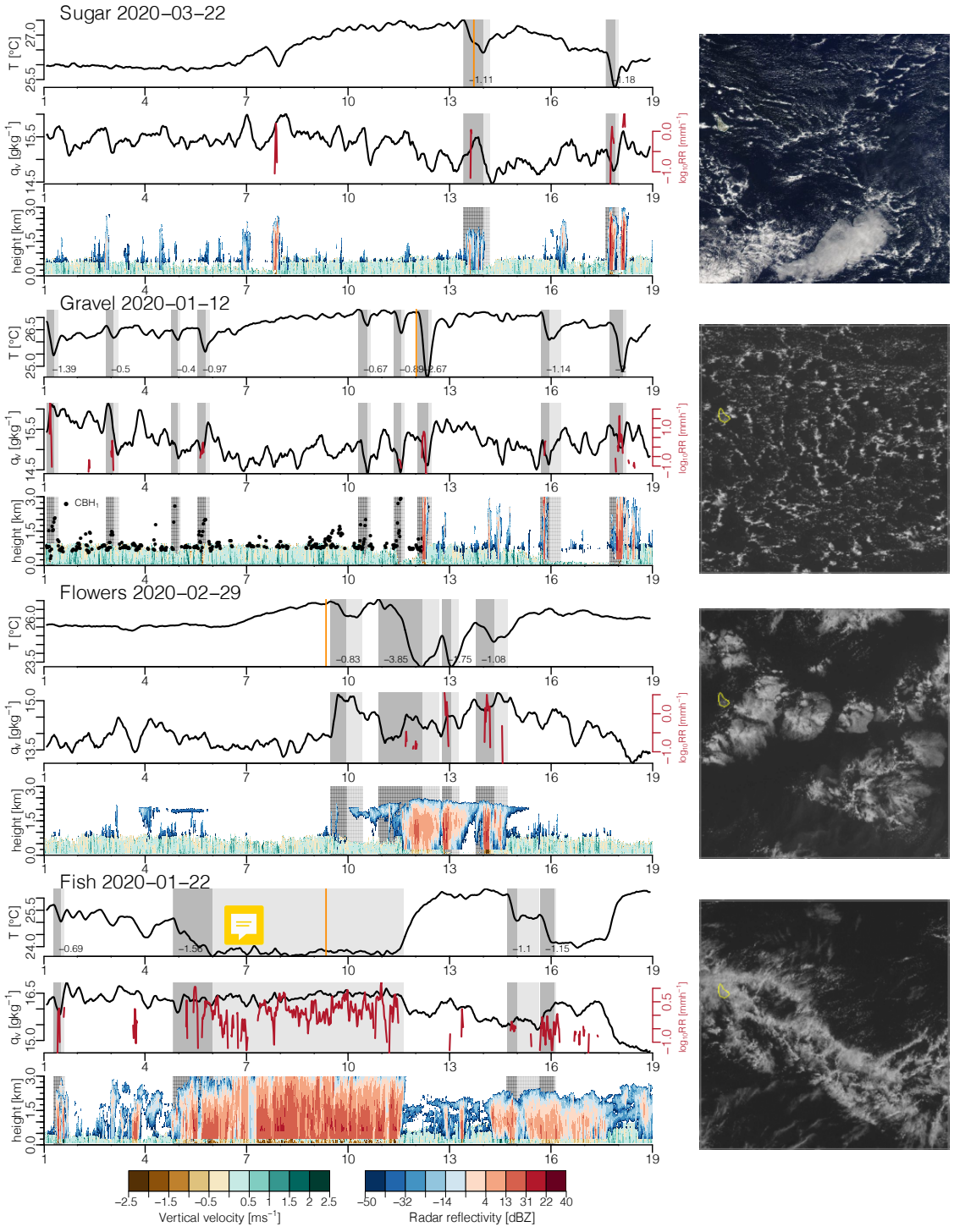

Figure 2. BCO time series and satellite images for 18 h of four cold-pool days representative of the four patterns. Shown are timeseries of filtered surface temperature and specific humidity, MRR RR, and time-height plots of Doppler lidar vertical velocity and radar reflectivity. On the Gravel day the radar did not work prior to 12 LT and the lowest CBH from the ceilometer is shown instead. The x-axis shows local time and the detected cold-pool fronts and wakes are indicated in grey and light grey, with ΔT indicated at the bottom. Visible satellite images from 10-15°N and 60-55°W from MODIS Aqua (Sugar day) and GOES-16 ABI (other days), with the respective recording times indicated by the orange lines in the temperature panels. The BCO is located near the easternmost tip of Barbados (outlined in yellow).

https://doi.org/10.5194/acp-2021-420
Preprint. Discussion started: 1 June 2021
© Author(s) 2021. CC BY 4.0 License.

Atmospheric Chemistry and Physics Discussions

2.4 Example cases

Timeseries of example cold-pool days along with corresponding satellite images are shown for every pattern in Figure 2. The example cases highlight how well the detection algorithm works in these diverse situations. Abrupt strong temperature drops are reliably detected, successive fronts sensibly combined into one single cold pool, and even the 6 h long cold pool with frontal character on the Fish day is correctly identified.

The example cases also indicate some challenges of the cold-pool identification. Although they look like cold pools, some temperature drops on the Gravel and Sugar day are not identified as cold pools because they are either not abrupt enough ($\delta T > -0.05$ K) or not strong enough ($\Delta T > -0.4$ K). The difficulty in defining the end of the cold-pool wake is illustrated in the Fish case: the cold pool starting shortly before 16 LT lasts until well after 18 LT, but the temperature drop near 17 LT causes a premature end of the cold pool, as such a temperature drop could also be caused by the daily cycle in temperature. The cold-pool end definition could be improved by an additional rain or downdraft requirement, to more robustly distinguish between cold-pool activity and other processes. Because most analyses and diagnostics computed in this study focus entirely on the cold-pool front (see next section), not fully representing the wake of rare long-lasting cold pools is a minor issue and only influences the overall cold-pool fraction and the duration statistics.

As mentioned in Section 2.2, the organization pattern definition is not unambiguous and also among the example days shown in Figure 2 some cold pools pertain to multiple patterns. For the Flowers case, the 2 h at the beginning and end of the period shown are also classified respectively as Gravel and Fish. In the Sugar case, only the period between 9-16 LT is exclusively classified as Sugar, while the periods before and after are also partly classified as Gravel. Most surprisingly, the textbook Gravel day is also entirely classified as Flowers, and also setting a stricter agreement score of 0.5 leaves half of the day co-classified as Flowers. This indicates that distinguishing Gravel from Flowers can be particularly challenging (as also shown in Vial et al., 2021). The Fish day is very confidently classified and no other pattern is detected for the entire day.

2.5 Selection criteria and diagnostics

For the subsequent analyses, we apply a number of selection criteria to make the comparison of cold pools more robust. Namely, we only consider cold pools with $\Delta T < -0.4$ K and less than two missing values in the filtered temperature timeseries during the entire cold-pool duration (set *all* with 9234 cold pools). For the analyses of the cold-pool properties we further apply a criterion of no non-recovered cold pool in the hour prior to the cold-pool onset (set *noprev* with 8772 cold pools), which selects cold pools moving into an initially undisturbed atmosphere that is not modified by previous convection. For most of the analyses we also focus on the dry winter regime from December-April (set *noprevWI* with 3889 cold pools), which is characterized by steady easterlies, subsiding large-scale motion in the free troposphere and the predominance of shallow trade-wind convection (Brueck et al., 2015).

As shown in the brackets, all these selection criteria reduce the cold-pool sample size considerably. They represent a trade-off between assuring a robust and unbiased sample to address our research questions, while not being unnecessarily strict and removing too many cold pools. The selection criteria are thus somewhat subjective and also differ among studies. For example,

https://doi.org/10.5194/acp-2021-420
Preprint. Discussion started: 1 June 2021
© Author(s) 2021. CC BY 4.0 License.

Atmospheric Chemistry and Physics Discussions

Chandra et al. (2018) used the criterion of no rain in the hour prior to the cold-pool onset to select cold pools unmodified by previous convection, whereas we achieve the same goal with the criterion of no non-recovered cold pool in the prior hour, which excludes about 2500 less cold pools in our case. Instead of focusing on the winter regime, we could have also set a criterion based on the cloud-top height to focus on trade cumulus cold pools. However, as this would restrict the analysis to periods when the radar is running, and—as we are relying on single-site measurements—the parent convection might not move over the BCO in its entirety, we would likely exclude too many cold pools with a CTH criterion, without even being sure that periods of deep convection are really excluded. Despite the rather strict criteria applied here, the long timeseries leads to a much larger number of cold pools analysed than in previous studies.

Another potential sampling issue regarding the single-site measurements is that it is not clear at which stage of its lifecycle we sample the cold pool, and where we sample it with respect to its center. Assuming isotropic wind variations around the cold-pool center, which in case of little wind shear is a good approximation (Touzè-Peiffer et al., 2021), the change in wind direction from the mean direction prior to the cold-pool onset could give a hint as to the location relative to the cold-pool center. However, due to our large sample size potential biases are likely to be small.

If not mentioned differently, the cold-pool diagnostics are computed either as the minimum difference ($\Delta X_{\min}$) or maximum difference ($\Delta X_{\max}$) of a variable X between its value at $t_{\max}$ and the values between $t_{\max}+1$ and $\min(t_{\text{end}}, t_{\min}+20)$. Similarly, X_{mean} or $X_{\max}$ are the mean or maximum of variable X over the same analysis period (indicated in dark red in Figure 1). For the Doppler lidar vertical velocities, we diagnose w_{maxSCL} (w_{max450}) as the maximum w_{SCL} (w_{450}) in the first half of the front (including the last 10 min before $t_{\max}$), and w_{minSCL} as the minimum w_{SCL} in the second half of the front (including the first 10 min after $t_{\min}$). Unless otherwise stated, the surface meteorology diagnostics are computed from the 11-min filtered timeseries.

Along with most diagnostics and composites we show the standard error (SE), which measures how well the median or mean of a given sample can be estimated. The SE of the median is computed as $IQR/\sqrt{n}$, where IQR represents the inter-quartile range and n the sample size, and the SE of the mean as $\sigma/\sqrt{n}$, where σ is the standard deviation. As not all instruments were running all the time, some diagnostics are only available for a subset of the cold pools and the sample size is adjusted accordingly when computing the SE.

3 Cold-pool climatology

In this section we present the climatology of trade cumulus cold pools detected at BCO for the winter seasons of the years 2011-2021. The first subsection presents general statistics, followed by a discussion of the composite temporal structure of the cold pools in Section 3.2. The daily cycle of cold-pool statistics is shown in Section 3.3. While our focus lies on the winter regime, Appendix B also briefly discusses the seasonal cycle of the cold-pool statistics.

https://doi.org/10.5194/acp-2021-420
Preprint. Discussion started: 1 June 2021
© Author(s) 2021. CC BY 4.0 License.

Atmospheric Chemistry and Physics Discussions

3.1 General statistics

In total we detect 3889 cold pools that meet the criteria of $\Delta T < -0.4$ K and less than two missing values in T_{fil} in the winter seasons considered. We find that cold pools are very frequent at BCO and on 73% of days at least one cold pool is detected. The BCO is on average affected by cold pools during 7.8% of the day (i.e. 112 min) and by a cold-pool front during 4.4% of the day, with the medians being about one-third smaller than the means mentioned. The mean cold-pool fraction of 8.6% for January and February 2011-2021 is also very close to the 7% found by Touzè-Peiffer et al. (2021) during the EUREC^{4}A campaign in January and February 2020, despite their very different method defining cold pools in atmospheric soundings based on a mixed-layer depth criterion.

Table 1. Table showing median$\pm IQR$ of various cold-pool properties for the *noprevWI* set of cold pools, as well as the 25% strongest ($\Delta T < -1.39$ K) and weakest ($\Delta T > -0.61$ K) cold pools of this set. How the diagnostics are computed is explained in Section 2.5 and in the text.

	noprevWI	strong	weak
#	3889	972	972
ΔT [K]	-0.89±0.78	-1.82±0.67	-0.5±0.1
$\Delta T_{\mathrm{unfil}}$ [K]	-1.2±0.8	-2.16±0.66	-0.79±0.17
Δq_{min} [gkg^{-1}]	-0.43±0.65	-0.55±0.81	-0.36±0.54
Δq_{max} [gkg^{-1}]	0.2±0.41	0.29±0.51	0.12±0.3
$\Delta \theta_{\mathrm{e,min}}$ [K]	-2.05±2.08	-3.3±2.25	-1.35±1.35
$\Delta \theta_{\mathrm{v,min}}$ [K]	-0.96±0.81	-1.92±0.7	-0.55±0.14
ΔU_{max} [ms^{-1}]	1.14±1.55	2±1.97	0.7±0.99
R_{int} [mmh^{-1}]	0.9±1.76	1.45±2.42	0.41±0.95
RR_{mean} [mmh^{-1}]	0.05±0.38	0.39±1.06	0±0.04
CTH_{max} [km]	3.04±1.11	3.56±1.2	2.66±0.96
CTH_{mean} [km]	2.32±0.88	2.74±0.81	2.03±0.89
w_{minSCL} [ms^{-1}]	-0.55±1.56	-1.89±2.42	-0.27±0.51
w_{maxSCL} [ms^{-1}]	0.91±0.62	1.1±0.7	0.78±0.54
w_{max450} [ms^{-1}]	0.98±0.81	1.27±0.99	0.79±0.66
length [km]	13.34±9.49	18.65±10.94	10.01±6.03
$\Delta t_{\mathrm{nextcp}}$ [min]	117±426	85±245	158±725
dur [min]	33±22	47±29	25±12
front dur [min]	19±12	29±19	15±4

Table 1 presents statistics of the most important cold-pool properties for the set of winter cold pools with no non-recovered cold pool in the prior hour (*noprevWI*). It shows that 50% of the cold pools have a temperature drop exceeding 0.9 K across

https://doi.org/10.5194/acp-2021-420
Preprint. Discussion started: 1 June 2021
© Author(s) 2021. CC BY 4.0 License.

Atmospheric Chemistry and Physics Discussions

the front (the unfiltered temperature drop is 0.3 K stronger), a $\Delta q_{\max}$ exceeding 0.2 g kg^{-1} and a $\Delta q_{\min}$ below -0.43 g kg^{-1}, decreases in θ_e and θ_v exceeding -2.1 K and -0.96 K, respectively, and a $\Delta U_{\max}$ larger than 1.14 m s^{-1}. The median rain intensity measured by the MRR is 0.9 mm h^{-1}. Furthermore, 50% of the cold pools are associated with a maximum cloud-top height exceeding 3 km, and w_{maxSCL} and w_{minSCL} of 0.9 m s^{-1} and -0.55 m s^{-1} near the onset and end of the front, respectively. The average cold-pool duration is 33 min, of which a bit more than half of the time pertains to the front. Multiplying the duration with the surface wind speed yields a median cold-pool length larger than 13.3 km.

The IQR shows that all these medians are associated with substantial variability, especially for the humidity and rain variables. However, focusing on the winter regime generally reduces the IQR of the diagnostics compared to all seasons (not shown), suggesting that this criterion indeed results in a more homogeneous cold-pool sample representative of the trade-cumulus regime. The median duration of 33 min and length of about 13.3 km of the cold pools may seem small compared to satellite imagery, in which mesoscale cold-pool arcs can easily span 100 km. Also the largest 2% of cold pools are hardly larger than 40 km. The smaller cold-pool sizes found here are likely due to the algorithm sampling mostly the edge of the cold pools, and due to the challenges of defining the cold-pool end purely based on the surface temperature timeseries (see discussion in Section 2.4).

Table 1 also compares the median$\pm IQR$ of the 25% strongest and weakest cold pools in terms of ΔT. The strongest cold pools last longer, follow each other more quickly (lower Δt_{nextcp}), and are associated with deeper clouds, more rain, stronger downdrafts, humidity drops and wind gusts, and larger positive vertical velocities at the beginning of the front compared to weaker cold pools. Similar but slightly smaller differences between stronger and weaker cold pools are found when comparing cold pools associated with the 25% strongest versus weakest downdrafts or the 25% deepest versus shallowest $CTH_{\max}$ (not shown). The downdraft strength w_{minSCL} is the diagnostic that correlates best with ΔT (R^2=0.23), and together with the front duration it explains a lot of the variability in ΔT for the *noprevWI* set (multiple R^2=0.49). The 25 and 75% quartiles of w_{minSCL} also distinguish the rain diagnostics best.

That $CTH_{\max}$ also distinguishes the cold-pool properties very well indicates that the parent convection triggering the cold pool is sampled well by the single-point measurements. The CTH usually scales with the precipitation amount for trade cumuli (Byers and Hall, 1955; Kubar et al., 2009; Nuijens et al., 2009), so other factors like the environmental humidity do not seem to influence rain evaporation and downdraft strength much further. We also compared the properties of the 25% driest and moistest cold pools in terms of $\Delta q_{\min}$ (not shown), which does not strongly distinguish other cold-pool properties, not even the RR that was shown to be particularly related to $\Delta q_{\min}$ in the literature (Barnes and Garstang, 1982). The specific humidity signal is generally also very variable and the response to the cold-pool onset hard to define in one diagnostic, as will be shown next.

3.2 Composite temporal structure

Figure 3 shows the composite mean temporal structure of the perturbations associated with the cold-pool passages. To facilitate the comparison of different cold pools, we use a normalized time coordinate in the cold-pool front with values mapped onto

https://doi.org/10.5194/acp-2021-420
Preprint. Discussion started: 1 June 2021
© Author(s) 2021. CC BY 4.0 License.

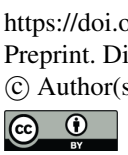

Atmospheric Chemistry and Physics Discussions

20 points (the median front duration), similar to previous studies (Young et al., 1995; de Szoeke et al., 2017; Zuidema et al., 2017).

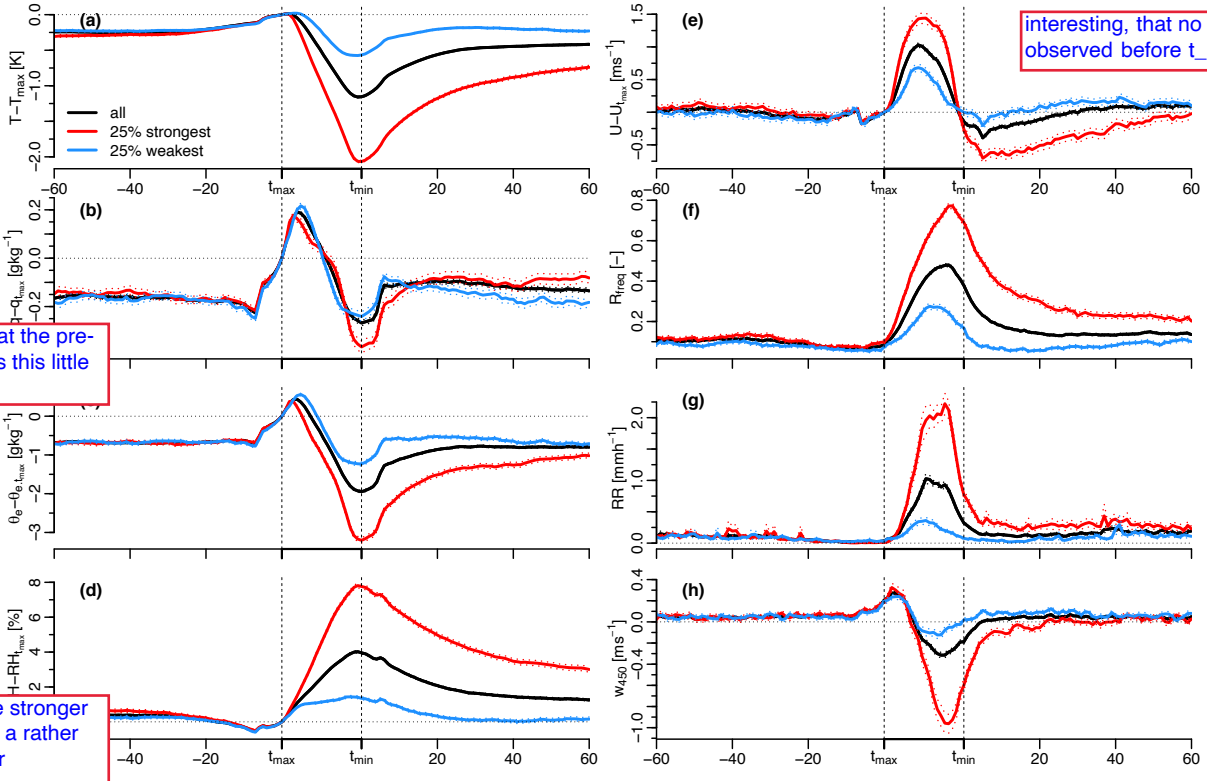

Figure 3. Composite mean temporal structure of anomalies relative to the cold-pool onset ($t_{\max}$) for the surface properties (a) temperature, (b) specific humidity, (c) equivalent potential temperature, (d) relative humidity, and (e) wind speed, as well as absolute values of (f) the MRR rain frequency and (g) rain rate, and (h) the vertical velocity at 450 m height. The black line shows the mean structure of all cold pools matching the *noprevWI* criterion, and the red and blue lines show the mean for the 25% strongest and weakest cold pools, respectively. The dotted lines show the mean±1 SE. Vertical and horizontal reference lines are added to indicate $t_{\max}$, $t_{\min}$ and 0.

The temperature of the composite-mean cold pool, after increasing slightly before $t_{\max}$, decreases rapidly in the front and recovers by $\Delta T/2$ within 16 min after $t_{\min}$. The temperature remains about 0.5 K below T_{max} in the hour after the frontal passage. The temperature drop in the front of the 25% strongest cold pools is by definition stronger, but with a mean tendency of $-0.070\,\mathrm{K\,min^{-1}}$ also more than twice as abrupt compared to the weakest cold pools. The strongest cold pools also take longer to recover than the weakest.

The temporal structure of the specific humidity response is intriguing. The composite-mean humidity starts to increase already 8 min before $t_{\max}$ and increases by about $0.2\,\mathrm{g\,kg^{-1}}$ until $t_{\max}$. In the first quarter of the front, the humidity increases by another $0.2\,\mathrm{g\,kg^{-1}}$, before it drops to its minimum of $-0.25\,\mathrm{g\,kg^{-1}}$ at $t_{\min}$, which is hardly lower than the pre-front value. The humidity recovers much more quickly than the temperature and remains slightly elevated compared to its pre-front value

https://doi.org/10.5194/acp-2021-420
Preprint. Discussion started: 1 June 2021
© Author(s) 2021. CC BY 4.0 License.

Atmospheric Chemistry and Physics Discussions

in the hour after. The fast humidity recovery might be due to the trapping of surface moisture fluxes in the shallow mixed layer typically associated with cold pools (Touzè-Peiffer et al., 2021). Another reason might be continued evaporation of precipitation, which would cool and moisten the air in the cold-pool wake and thus speed up the humidity recovery but slow down the temperature recovery.

The specific humidity response of the strongest cold pools only differs significantly from the weakest cold pools at $t_{\min}$, with the humidity drop at $t_{\min}$ being about $-0.4\,\mathrm{g\,kg^{-1}}$ and thus about twice stronger than the drop for the weakest cold pools. If the entire set of cold pools including the summer season with deeper convection is used, the strongest cold pools have a significantly weaker positive humidity anomaly at the beginning of the front, and a significantly faster and stronger humidity reduction at $t_{\min}$ compared to the weakest cold pools (see Figure B1c-d). As discussed by de Szoeke et al. (2017), the humidity increase just before $t_{\max}$ might be mostly due to the increasing saturation specific humidity associated with the increasing temperature before $t_{\max}$ (as seen by the relative humidity anomaly in panel d being slightly below zero), and as such likely also related to the way we identify $T_{\max}$.

The temporal structure of the equivalent potential temperature is similar to the humidity structure, but with a stronger drop across the front, and a stronger difference between the weaker and stronger cold pools governed by the temperature drops. The relative humidity signal in the front is mostly governed by the temperature decrease, with RH being 8% larger at $t_{\min}$ for the strongest cold pools. The in-front wind speed increase has a maximum in the middle of the front. After the frontal passage, the wind speed decreases slightly below the pre-front level. The strengthening winds in the front and the slackening winds in the wake are again significantly more pronounced for the strongest cold pools, with a maximum of $1.5\,\mathrm{m\,s^{-1}}$ and a minimum smaller $-0.5\,\mathrm{m\,s^{-1}}$ in the front and wake compared to the value at $t_{\max}$. Figure 3f-g show the composite mean R_{freq} and RR measured by the MRR. Both rain variables increase rapidly after the onset of the cold pool, peak towards the middle or end of the front, and start to decrease shortly before $t_{\min}$. The strongest cold pools have much larger rain rates and rain frequencies during the entire front compared to the weakest cold pools, and the rain frequency of the strongest cold pools also remains strongly elevated until more than an hour after $t_{\min}$.

The last panel of Figure 3 shows the Doppler lidar vertical velocity averaged over four 30 m range gates with mean height of 450 m (w_{450}). The mean w_{450} peaks at the edge of the front with about $0.25\,\mathrm{m\,s^{-1}}$ and decreases rapidly to $-0.3\,\mathrm{m\,s^{-1}}$ near the end of the front, reflecting updrafts triggered at the cold-pool gust front and downdrafts driven by the evaporating precipitation inside the front, respectively. The strongest cold pools have significantly stronger downdrafts and also updrafts compared to the weakest cold pools (see also Table 1), the latter highlighting the potentially enhanced triggering of new convection by stronger cold pools. For the vertical velocity averaged over the entire sub-cloud layer (w_{SCL}), the picture is similar, but the peak w_{maxSCL} is slightly smaller for the strongest cold pools and more similar compared to the weaker cold pools (Table 1).

As already shown in Table 1, Figure 3 shows that the strongest cold pools are also the driest and the rainiest, and have the strongest wind and vertical velocity anomalies in the front. The relationships and timings discussed are mostly the same when considering all cold pools meeting the *noprev* criterion (i.e. also including summer periods), just with larger anomalies and the differences mentioned above for the humidity structure. The mean temporal structure for all variables—except for the specific humidity and partly for the wind speed—is also similar to previous observations of tropical deep convective cold pools during

https://doi.org/10.5194/acp-2021-420
Preprint. Discussion started: 1 June 2021
© Author(s) 2021. CC BY 4.0 License.

Atmospheric Chemistry and Physics Discussions

the DYNAMO field campaign (de Szoeke et al., 2017; Chandra et al., 2018), just with slightly smaller anomalies at BCO due to the shallower convection. During DYNAMO, the increases in specific humidity at the beginning of the front are hardly present and the humidity minima near $t_{\min}$ are much more pronounced compared to BCO. The mean in-front wind speed increase is about $2\,\mathrm{m\,s^{-1}}$ and the wind speed also remains elevated in the wake of the DYNAMO cold pools (de Szoeke et al., 2017; Chandra et al., 2018), whereas at BCO it decreases below the value at $t_{\max}$ in the wake. What might strengthen cold pools in the trades despite the shallower parent convection is the drier cloud layer and free troposphere compared to the deep convective regions, which facilitates evaporation of precipitation and can strengthen downdrafts (Chandra et al., 2018).

The initial increase in humidity at the edge of the front at BCO might be explained by enhanced surface fluxes due to the strengthening winds (Langhans and Romps, 2015; Torri and Kuang, 2016), or by an accumulation of moisture from evaporation of precipitation of the parent convection, which was pushed to the edge of the front (Tompkins, 2001). Analyses of the various isotope measurements made during the EUREC^{4}A field campaign (Stevens et al., 2021) might help elucidate the origin of these moisture rings. This could also help understand why cloud-resolving models seem to have difficulties in representing the humidity structure in the cold-pool front correctly (Chandra et al., 2018).

The cloud radars at BCO also allow study of how the cloud properties change across the cold-pool passage (Figure 4). The mean cloud-top height (CTH) increases rapidly by $\sim 500\,\mathrm{m}$ after the cold-pool onset and peaks at the end of the front. CTH remains elevated by $\sim 300\,\mathrm{m}$ compared to the pre-front value in the following hour. The 25% strongest cold pools are associated with significantly deeper clouds throughout the entire period shown, especially so at the end of the front, when the CTH is on average higher than 3300 m. The cloud-base height (CBH) starts to decrease already slightly before $t_{\max}$ and reaches its minimum near the end of the front at $\sim 500\,\mathrm{m}$. This decrease is due to the more frequent precipitation with very low echo-base heights, and is most pronounced for the strongest cold pools.

The total hydrometeor cover (CC) increases rapidly at the beginning of the cold-pool front, remains about 25% larger compared to the pre-front value inside the front, and then decreases slowly in the wake. The mean CC of the 25% strongest cold pools reaches nearly 100% at the end of the front and is significantly larger than the CC of the weakest cold pools during the entire period shown, especially so in the wake. Figure 4d-f show that the enhanced CC of the strongest cold pools in the prior hour is entirely due to cloud segments with CBH above 1 km (CC_{aloft}), whereas the enhanced CC in the front and wake of the strongest cold pools is mostly due to precipitating cloud segments with CBH below 300 m. The rapid increase in CC_{lcl} up to its peak at $t_{\max}$ strongly contributes to the CC increase at the edge of the front. This peak is also larger for the strongest cold pools, consistent with their larger w_{450} at $t_{\max}$. CC_{lcl} and CC_{aloft} are lower at the end of the front for the strongest cold pools, as the lowest CBH is mostly below 300 m and the cloud segments thus count to the CC_{prcp} category (note that a given time can only count to one of the three categories).

In Figure 4d-f the cloud cover is split into contributions from cloud segments with different CBH without accounting for the information of the cloud entity. Based on a similar analysis that accounts for the entity information (see Appendix A), we find that the peak in CC_{lcl} at $t_{\max}$ is mainly due to edges of precipitating clouds that have a $CBH > 300\,\mathrm{m}$. Assuming that this cloud population represents the clouds evident as mesoscale arcs in satellite imagery, this suggests that the cloudiness at the gust front is mostly characterized by well-developed precipitating clouds. The entity analysis also shows that more than

https://doi.org/10.5194/acp-2021-420
Preprint. Discussion started: 1 June 2021
© Author(s) 2021. CC BY 4.0 License.

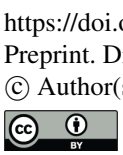

Atmospheric Chemistry and Physics Discussions

355 half of the CC_{aloft} in the cold-pool wake is part of large precipitating clouds, and not from detached stratiform layers. This is also suggested by the time-height plots of the composite-mean hydrometeor fraction shown in Figure 4g-i. These panels nicely summarize what was discussed in the previous paragraphs, and again highlight the differences between the 25% strongest and weakest cold pools in terms of the cloud response.

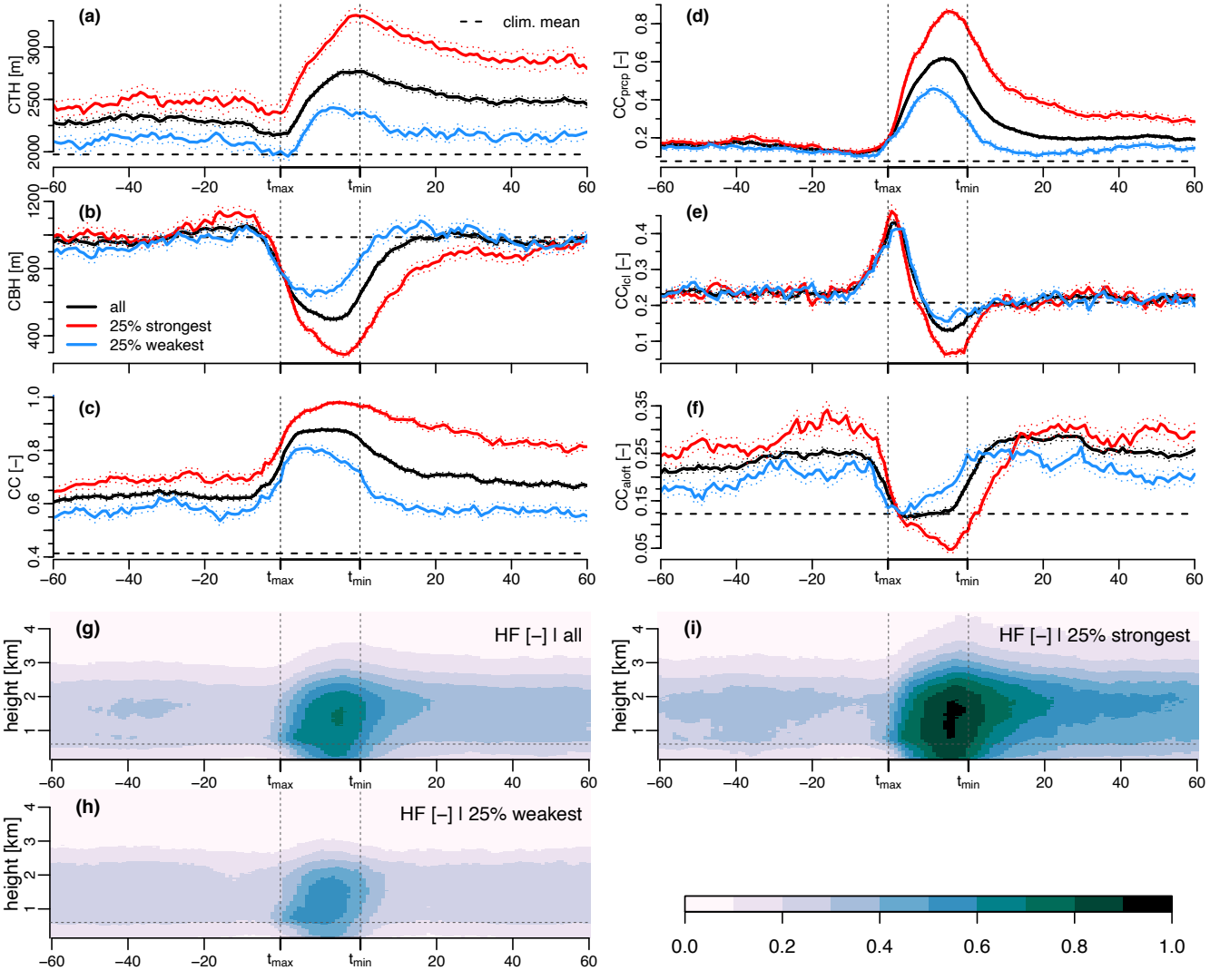

Figure 4. (a-f) Same as Figure 3, but for (a) cloud-top height, (b) cloud-base height, (c) total cloud cover, and the contribution to total cloud cover from (d) CC_{prcp}, (e) CC_{lcl} and (f) CC_{aloft}. Also indicated is the climatological mean value for the winter periods of 2012-2020. (g-i) Composite mean temporal structure of vertical hydrometeor fraction (HF) profiles for all *noprevWI* cold pools, as well as the 25% strongest and weakest. The thin dashed line at 600 m height marks the average cloud-base height.

https://doi.org/10.5194/acp-2021-420
Preprint. Discussion started: 1 June 2021
© Author(s) 2021. CC BY 4.0 License.

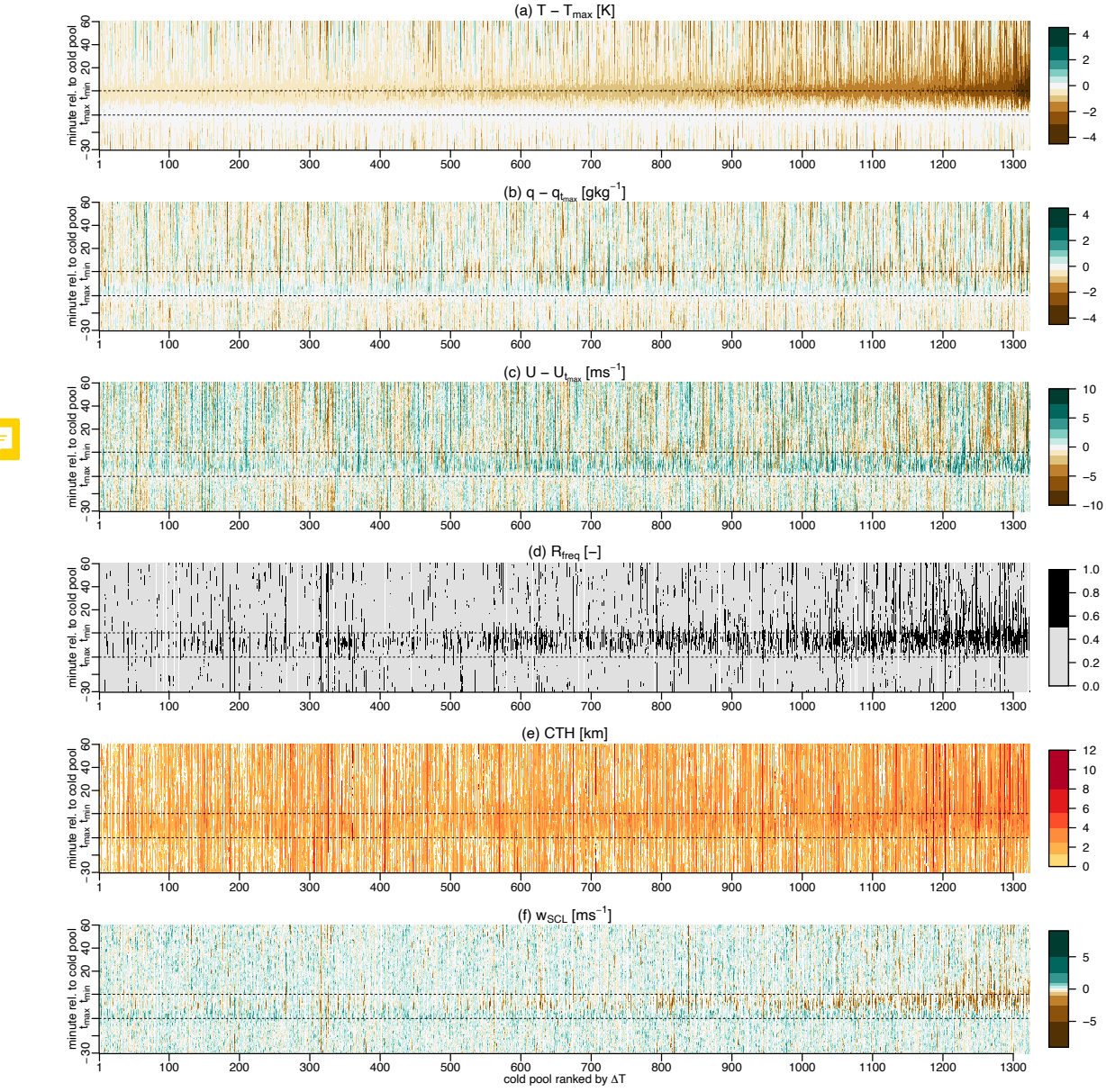

Figure 5. Temporal structure of individual cold pools ranked according to their ΔT. Shown are all cold pools of *noprevWI* that have all instruments running. The panels show anomalies relative to the cold-pool onset ($t_{\max}$) for (a) temperature, (b) specific humidity, and (c) wind speed, as well as absolute values of (d) the MRR rain frequency, (e) the cloud-top height, and (f) the vertical velocity averaged over the sub-cloud layer.

Figure 4a-f also indicate the respective mean CTH, CBH and CCs for all the winter months of the period 2012-2021. They show that cold-pool periods are much cloudier than the average winter trades. Cold-pool periods also have much deeper clouds, which is expected as it needs deeper precipitating clouds to form cold pools. The enhanced CC in the wake of cold

https://doi.org/10.5194/acp-2021-420
Preprint. Discussion started: 1 June 2021
© Author(s) 2021. CC BY 4.0 License.

Atmospheric Chemistry and Physics Discussions

pools compared to the long-term mean is nevertheless surprising, as convection might be expected to be suppressed in the cold-pool wake. Mesoscale arcs encircling vast decks of deeper cumuli with stratiform layers therefore seem more representative for periods of cold-pool activity than the more classical picture of trade cumulus cold pools as mesoscale arcs enclosing broad clear-sky areas.

Despite the various significant differences between the strongest and weakest cold pools highlighted in the previous paragraphs, there is a lot of variability among individual cold pools. The variability is illustrated in Figure 5, which shows the temporal structure of the most important variables for individual cold pools ranked according to their ΔT. Especially the individual differences in humidity and wind in the front and the beginning of the wake can by far exceed the mean differences among the strongest and weakest cold pools shown in Figure 3. Tendencies of more frequent (and intense) rain, deeper clouds and stronger downdrafts near $t_{\min}$ of the stronger cold pools are nevertheless clearly evident. Especially the downdraft strength seems to be systematically increasing for stronger temperature drops. Besides showing the CTH, Figure 5e also gives an indication of the CC, again illustrating how cloudy the cold-pool periods are.

3.3 Daily cycle

The long timeseries also allows to study the variability of the cold-pool frequency and characteristics at the daily timescale. Figure 6 shows the daily variability of cold-pool properties for the *noprevWI* set. There are clearly fewer cold pools and a lower hourly cold-pool frequency between 16–22 LT compared to the rest of the day. Three local maxima in both the cold-pool frequency and number are present at 03, 09 and 14 LT. Also most cold-pool diagnostics show a pronounced daily variability. During nighttime between about midnight and 04 LT, cold pools are associated with significantly deeper clouds, stronger mean rain rates, stronger downdrafts and updrafts, larger CC, and slightly stronger humidity drops and weaker wind gusts compared to daytime cold pools between about 08-16 LT. There is also a hint of slightly stronger ΔT during nighttime compared to daytime, but neither in the median nor in the 25% quartiles is this daily cycle significant. It is somewhat surprising that we find no pronounced daily cycle in ΔT, although the daily cycle of e.g. w_{minSCL} and $CTH_{\max}$ would suggest that ΔT should be stronger at nighttime compared to daytime. There is a climatological background daily cycle in temperature of about 1.2 K due to the daytime solar heating (minimum and maximum temperatures near 5 and 12 LT, respectively), but this should not affect the cloudy cold-pool periods much and would at best contribute to lower ΔT in the morning. Other diagnostics like $\Delta q_{\max}$ and R_{int} do not show a pronounced daily variability (not shown).

The pronounced daily variability in the cold-pool frequency and most diagnostics is not surprising given the distinct daily cycle in trade cumulus cloudiness discussed in detail in Vial et al. (2019) based on both high-resolution simulations and observations. The daily cycle of trade cumuli is characterized by larger CC and deeper clouds at the end of the night and smaller CC and shallower clouds in the afternoon. This is evident in the background climatological daily cycles indicated in Figure 6e-i. The daily cycles of most cold-pool diagnostics have a similar phase and also amplitude as their background daily cycles, but are shifted to much larger values (as indicated in the respective legends). For the vertical velocity diagnostics, also the amplitude of the daily cycle is much larger compared to the background climatology.

https://doi.org/10.5194/acp-2021-420
Preprint. Discussion started: 1 June 2021
© Author(s) 2021. CC BY 4.0 License.

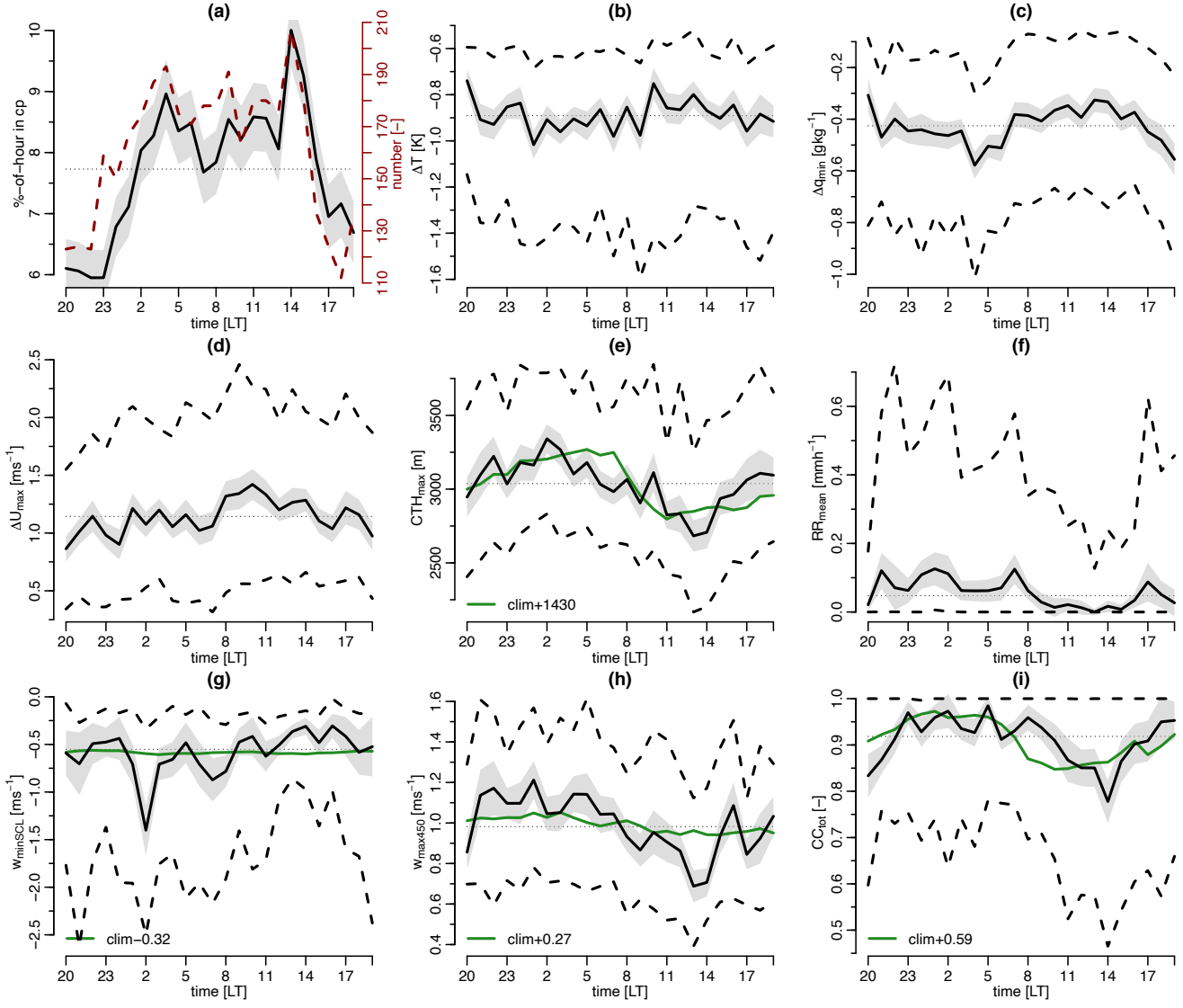

Figure 6. Daily cycles of important cold-pool diagnostics. (a) mean±1 SE of hourly cold-pool frequency as well as the number of cold pools per hour, (b) ΔT, (c) $\Delta q_{\min}$, (d) $\Delta U_{\max}$, (e) $CTH_{\max}$, (f) MRR RR_{mean}, (g) w_{minSCL} and (h) w_{max450}, and (i) CC_{tot}, with cold pools associated to a specific hour according to their $t_{\max}$. In panels b-i the lines represent the 25%, 50%, and the 75% quartiles of the respective variables and the shading represents the median±1 SE. Also indicated in green is the median climatological background daily cycle of 30-min values of (e) maximum CTH, (g) minimum w_{SCL}, (h) maximum w_{450}, and (i) mean CC, shifted by the mean difference of the climatological median compared to the cold-pool median to ease reading. Due to the infrequent rain, the median climatological RR_{mean} is always 0 and omitted in panel f.

The peaks in the cold-pool frequency at 09 and 14 LT are shifted by a few hours compared to the peak in the surface precipitation between 03–06 LT (Nuijens et al., 2009; Vial et al., 2019). This suggests that cold pools help extend the daily

https://doi.org/10.5194/acp-2021-420
Preprint. Discussion started: 1 June 2021
© Author(s) 2021. CC BY 4.0 License.

Atmospheric Chemistry and Physics Discussions

cycle of shallow convection into the early afternoon, which could be due to cold pools reinforcing each other and triggering subsequent cold pools. This hypothesis is supported by the shorter median interval between subsequent cold pools of 121 min between 07-14 LT compared to 182 min between 22-04 LT. Also the daily cycle of cloud cover seems to be slightly extended into the morning, with CC_{tot} decreasing below the daily mean about 4 h later compared to the climatological *CC*.

Vial et al. (2021) also find the daily cycle of trade cumuli to be strongly linked to the daily cycle in the occurrence frequency of the mesoscale organization patterns. Whether the cold-pool characteristics and their daily cycles are related to the pattern of mesoscale organization will be discussed in the next section.

4 Relationship of cold-pool characteristics to mesoscale organization pattern

In this section we investigate whether the cold-pool frequency and characteristics depend on the pattern of mesoscale cloud organization. For this we condition the cold pools on the organization pattern present at BCO. As explained in Section 2.2, a pattern is attributed to a cold pool if it is present during $> 75\%$ of the cold-pool duration. As multiple patterns can be present at the same time, a cold pool can pertain to two (or rarely even three) patterns. Pattern labels are available from January 2018 to March 2021, and using the *noprevWI* criterion we end up with 1332 cold pools to be analysed

The four example cold-pool days in Figure 2 already shed some light on the differences in the cold-pool characteristics of the four patterns. The two Sugar cold pools stem from isolated precipitating deeper cumuli. The satellite image captures the deeper cloud over BCO at the time of the first cold pool and also indicates some organization of the cumuli in lines upstream BCO, while the canonical Sugar fields of shallow cumuli pass further North.

The ~~textbook~~ Gravel day is characterized by many short and often weak cold pools quickly following each other, interspersed by stronger cold pools. The cold pools are associated with the presence of strongly precipitating deeper clouds (note that the radar did not work prior to 12 LT). The many cold pools present on this day clearly imprint their signature on the satellite image in the form of mesoscale arcs.

The cold pools on the Flowers day are associated with the large cloud system whose stratiform layer reaches the BCO at 10 LT. Three cold pools are directly associated with the large system, with the first one starting at 11 LT showing a very strong ΔT of -3.85 K. The large system has rain rates up to 3.6 mm h^{-1} and is announced by a weaker cold pool associated with the very thin mesoscale arc visible in the satellite image, which goes along with a strong increase in humidity of 1.3 g kg^{-1}.

The Fish day features a 6 h long cold pool associated with steady and intense rain (maximum RR of 11.6 mm h^{-1}), continued strong downdrafts and very large humidity throughout its entire duration. The temperature fully recovers within about 20 min of the cold-pool end, and 3 h later two subsequent pronounced cold pools follow that are again characterized by continued precipitation and downdrafts. The satellite image shows the fish-bone like cloud band typically associated with the Fish pattern. The occurrence of the Fish pattern is strongly connected to trailing cold fronts of extratropical origins (Aemisegger et al., 2021; Schulz et al., 2021). The more front-like character of the Fish cold pools with steady showers and downdrafts is clearly evident in the example timeseries.

https://doi.org/10.5194/acp-2021-420
Preprint. Discussion started: 1 June 2021
© Author(s) 2021. CC BY 4.0 License.

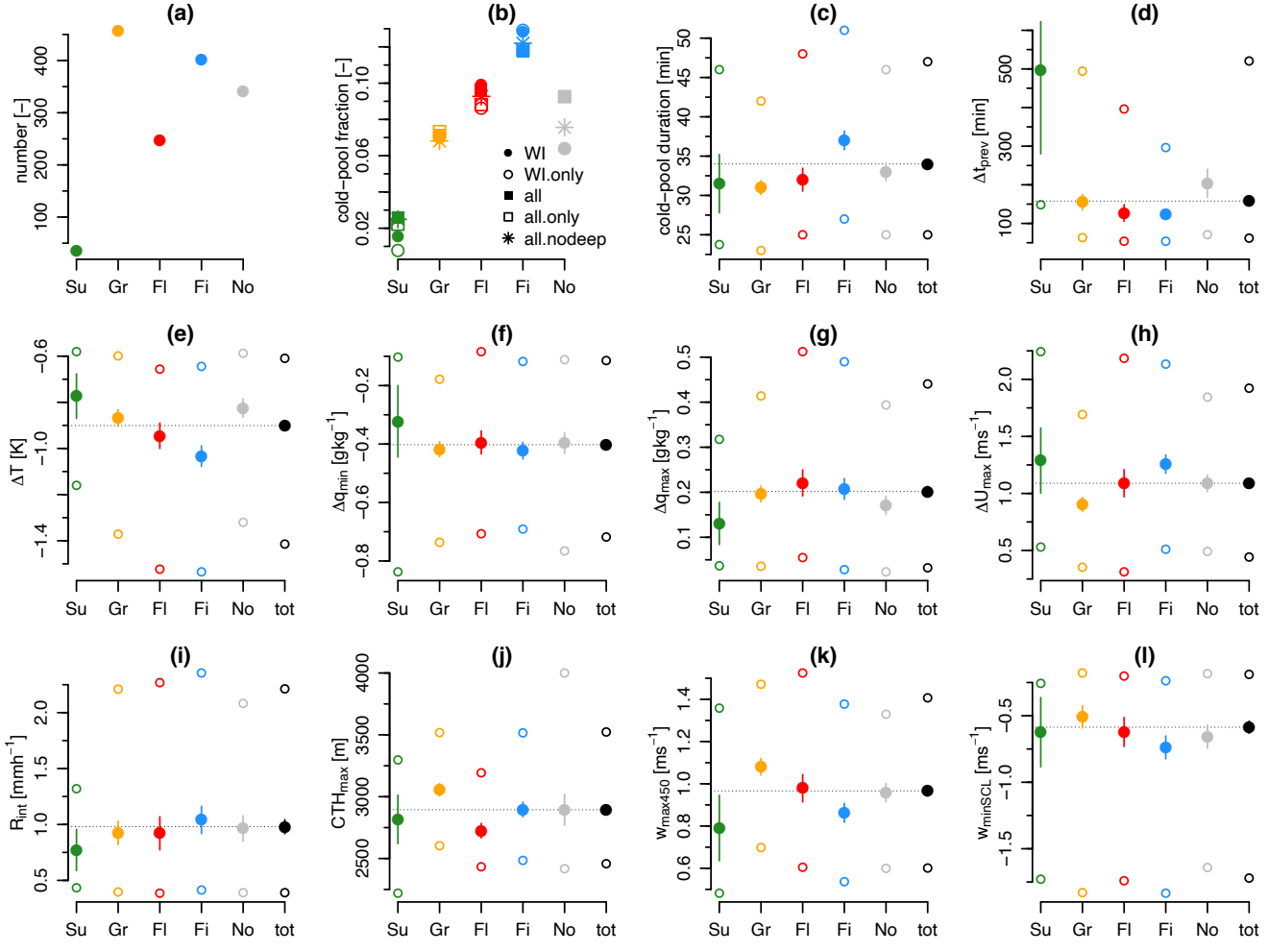

Figure 7. Distributions of various cold-pool diagnostics conditioned on the organization patterns. (a) Number of cold pools, (b) cold-pool fraction, (c) cold-pool duration, (d) time since $t_{\min}$ of the last cold pool, (e) ΔT, (f) $\Delta q_{\min}$, (g) $\Delta q_{\max}$, (h) $\Delta U_{\max}$, (i) MRR R_{int}, (j) $CTH_{\max}$, (k) $w_{\max 450}$ and (l) $w_{\min SCL}$. The different symbols in panels c-l represent the 25%, 50% and 75% quartiles of the respective variables, the solid lines represent the median±1 SE, and the dotted horizontal reference lines show the median of the entire set ('tot'). Besides the cold pools matching the *noprevWI* criterion, panel (b) also shows the fraction of cold pools for all seasons ('all'), for all seasons but without periods of deep convection ('all.nodeep'), and excluding periods with multiple organization patterns ('WI.only' and 'all.only').

Figure 7 shows distributions of several cold-pool properties for the different patterns, including the 'No' category and the union of the five categories ('tot'). The most pronounced difference among the patterns lies in the occurrence frequency of cold pools. Most cold pools detected at BCO pertain to the Gravel pattern (458), followed by Fish (402) and Flowers (248). As expected, only 36 cold pools are detected during Sugar periods. Many cold pools are also associated with the No category (341). When we look at the fraction of time a given pattern is subject to a cold pool, the picture changes and the Fish pattern is

https://doi.org/10.5194/acp-2021-420
Preprint. Discussion started: 1 June 2021
© Author(s) 2021. CC BY 4.0 License.

Atmospheric Chemistry and Physics Discussions

associated with the largest cold-pool fraction (12.8% of time), followed by Flowers and Gravel (9.9% and 724%, respectively). Again, Sugar has clearly the lowest cold-pool fraction (1.6%).

Figure 7b also shows the cold-pool fractions using different selection criteria, namely that only one pattern is allowed at a time (*'.only'*; excluding cold pools that pertain to multiple patterns), that all *noprev* cold pools from all seasons are used (rather than only from the winter months; *'all'*), and that periods of deep convection in all seasons are excluded (*'all.nodeep'*; i.e. no cold pools with any radar signal between 4.5–8 km). For the Gravel pattern, these different criteria hardly influence the cold-pool fraction, whereas for Flowers and Sugar the different sets of criteria tend to change the cold-pool fraction. For Flowers, the cold-pool fraction in winter reduces to 8.6% if periods with multiple patterns and their cold pools are excluded. Only 85 cold pools are left for Flowers.only, while the rest are shared with Gravel (86), Fish (80) and a few also with Sugar (7). While excluding periods of multiple patterns more than halves the cold-pool fraction for Sugar (to 0.8%, mostly due to overlap with the Gravel pattern), considering all seasons nearly doubles the cold-pool fraction of Sugar. Despite these differences, the four patterns remain distinct in their cold-pool fractions independent of the criteria considered. The cold-pool fraction of the No category in winter is with 6.4% also substantial. The No category is particularly sensitive to the inclusion of all seasons, and in summer with more frequent deep convection most cold pools pertain to the No category (not shown). Excluding periods of deep clouds (*'all.nodeep'*) therefore mostly affects the No category, as deep convection is usually absent when patterns are detected.

That Gravel has the largest number of cold pools but only the third largest cold-pool fraction is partly due to Gravel being the most frequent pattern at BCO (a total of 178 days out of the 18 winter months considered, compared to 113 Fish, 78 Flowers and 72 Sugar days), and partly because Gravel cold pools on average last 6 min shorter than Fish cold pools (Figure 7c). With a median duration of 37 min, Fish has the significantly longest-lasting cold pools of all patterns. Cold pools in the Fish case also follow each other most rapidly, with a median of 124 min separating individual cold pool fronts (Figure 7d). Also for Flowers and Gravel do cold pools follow each other quickly, whereas much more time passes between cold pools for Sugar and No. The same picture emerges when considering the cold-pool length (i.e. the duration multiplied by the surface wind speed): Fish cold pools are with a median size of 13.8 km slightly larger than Gravel and Flowers cold pools (both about 12.6 km, not shown).

Figure 7e-i show the differences in the surface meteorology, rain and cloud response associated with cold pools for the different patterns. Fish has the strongest median ΔT and the strongest downdrafts of all patterns, and also a stronger $\Delta U_{\max}$ compared to Gravel and Flowers. Gravel cold pools are associated with significantly larger $CTH_{\max}$ and stronger updrafts compared to the other patterns. For the humidity and rain diagnostics, the differences between Gravel, Flowers and Fish cold pools are minor. Sugar cold pools generally have the weakest cold-pool signatures. Contrastingly, the cold pools of the No category show no significant differences compared to Gravel, Fish and Flowers for most of the statistics.

If cold pools with multiple patterns are excluded, the strongest differences in the diagnostics occur for Flowers and Sugar, as their sample sizes become very small. For Flowers.only cold pools, $\Delta q_{\max}$ is significantly larger compared to the other patterns (not shown), and ΔT becomes comparable to the Fish and $w_{\max 450}$ comparable to Gravel cold pools. The Sugar.only cold-pool sample tends to have smaller cold-pool anomalies compared to when multiple patterns are allowed (except for the median $\Delta U_{\max}$ and $w_{\max 450}$), but the small sample of 11 Sugar.only cold pools does not allow for robust conclusions here. We

https://doi.org/10.5194/acp-2021-420
Preprint. Discussion started: 1 June 2021
© Author(s) 2021. CC BY 4.0 License.

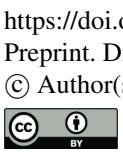

Atmospheric Chemistry and Physics Discussions

find similar differences in the cold-pool samples when the neural network agreement score is increased to 0.5 (instead of the default 0.4).

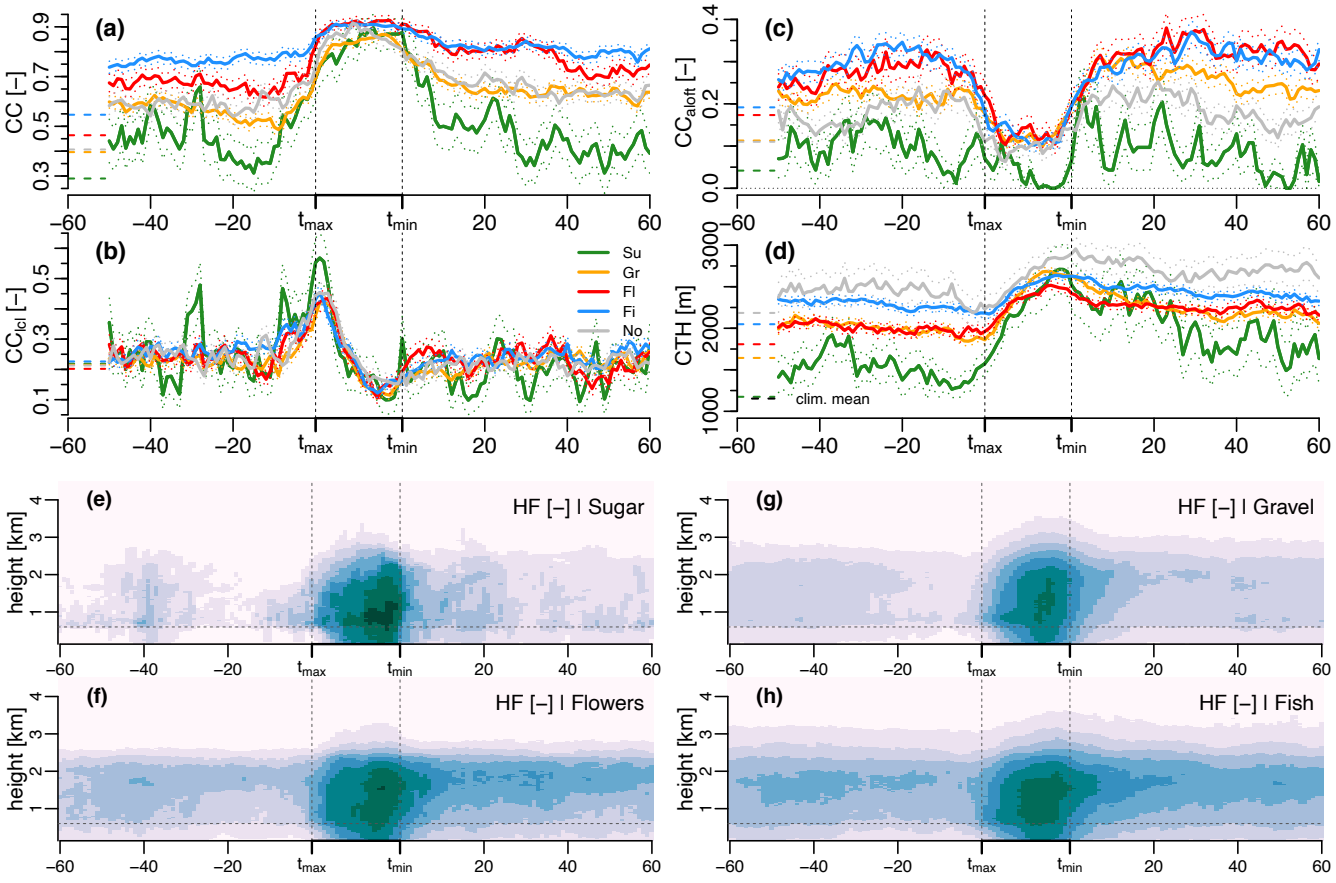

Figure 8. Composite mean temporal structure of the four organization patterns and the No category. Shown are (a) total CC, the contribution to total CC from (b) CC_{lcl} and (c) CC_{aloft}, and (d) the CTH. The dotted lines show the mean$\pm$1 SE. Also indicated on the far-left of panels a-d are the climatological mean values per pattern for the corresponding winter periods of 2018-2021. Panels e-h show the mean temporal structure of the vertical hydrometeor fraction profiles for the four patterns. The colour scale is the same as in Figure 4.

Figure 8a-d shows the differences in the temporal structures of cloud properties for the four patterns. They show that also during the cold-pool periods, the climatological differences in CC and CTH among the different patterns remain (see also Schulz et al., 2021; Vial et al., 2021; Bony et al., 2020). Fish has the largest CC, closely followed by Flowers[1], and then Gravel and Sugar. The CC differences are mostly due to the differing contributions of CC_{aloft}, whereas CC_{lcl} is fairly similar among the patterns both for the cold-pool periods and the climatological mean (Schulz et al., 2021). Also the temporal structure of

[1]Whether Fish or Flowers have the larger mean CC depends on the dataset and the period considered (Bony et al., 2020; Schulz et al., 2021; Vial et al., 2021)

https://doi.org/10.5194/acp-2021-420
Preprint. Discussion started: 1 June 2021
© Author(s) 2021. CC BY 4.0 License.

Atmospheric Chemistry and Physics Discussions

CC_{prcp} is similar for all patterns during the cold-pool period (not shown), and resembles the mean structure of all cold pools shown in Figure 3d. For all patterns, the cold-pool periods are characterized by significantly deeper clouds and larger CC compared to the pattern average.

The CC of Fish cold pools hardly changes across the cold-pool passage, whereas the onset of the cold-pool front is much more clearly evident for the Gravel and even more for the Sugar CC. The CC in the wake of Sugar cold-pools also decreases most rapidly back to its pre-front value. Fish also tends to have the deepest mean CTH associated with the cold-pool periods, closely followed by Gravel and Flowers. The mean CTH of Gravel cold pools increases more rapidly in the front compared to Flowers and Fish, but also decreases a bit faster in the wake of the cold pools. Again, the cold-pool onset has the strongest CTH imprint for the Sugar pattern, with a mean CTH increase exceeding 1 km between t_{max} and t_{min}.

The differences in the cloud properties of the different patterns associated with the cold-pool passages are again summarized in the time-height composite hydrometeor fraction plots (Figure 8e-h). They show the strongly enhanced CC_{aloft} of Fish and Flowers cold pools that is mostly associated with more frequent stratiform layers near 1.5-2 km. The more pronounced influence of the cold-pool onset on the CC and CTH for Sugar and Gravel compared to Flowers and Fish, as well as the overall higher CTH for Fish are also clearly evident.

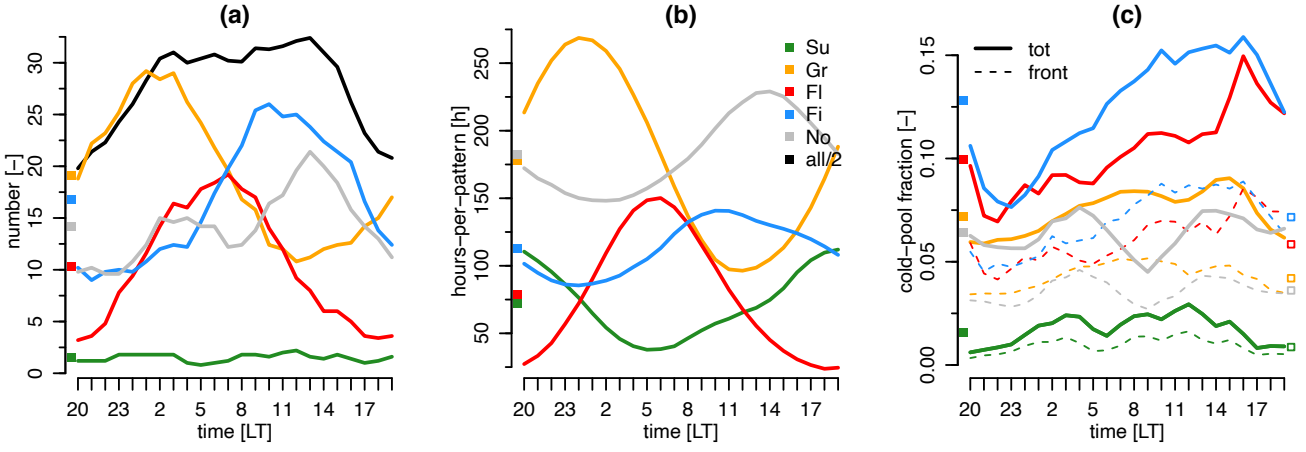

Figure 9. Daily cycles of (a) number of cold pools, (b) hours of data for the different organization patterns, and (c) hourly fraction in cold pool (solid) and in cold-pool front (dashed). A 5-hourly running mean is applied to smooth the data. The daily means are indicated on the left side of each panel.

As mentioned before, Vial et al. (2021) find the daily cycle of trade cumuli to be strongly linked to the daily cycle in the occurrence frequency of the mesoscale organization patterns. Figure 9a shows strong daily variations of the number of cold pools associated with the different patterns. These variations are strongly connected to the daily cycles in the occurrence frequency of the patterns (Figure 9b and Vial et al., 2021). The maximum number of Gravel cold pools occurs just after midnight, followed by Flowers around 7 LT, and Fish cold pools at 10 LT. The number of Sugar cold pools is very low throughout the day.

https://doi.org/10.5194/acp-2021-420
Preprint. Discussion started: 1 June 2021
© Author(s) 2021. CC BY 4.0 License.

Atmospheric Chemistry and Physics Discussions

Figure 9a suggests that the extension of the daily cycle of convection into the early afternoon due to cold pools may largely be explained by the Fish pattern, together with a substantial contribution of the No category to the peak at 14 LT. Despite the strong connection between the daily phasings of Figure 9a-b, especially the Fish pattern also shows a daily cycle of the cold-pool fraction with a peak in the afternoon (Figure 9c), which is broadly in phase with the occurrence frequency. The daily cycle in the cold-pool fraction might be due to cold pools lasting a while once they are formed, which is supported by the much weaker daily cycles of the cold-pool *front* fraction (dashed lines in Figure 9c). Once present, cold pools often trigger new cold pools, as indicated by the 33% shorter interval between subsequent fronts during daytime compared to nighttime (see discussion in Section 3.3). From the present analyses, it is difficult to disentangle causal relationships between the pattern occurrence, cold pools, and the daily cycle. It is also difficult to pin down the evolution from one pattern to another, and the role of cold pools therein. As the number of cold pools per pattern and hour is quite low (especially in the case of Flowers), more data is needed to draw robust conclusions on this.

The pattern-associated daily phasing of the cold-pool number might give a clue about why ΔT varies little on the daily timescale (Figure 6c), although the daily cycle of most cold-pool properties would suggest that ΔT should be stronger at night compared to day. The daytime Fish pattern has significantly stronger ΔT compared to the nighttime Gravel pattern (Figure 7e), which might compensate for the opposite expectation due to the daily phasing of $CTH_{\max}$ and w_{minSCL}.

5 Conclusions

This paper presents a longterm climatology of trade cumulus cold pools based on more than ten years of in-situ and ground-based remote sensing data from the Barbados Cloud Observatory (BCO; Stevens et al., 2016). Cold pools are detected by abrupt drops in low-pass filtered temperature timeseries and their associated changes in surface meteorology, cloudiness and sub-cloud layer dynamics are extracted. The cold-pool climatology is combined with a neural network classification of the four mesoscale organization patterns Sugar, Gravel, Flowers and Fish (Stevens et al., 2020) based on GOES-16 ABI infrared images (Schulz et al., 2021). To focus on trade cumulus cold pools, most analyses are restricted to the set of 3889 cold pools detected in the dry winter regime from December to April that have no non-recovered cold pool in the hour prior to their onset.

We find cold pools to be ubiquitous in the winter trades—they are present about 7.8% of the time and on more than 73% of days at least one cold pool is detected. The average cold-pool passage is characterized by a 0.9 K temperature drop, a 0.2 g kg^{-1} humidity increase at the onset and a -0.4 g kg^{-1} humidity decrease at the end of the front, wind speed increases of 1.15 m s^{-1}, and rain intensities of 0.9 mm h^{-1}. The vertical velocity at the sub-cloud layer top shows a pronounced peak of 1 m s^{-1} near the cold-pool onset and sub-cloud layer averaged downdrafts of -0.55 m s^{-1} near the end of the front. Strong signals of cold-pool passages are also found for all cloud macrophysical properties analysed: cloud-top height increases, cloud-base height decreases (due to the very frequent precipitation), and cloud cover increases with the cold-pool onset. Cloudiness at the gust front is mostly due to cloud segments near the lifting-condensation level that pertain to larger precipitating cloud entities. Similarly, cloud segments with bases above 1 km in the cold-pool wake are mostly part of large precipitating clouds, and not from detached stratiform layers.

https://doi.org/10.5194/acp-2021-420
Preprint. Discussion started: 1 June 2021
© Author(s) 2021. CC BY 4.0 License.

Atmospheric Chemistry and Physics Discussions

The strength of the cold-pool signature depends strongly on the intensity of the temperature drops (ΔT). Cold pools with stronger ΔT are associated with deeper clouds, stronger precipitation, downdrafts, and humidity drops, stronger wind gusts and updrafts at the edge of the front, and larger cloud cover compared to cold pools with weaker ΔT. Stronger cold pools also last significantly longer and follow each other more quickly than weaker cold pools. We find that also the minimum vertical velocity averaged over the sub-cloud layer and the maximum cloud-top height distinguish stronger and weaker cold pools very well. Especially the downdraft strength is a very robust indicator of cold-pool strength and together with the cold-pool front duration it explains 50% of the variability in ΔT.

The cold-pool frequency and characteristics also show pronounced daily variability. There are significantly less cold pools and a lower cold-pool frequency between 16-22 LT compared to the rest of the day. We find that cold pools extend the daily cycle of convection into the early afternoon, with a peak in both the cold-pool number and fraction at 14 LT. Also most cold-pool diagnostics show a pronounced daily cycle, with significantly deeper clouds, stronger mean rain rates, stronger downdrafts and updrafts, larger cloud cover, slightly stronger humidity drops and weaker wind gusts associated with nighttime compared to daytime cold pools. The phase of these daily signatures is consistent with their background climatological daily cycle, but shifted to much larger values. For the vertical velocity minima and maxima, also the amplitude of the daily cycle is much more pronounced during cold-pool periods.

In the wet summer regime, cold-pools are about 30% more frequent relative to the average winter regime. Summer cold pools are also associated with significantly stronger temperature and humidity drops, deeper clouds and stronger downdrafts—consistent with the frequent deep convection and stronger precipitation of this season (Brueck et al., 2015). On the other hand, the summer cold pools have weaker updrafts and humidity maxima at the beginning of the front, suggesting that they might be less effective in triggering new convection. While the temporal structure of cold-pool passages for most meteorological variables in both seasons resemble those of previous observations of tropical deep convective cold pools (de Szoeke et al., 2017; Chandra et al., 2018; Zuidema et al., 2017), especially the humidity structure and also the generally larger anomalies render the summer cold pools more similar to the deep convective cold pools from previous studies.

We also analysed if the cold-pool frequency and characteristics depend on the pattern of mesoscale cloud organization. The most pronounced difference among the patterns lies in the occurrence frequency of cold pools, with Fish having the largest cold-pool fraction (12.8% of time), followed by Flowers and Gravel (9.9% and 7.2%, respectively). As expected, the cold-pool fraction of Sugar is negligible (1.6%). Fish cold pools last significantly longer than cold pools from all the other patterns, and they are also associated with the strongest temperature drops and downdrafts. Gravel cold pools are associated with the strongest updrafts at the cold-pool onset and the deepest cloud-top height maxima.

Given the distinct daily cycle in the occurrence frequency of the four patterns found in Vial et al. (2021), it is not surprising that we find strong daily variations of the number of cold pools associated with the different patterns. The maximum number of Gravel cold pools occurs around midnight, followed by Flowers around 7 LT, and Fish cold pools around 10 LT, in line with the daily cycles in the occurrence frequency of the patterns. The Gravel, Flowers and Fish cold pools can thus explain a large fraction of the daily cycle in the cold-pool occurrence, as well as their extension into the early afternoon. Note also that the unclassified cold pools have a non-negligible contribution to the peak at 14 LT. Interestingly, the climatological differences in

https://doi.org/10.5194/acp-2021-420
Preprint. Discussion started: 1 June 2021
© Author(s) 2021. CC BY 4.0 License.

Atmospheric Chemistry and Physics Discussions

the cloud cover and cloud-top height among the different patterns are also present during cold-pool periods—the overall cloud cover and cloud-top height for all patterns is just enhanced compared to their respective climatological values.

This study paves the way for more in-depth analyses of the cold-pool properties and their relation to the environment in the trades. Especially the complex humidity signals deserve a more detailed investigation, also using data from the recent EUREC^{4}A field campaign (Stevens et al., 2021) and from realistic large-eddy simulations. Together with the vertical velocity statistics, the humidity anomalies can help shed light on the triggering of new convection at the cold-pool front Additional measurements of the mixed-layer depth from radiosondes and the Raman or Doppler lidar could help refine the cold-pool end definition, which is only poorly constrained by the surface temperature data. Such additional data could also provide interesting insight into the cold-pool recovery process. A systematic matching with satellite imagery would also help collocate the clouds sampled at BCO with the broader view of the entire cold pool seen from space.

Overall, we find that the cold-pool periods are about 90% cloudier relative to the average winter trades. The larger cloudiness is mostly due to larger cloud cover from precipitating and stratiform cloud segments. Also the wake of cold pools is characterized by above average cloudiness, indicating that the classical image of trade cumulus cold pools as mesoscale arcs enclosing broad clear-sky areas is rather the exception than the rule. Our study suggests that a better understanding of how trade-cumulus cold pools interact with and shape their environment is important to understand the variability in cloud cover and cloud organization in the trade-wind regime.

Code and data availability. The BCO data used in the analysis and other supplementary information that may be useful to reproduce the present study are avalaible from the first author on request. The GOES-16 ABI data are publicly available online at doi.org/10.7289/V5BV7DSR. The satellite images in Figure 2 are retrieved from the imagery of the Earth Observing System Data and Information System (EOSDIS) Worldview Snapshots application (https://wvs.earthdata.nasa.gov, last access: 21 March 2021), and from the NASA ATOMIC-EUREC^{4}A GOES-16 ABI imagery (https://satcorps.larc.nasa.gov/cgi-bin/site/showdoc?docid=22&lkdomain=Y&domain=FEXP-ATOMIC-SATIMG, last access 21 March 2021).

Appendix A: Cloud cover contributions from different types of cloud entities

The contributions to total cloud cover from clouds at different height levels can either be computed by classifying every radar profile independently based on its CBH (see Figure 4d-f), or—if a cloud segmentation mask is available—by classifying the entire cloud entities according to their cbh_{ID} (i.e. their overall lowest CBH). As both approaches can provide valuable insights, Figure A1 also shows the temporal structure of the cold-pool signatures for the latter classification method. For this, the cloud cover is again split up into contributions from precipitating clouds with $cbh_{\mathrm{ID}} \leq 300\,\mathrm{m}$ ($CC_{\mathrm{ID.prcp}}$), LCL clouds ($CC_{\mathrm{ID.lcl}}$; $300\,\mathrm{m} < cbh_{\mathrm{ID}} \leq 1\,\mathrm{km}$), and stratiform clouds ($CC_{\mathrm{ID.aloft}}$; $1\,\mathrm{km} < cbh_{\mathrm{ID}} \leq 4\,\mathrm{km}$). The difference between $CC_{\mathrm{ID.prcp}}$ and CC_{prcp} is that edges or slanted sides of precipitating clouds that have a $CBH > 300\,\mathrm{m}$ are counted in their entirety to the $CC_{\mathrm{ID.prcp}}$ category, while they would be counted in the CC_{lcl} or CC_{aloft} category if the cloud ID was not considered. Due to

https://doi.org/10.5194/acp-2021-420
Preprint. Discussion started: 1 June 2021
© Author(s) 2021. CC BY 4.0 License.

Atmospheric Chemistry and Physics Discussions

the potential presence of cloud entities at different heights, the sum of the three height categories ($CC_{\mathrm{ID.tot}}$) can be larger than one.

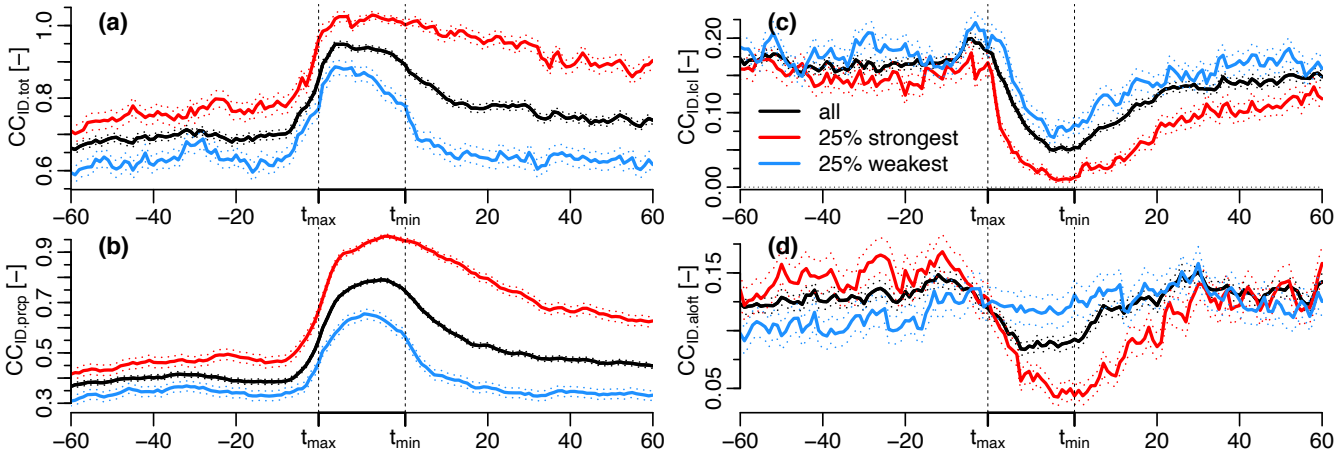

Figure A1. Same as Figure 3, but for (a) $CC_{\mathrm{ID.tot}}$, (b) $CC_{\mathrm{ID.prcp}}$, (c) $CC_{\mathrm{ID.lcl}}$, (d) $CC_{\mathrm{ID.aloft}}$, for all cold pools of *noprevWI* and the 25% strongest and weakest cold pools.

$CC_{\mathrm{ID.prcp}}$ already starts to increase before t_{max} and continues to increase until the middle of the front for all the cold-pool sets shown. For the 25% strongest cold pools, the end of the front is entirely covered by precipitating clouds. $CC_{\mathrm{ID.lcl}}$ in Figure A1c for all sets is relatively stable at about 17.5% before the cold-pool onset, decreases abruptly after t_{max} to a minimum near t_{min}, and then slowly recovers back to the pre-front value. $CC_{\mathrm{ID.lcl}}$ shows the strongest impact when the cloud entities are considered through the cbh_{ID} and thus the strongest difference to the structure of CC_{lcl} (Figure 4e). The absence of a peak in $CC_{\mathrm{ID.lcl}}$ near t_{max} indicates that the CC_{lcl} peak there is almost entirely due to edges of precipitating clouds with a $CBH > 300$ m, and not due to (not-yet or) non-precipitating trade cumuli.

The temporal structure of $CC_{\mathrm{ID.aloft}}$ resembles the structure of CC_{aloft} (Figure 4f), yet with substantially lower coverage as most cloud segments with $CBH > 1$ km are connected to a precipitating core. This shows that nearly half of the CC_{aloft} in the cold-pool wake is part of large precipitating clouds, and not from detached stratiform layers.

Appendix B: Seasonal cycle of cold-pool characteristics

While this study focuses on the cold-pool climatology of the winter regime, it is also interesting to look at the seasonal cycle of the cold-pool characteristics at BCO. Using all cold pools of the *noprev* category, we find the largest median *%-of-day in cold pool* in the summer months from July-November, and another peak in January (Figure B1a). Only 13% of days have no cold pool at all in summer, compared to 27% in winter. The same monthly variability is found for the *%-of-day in front*, but with 45% lower values due to the shorter duration of the front compared to the entire cold pool (not shown).

https://doi.org/10.5194/acp-2021-420
Preprint. Discussion started: 1 June 2021
© Author(s) 2021. CC BY 4.0 License.

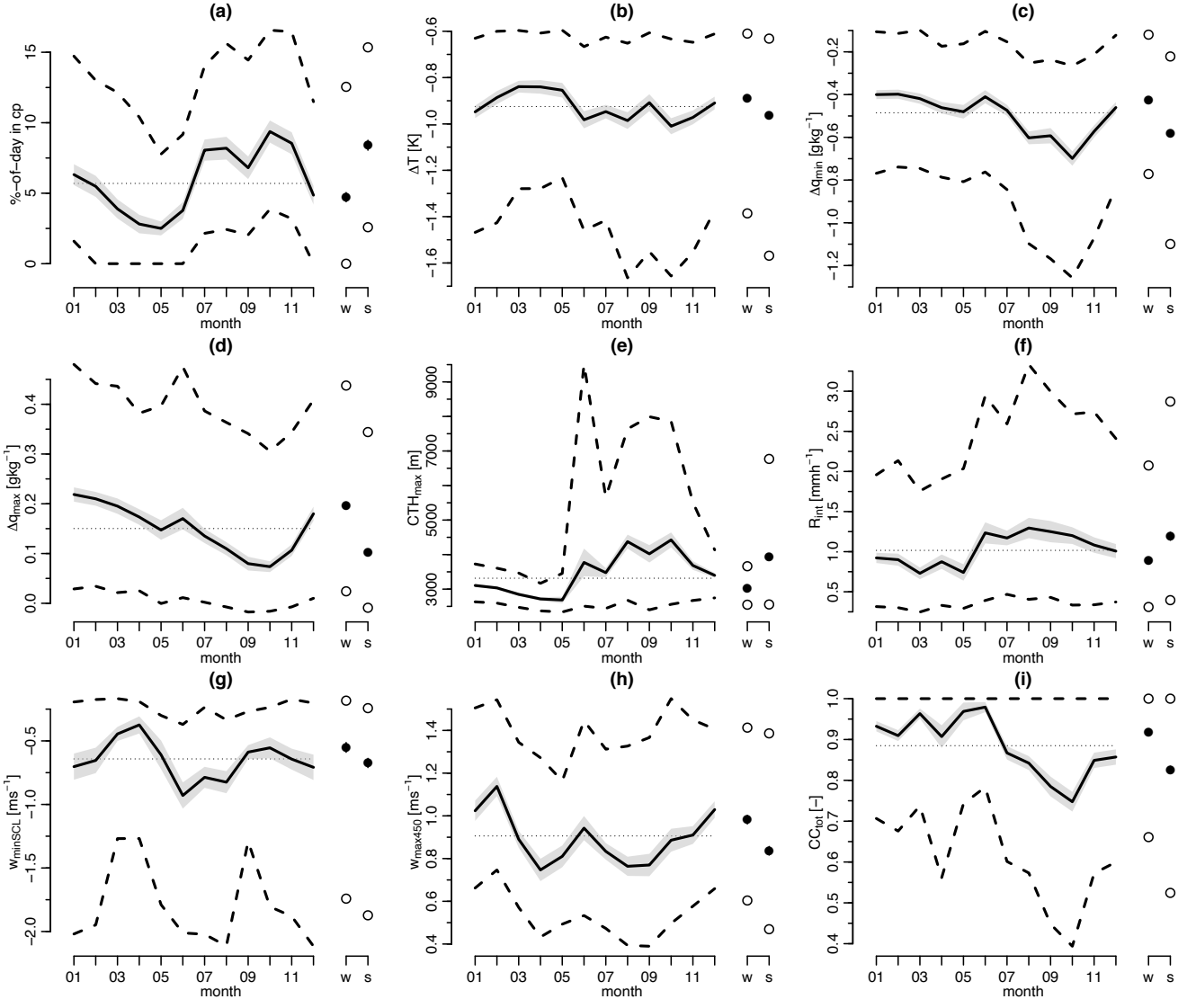

Figure B1. Monthly and seasonal distribution of important cold-pool diagnostics. (a) *%-of-day in cold-pool*, (b) ΔT, (c) $\Delta q_{\min}$, (d) $\Delta q_{\max}$, (e) $CTH_{\max}$, (f) MRR R_{int}, (g) w_{minSCL} and (h) w_{max450}, and (i) CC_{tot}. The lines represent the 25%, 50%, and the 75% quartiles of the respective variables, the shading represents the median$\pm$1 SE, and the points show the average distribution for the five winter (w; December-April) and summer months (s; July-November).

Figure B1b-i show the monthly distributions of various cold-pool properties, as well as averages over the five winter and summer months, respectively. They show that the summer cold pools are on average characterized by significantly stronger $\Delta q_{\min}$, $CTH_{\max}$ and R_{int}, as well as slightly stronger ΔT and w_{minSCL}, consistent with the relationships discussed in Section 3. However, w_{max450} is significantly lower by 0.2 m s^{-1} and $\Delta q_{\max}$ by 0.1 g kg^{-1} in summer compared to winter, indicating that cold pools in summer might be less successful in triggering new convection. Furthermore, CC_{tot} of summer cold pools

https://doi.org/10.5194/acp-2021-420
Preprint. Discussion started: 1 June 2021
© Author(s) 2021. CC BY 4.0 License.

Atmospheric Chemistry and Physics Discussions

is also significantly smaller compared to winter cold pools by about 10%. The differences in the cold-pool characteristics between the summer and winter regime are not surprising, as the summer regime is referred to as the *wet* season in Barbados and characterized by frequent deep convection and much larger precipitation (Brueck et al., 2015). When excluding periods of deep convection (defined by the presence of a radar signal between 4.5–8 km), the number of cold pools detected in summer strongly decreases compared to winter, and the median summer cold pool also becomes weaker compared to the median winter cold pool (not shown).

Author contributions. RV initiated the project in exchange with PZ. HK prepared the radar cloud mask and HS the neural network classifications of the organization patterns. RV developed the cold-pool detection algorithm, performed the analyses and wrote the manuscript. All co-authors contributed to the interpretation of the results and commented on the manuscript.

Competing interests. The authors declare that they have no conflict of interest.

Acknowledgements. Many thanks go to the Tropical Cloud Observation group at MPI for maintaining the BCO infrastructure. We thank Nicolas Rochetin, Ludovic Touzé-Pfeiffer, Cathy Hohenegger, Bjorn Stevens, and the EUREC^{4}A science team at LMD and MPI for interesting discussions. RV thanks Louise Nuijens for motivating to look at cold pools at end of the PhD thesis. RV acknowledges funding from the European Research Council (ERC) under the European Union's Horizon 2020 research and innovation programme (grant agreement No 694768). HK has received funding from HALO SPP (DFG HALO SPP 1294). PZ acknowledges support from NOAA Climate Program Office award NA19OAR4310379.

https://doi.org/10.5194/acp-2021-420
Preprint. Discussion started: 1 June 2021
© Author(s) 2021. CC BY 4.0 License.

Atmospheric Chemistry and Physics Discussions

References

Aemisegger, F., Vogel, R., Graf, P., Dahinden, F., Villiger, L., Jansen, F., Bony, S., Stevens, B., and Wernli, H.: How Rossby wave breaking modulates the water cycle in the North Atlantic trade wind region, Weather and Climate Dynamics, 2, 281–309, https://doi.org/10.5194/wcd-2-281-2021, 2021.

Barnes, G. M. and Garstang, M.: Subcloud layer energetics of precipitating convection, Mon. Wea. Rev., 110, 102–117, 1982.

Bony, S. and Dufresne, J.-L.: Marine boundary layer clouds at the heart of tropical cloud feedback uncertainties in climate models, Geophys. Res. Lett., 32, L20 806, https://doi.org/10.1029/2005GL023851, 2005.

Bony, S., Stevens, B., Ament, F., Bigorre, S., Chazette, P., Crewell, S., Delanoë, J., Emanuel, K., Farrell, D., Flamant, C., Gross, S., Hirsch, L., Karstensen, J., Mayer, B., Nuijens, L., Ruppert, J. H., Sandu, I., Siebesma, P., Speich, S., Szczap, F., Totems, J., Vogel, R., Wendisch, M., and Wirth, M.: EUREC4A: A Field Campaign to Elucidate the Couplings Between Clouds, Convection and Circulation, Surveys in Geophysics, https://doi.org/10.1007/s10712-017-9428-0, 2017.

Bony, S., Schulz, H., Vial, J., and Stevens, B.: Sugar, Gravel, Fish, and Flowers: Dependence of Mesoscale Patterns of Trade-Wind Clouds on Environmental Conditions, Geophysical Research Letters, 47, e2019GL085 988, https://doi.org/10.1029/2019GL085988, 2020.

Brueck, M., Nuijens, L., and Stevens, B.: On the seasonal and synoptic time-scale variability of the north atlantic trade wind region and its low-level clouds, J. Atmos. Sci., 72, 1428–1446, https://doi.org/10.1175/JAS-D-14-0054.1, 2015.

Byers, H. R. and Hall, R. K.: A census of cumulus-cloud height versus precipitation in the vicinity of Puerto Rico during the winter and spring of 1953-1954, Journal of the Atmospheric Sciences, 12, 176–178, https://doi.org/10.1175/1520-0469(1955)012<0176:ACOCCH>2.0.CO;2, 1955.

Chandra, A. S., Zuidema, P., Krueger, S., Kochanski, A., de Szoeke, S. P., and Zhang, J.: Moisture Distributions in Tropical Cold Pools From Equatorial Indian Ocean Observations and Cloud-Resolving Simulations, Journal of Geophysical Research: Atmospheres, 123, 11,445–11,465, https://doi.org/10.1029/2018JD028634, 2018.

de Szoeke, S. P., Skyllingstad, E. D., Zuidema, P., and Chandra, A. S.: Cold Pools and Their Influence on the Tropical Marine Boundary Layer, Journal of the Atmospheric Sciences, 74, 1149 – 1168, https://doi.org/10.1175/JAS-D-16-0264.1, 2017.

Feng, Z., Hagos, S., Rowe, A. K., Burleyson, C. D., Martini, M. N., and de Szoeke, S. P.: Mechanisms of convective cloud organization by cold pools over tropical warm ocean during the AMIE/DYNAMO field campaign, Journal of Advances in Modeling Earth Systems, 7, 357–381, https://doi.org/https://doi.org/10.1002/2014MS000384, 2015.

GOES-R Calibration Working Group and GOES-R Series Program: NOAA GOES-R Series Advanced Baseline Imager (ABI) Level 1b Radiances, https://doi.org/10.7289/V5BV7DSR, online; accessed on 15 July 2020, 2017.

Klingebiel, M., Ghate, V. P., Naumann, A. K., Ditas, F., Pöhlker, M. L., Pöhlker, C., Kandler, K., Konow, H., and Stevens, B.: Remote Sensing of Sea Salt Aerosol below Trade Wind Clouds, Journal of the Atmospheric Sciences, 76, 1189 – 1202, https://doi.org/10.1175/JAS-D-18-0139.1, 2019.

Konow, H.: BCO Cloudmask Code, https://doi.org/10.5281/zenodo.4312818, 2020.

Kubar, T. L., Hartmann, D. L., and Wood, R.: Understanding the Importance of Microphysics and Macrophysics for Warm Rain in Marine Low Clouds. Part I: Satellite Observations, Journal of the Atmospheric Sciences, 66, 2953–2972, https://doi.org/10.1175/2009JAS3071.1, 2009.

Langhans, W. and Romps, D. M.: The origin of water vapor rings in tropical oceanic cold pools, Geophysical Research Letters, 42, 7825–7834, 2015.

https://doi.org/10.5194/acp-2021-420
Preprint. Discussion started: 1 June 2021
© Author(s) 2021. CC BY 4.0 License.

Atmospheric Chemistry and Physics Discussions

Lin, T., Goyal, P., Girshick, R. B., He, K., and Dollár, P.: Focal Loss for Dense Object Detection, CoRR, abs/1708.02002, http://arxiv.org/abs/1708.02002, 2017.

Medeiros, B. and Nuijens, L.: Clouds at Barbados are representative of clouds across the trade wind regions in observations and climate models, Proceedings of the National Academy of Sciences, 113, E3062–E3070, https://doi.org/10.1073/pnas.1521494113, 2016.

Nuijens, L., Stevens, B., and Siebesma, A. P.: The environment of precipitating shallow cumulus convection, J. Atmos. Sci., 66, 1962–1979, 2009.

Nuijens, L., Serikov, I., Hirsch, L., Lonitz, K., and Stevens, B.: The distribution and variability of low-level cloud in the North Atlantic trades, Quart. J. Roy.Meteor.Soc., 140, 2364–2374, https://doi.org/10.1002/qj.2307, 2014.

Rasp, S., Schulz, H., Bony, S., and Stevens, B.: Combining Crowdsourcing and Deep Learning to Explore the Mesoscale Organization of Shallow Convection, Bulletin of the American Meteorological Society, 101, E1980–E1995, https://doi.org/10.1175/BAMS-D-19-0324.1, 2020.

Rochetin, N., Hohenegger, C., Touzé-Peiffer, L., and Villafranque, N.: A physically-based robust definition of convectively generated density currents: detection and characterization in convection-permitting simulations, submitted to JAMES, 2021.

Rowe, A. K. and Houze Jr., R. A.: Cloud organization and growth during the transition from suppressed to active MJO conditions, Journal of Geophysical Research: Atmospheres, 120, 10,324–10,350, https://doi.org/10.1002/2014JD022948, 2015.

Schlemmer, L. and Hohenegger, C.: The Formation of Wider and Deeper Clouds as a Result of Cold-Pool Dynamics, J. Atmos. Sci., 71, 2842–2858, https://doi.org/10.1175/JAS-D-13-0170.1, 2014.

Schulz, H., Eastman, R. M., and Stevens, B.: Characterization and Evolution of Organized Shallow Convection in the Trades, https://doi.org/10.1002/essoar.10505836.1, 2021.

Stevens, B., Farrell, D., Hirsch, L., Jansen, F., Nuijens, L., Serikov, I., Brügmann, B., Forde, M., Linne, H., Lonitz, K., and Prospero, J. M.: The Barbados Cloud Observatory: Anchoring Investigations of Clouds and Circulation on the Edge of the ITCZ, Bulletin of the American Meteorological Society, 97, 787–801, https://doi.org/10.1175/BAMS-D-14-00247.1, 2016.

Stevens, B., Satoh, M., Auger, L., Biercamp, J., Bretherton, C. S., Chen, X., Düben, P., Judt, F., Khairoutdinov, M., Klocke, D., Kodama, C., Kornblueh, L., Lin, S.-J., Neumann, P., Putman, W. M., Röber, N., Shibuya, R., Vanniere, B., Vidale, P. L., Wedi, N., and Zhou, L.: DYAMOND: the DYnamics of the Atmospheric general circulation Modeled On Non-hydrostatic Domains, Progress in Earth and Planetary Science, https://doi.org/10, 2019.

Stevens, B., Bony, S., Brogniez, H., Hentgen, L., Hohenegger, C., Kiemle, C., L'Ecuyer, T. S., Naumann, A. K., Schulz, H., Siebesma, P. A., Vial, J., Winker, D. M., and Zuidema, P.: Sugar, gravel, fish and flowers: Mesoscale cloud patterns in the trade winds, Quarterly Journal of the Royal Meteorological Society, 146, 141–152, https://doi.org/10.1002/qj.3662, 2020.

Stevens, B., Bony, S., and Farrell, D. e. a.: EUREC^{4}A, Earth System Science Data Discussions, 2021, 1–78, https://doi.org/10.5194/essd-2021-18, 2021.

Tompkins, A. M.: Organization of Tropical Convection in Low Vertical Wind Shears: The Role of Cold Pools, J. Atmos. Sci., 58, 1650–1672, https://doi.org/10.1175/1520-0469(2001)058<0529:OOTCIL>2.0.CO;2, 2001.

Torri, G. and Kuang, Z.: Rain evaporation and moist patches in tropical boundary layers, Geophys. Res. Lett., 43, 9895–9902, 2016.

Touzè-Peiffer, L., Vogel, R., and Rochetin, N.: Detecting cold pools from soundings during EUREC4A, https://arxiv.org/abs/2104.09146, 2021.

Vial, J., Dufresne, J. L., and Bony, S.: On the interpretation of inter-model spread in CMIP5 climate sensitivity estimates, Clim. Dyn., pp. 3339–3362, https://doi.org/10.1007/s00382-013-1725-9, 2013.

https://doi.org/10.5194/acp-2021-420
Preprint. Discussion started: 1 June 2021
© Author(s) 2021. CC BY 4.0 License.

Atmospheric Chemistry and Physics Discussions

Vial, J., Vogel, R., Bony, S., Stevens, B., Winker, D. M., Cai, X., Hohenegger, C., Naumann, A. K., and Brogniez, H.: A New Look at the Daily Cycle of Trade Wind Cumuli, Journal of Advances in Modeling Earth Systems, 11, 3148–3166, https://doi.org/10.1029/2019MS001746, 2019.

Vial, J., Vogel, R., and Schulz, H.: On the daily cycle of mesoscale cloud organization in the winter trades, accepted for *QJRMS*, 2021.

Vogel, R.: The influence of precipitation and convective organization on the structure of the trades (Doctoral dissertation, Universität Hamburg), Berichte zur Erdsystemforschung, https://doi.org/10.17617/2.2503092, 2017.

Young, G. S., Perugini, S. M., and Fairall, C. W.: Convective Wakes in the Equatorial Western Pacific during TOGA, Monthly Weather Review, 123, 110, https://doi.org/10.1175/1520-0493(1995)123<0110:CWITEW>2.0.CO;2, 1995.

Zuidema, P., Li, Z., Hill, R. J., Bariteau, L., Rilling, B., Fairall, C., Brewer, W. A., Albrecht, B., and Hare, J.: On Trade Wind Cumulus Cold Pools, J. Atmos. Sci., 69, 258–280, https://doi.org/10.1175/JAS-D-11-0143.1, 2012.

Zuidema, P., Torri, G., Muller, C., and Chandra, A.: A Survey of Precipitation-Induced Atmospheric Cold Pools over Oceans and Their Interactions with the Larger-Scale Environment, Surveys in Geophysics, https://doi.org/10.1007/s10712-017-9447-x, 2017.

A climatology of trade-wind cumulus cold pools and their link to mesoscale cloud organization

Raphaela Vogel[1], Heike Konow[2], Hauke Schulz[3], and Paquita Zuidema[4]

[1]LMD/IPSL, Sorbonne Université, CNRS, Paris, France
[2]Meteorological Institute, Universität Hamburg, Hamburg, Germany
[3]Max Planck Institute for Meteorology, Hamburg, Germany
[4]Rosenstiel School of Marine and Atmospheric Science, University of Miami, Miami, FL, USA

Correspondence: Raphaela Vogel (raphaela.vogel@lmd.ipsl.fr)

Abstract. We present a climatology of trade cumulus cold pools and their associated meteorological perturbations based on more than ten years of in-situ and remote sensing data from the Barbados Cloud Observatory. Cold pools are identified by abrupt drops in surface temperature, and the mesoscale organization pattern is classified by a neural network algorithm based on GOES-16 ABI infrared images. We find cold pools to be ubiquitous in the winter trades—they are present about 7.8% of the time and occur on 73% of days. Cold pools with stronger temperature drops (ΔT) are associated with deeper clouds, stronger precipitation, downdrafts and humidity drops, stronger wind gusts and updrafts at the onset of the front, and larger cloud cover compared to weaker cold pools. The downdraft strength together with the cold-pool front duration explains 50% of the variability in ΔT.

The mesoscale organization pattern has a strong influence on the occurrence frequency of cold pools. Fish has the largest cold-pool fraction (12.8% of time), followed by Flowers and Gravel (9.9% and 7.2%), and lastly Sugar (1.6%). Fish cold pools are also significantly stronger and longer-lasting compared to the other patterns, while Gravel cold pools are associated with significantly stronger updrafts and deeper cloud-top height maxima. The daily cycle of the occurrence frequency of Gravel, Flowers, and Fish can explain a large fraction of the daily cycle in the cold-pool occurrence, as well as the pronounced extension of the daily cycle of shallow convection into the early afternoon by cold pools. Overall, we find cold-pool periods to be 90% cloudier relative to the average winter trades. Also the wake of cold pools is characterized by above-average cloudiness, suggesting that mesoscale arcs enclosing broad clear-sky areas are an exception. A better understanding of how cold pools interact with and shape their environment could therefore be valuable to understand cloud cover variability in the trades.

Copyright statement. TEXT

1 Introduction

Satellite images in the trades usually show very beautiful and diverse cloud structures over the dark blue ocean. Recurrent features in these images are mesoscale arcs of cumuli that encircle either clear-sky areas or extensive stratiform cloud decks.

The mesoscale arcs result from spreading cold pools that have favourable conditions at their gust front for triggering new convection. Convective cold pools are generated by the evaporation of precipitation into unsaturated downdrafts, spreading out at the surface as a density current. Cold pools are not only important for the triggering of new and often deeper convection (Schlemmer and Hohenegger, 2014; Feng et al., 2015; Rowe and Houze Jr., 2015), but might also play a role in regulating cloud cover in this regime responsible for much of the uncertainty in climate sensitivity (Bony and Dufresne, 2005; Vial et al., 2013). Here we use ground-based in-situ and remote sensing data from the Barbados Cloud Observatory (BCO) to study the climatology of trade-wind cumulus cold pools and to investigate its link to the pattern of mesoscale cloud organization.

Many studies addressing oceanic cold pools have focused on deep convection (Zuidema et al., 2017). In the trades, detailed case studies for two weeks of the *Rain in Cumulus over the Ocean* (RICO) campaign have advanced our understanding of cold pools from shallow convection (Zuidema et al., 2012). They showed that the deepest clouds and strongest radar signals occurred in the moistest tercile of water vapour paths, and that precipitation-driven downdrafts can introduce additional gradients in the thermodynamic structure. More recently, analyses of data from the *Elucidating the Role of Clouds-Circulation Coupling in Climate* (EUREC^{4}A) field campaign (Bony et al., 2017; Stevens et al., 2021), which took place in January and February 2020 upstream Barbados, reveal that cold pools are frequent in the winter trades and can be well-detected from soundings due to their very shallow mixed layers (Touzè-Peiffer et al., 2021). What is missing is a long-term climatology of trade cumulus cold pools, along with a description of the changes in cloud properties and sub-cloud layer dynamics associated with the cold-pool passages. Such a climatology is particularly pertinent given the need for a reference dataset for comparison against increasingly-available high-resolution simulations (Stevens et al., 2019; Rochetin et al., 2021).

Renewed interest in trade cumulus cold pools is also motivated by recent advances in characterizing patterns of mesoscale cloud organization. Stevens et al. (2020) classified 900 satellite images in the North Atlantic trades and identified four prominent patterns of mesoscale cloud organization—Sugar, Gravel, Flowers and Fish. The horizontal structure of the latter three patterns is intrinsically linked to the occurrence of mesoscale arcs and hence cold pools. The four patterns differ not only in their horizontal structure, but also in cloud cover, cloud depth and precipitation (Bony et al., 2020; Schulz et al., 2021; Vial et al., 2021). These differences likely also manifest in different cold-pool characteristics. Furthermore, cold pools might play different roles in creating and maintaining these patterns. For the pattern Fish with its very large-scale fish-bone structures that are tightly linked to extratropical dry intrusions (Aemisegger et al., 2021; Schulz et al., 2021), cold pools are likely to give the cloudy part its skeletal structure, but the overall system is forced by the large-scale into its linear alignment. Contrastingly, for the Gravel pattern, the large-scale influence may be less important and also more homogeneous, such that the cold pools likely play an important role in creating and maintaining this pattern. Before we can understand the different roles that cold pools play in these patterns, we need to understand whether and how cold-pool characteristics differ among them.

This paper presents the first long-term climatology of trade-wind cumulus cold pools and addresses the following research questions:

1. How frequent are cold pools in the trade cumulus regime, and with ~~which~~ changes in the surface meteorology, cloudiness and vertical velocity are they associated?

2. How do cold-pool characteristics covary with the pattern of mesoscale organization?

We use more than ten years of surface meteorology and ground-based remote sensing data from the BCO (Stevens et al., 2016). Clouds, their precipitation and therefore likely also cold pools at the BCO were shown to be representative across the trades (Medeiros and Nuijens, 2016). Cold pools are identified by abrupt drops in surface temperature, and the pattern of mesoscale organization is classified by a neural network algorithm based on infrared satellite images (Schulz et al., 2021).

The next section presents the data sources and explains the cold-pool detection algorithm and the selection criteria. In Section 3, we present the cold-pool climatology and analyse the temporal structure of the cold-pool passages and its associated changes in meteorology and cloudiness. Section 4 discusses differences between the cold-pool properties of the different mesoscale organization patterns. Conclusions are presented in Section 5.

2 Data and Methods

2.1 BCO data

We use in-situ and ground-based remote sensing data from the BCO (Stevens et al., 2016), which is operated by the Max Planck Institute for Meteorology together with the Caribbean Institute for Meteorology and Hydrology since April 2010. The BCO is located atop a 17 m cliff on an eastward promontory of Barbados called Deebles Point (13.16°N, 59.43°W), and samples nearly undisturbed Atlantic trade-wind conditions. We use surface meteorology and micro-rain radar (MRR) data from January 2011, cloud radar data from January 2012, and Doppler lidar data from March 2016 until March 2021. All data is aggregated into 1-min averages. The instruments used and meteorological variables derived are explained in the following. More details about the BCO and its instrumentation can be found in Nuijens et al. (2014) and Stevens et al. (2016).

Surface meteorology

A Vaisala WXT520 sensor mounted on a 5 m mast measures temperature, relative humidity, barometric pressure, wind speed and wind direction. We discard temperature measurements exceeding 35°C and pressure measurements lower than 980 hPa, as they are outside the expected range of variability at the BCO.

Micro-rain radar (MRR)

The MRR is a vertically-pointing frequency-modulated continuous-wave radar operating at 24 GHz (K band). The MRR has a sampling frequency of 10 s (here averaged to 1 min) and a range gate of 30 m up to a height of 3 km. Rain rates lower than 0.03 $\mathrm{mm\,h^{-1}}$ are below the noise level and set to zero. We derive the mean rain rate (RR) and the rain intensity (R_{int}; i.e. the rain rate during periods of rain) in a given period from data at 325 m above ground (the lowest level with reliable data). The MRR is also used to compute the rain frequency (R_{freq}), which is set to 1 when a $RR > 0.05\,\mathrm{mm\,h^{-1}}$ is measured in at least five range gates in the lowest 3 km (following Nuijens et al., 2014). A few instances with unrealistically large RR exceeding 200 $\mathrm{mm\,h^{-1}}$ are set to NA.

Cloud radar

Vertical profiles of hydrometeors (i.e. cloud and rain droplets) at approx. 30 m vertical resolution are derived from two 35.5 GHz (Ka-Band) Doppler cloud radars. Radar returns with an equivalent radar reflectivity lower than -50 dBZ are removed to eliminate signal from sea salt aerosol (Klingebiel et al., 2019). To identify individual 2D cloud entities, a cloud segmentation algorithm is applied (Konow, 2020). Radar reflectivity is converted to a binary mask and morphological closing is applied. The resulting mask is used to segment cloud entities with connected components analysis with 8-connectivity. A minimum cloud size of four pixels is applied, everything smaller than four pixels is discarded as clutter. For the resulting cloud entities, the ~~overall~~ cloud-base height (cbh_{ID}), ~~overall~~ cloud-top height ~~and the~~ cloud length ~~(i.e.~~ the duration times the wind extrapolated from the surface to cloud base ~~assuming a power law) are determined~~. To focus on clouds connected to the sub-cloud and trade-wind layer, cloud entities with a cbh_{ID}>4 km are excluded.

From the remaining clouds, we derive timeseries of the hydrometeor fraction, the ~~lowest~~ cloud-base height (CBH) and the highest cloud-top height (CTH) for every radar profile. The cloud cover is further split up into contributions from precipitating cloud segments if $CBH \leq 300$ m (CC_{prcp}), from cloudiness near the lifting-condensation level (CC_{lcl}; 300 m $< CBH \leq$ 1 km), and from cloudiness aloft (CC_{aloft}; 1 km $< CBH \leq 4$ km). The ~~latter~~ two categories were also used in many previous studies (e.g Nuijens et al., 2014; Vial et al., 2019). A given radar profile can only count to one of the three categories, such that e.g. a 2 km deep cloud with a CBH<300 m will only be counted in the CC_{prcp} category. Note that the above classification into the different CBH categories does not account for the information of the cloud entity and all radar profiles are classified independently. A similar analysis accounting for the cloud entity by classifying cloud cover contributions of different cloud types by their cbh_{ID} is shown in Appendix A.

From the cloud radar we also derive a deep-cloud mask, which is set to 1 if a radar signal between 4.5–8 km is detected. With this deep-cloud mask, periods of active deep convection reaching above the melting level can be omitted, while periods with only cirrus-clouds are retained.

Doppler lidar

The vertical velocity in the sub-cloud layer is measured by two Halo Photonics Streamline Pro Doppler wind lidar systems at 30 m vertical resolution. The Doppler lidars measure vertical velocities of up to $\pm 20\,\mathrm{m\,s^{-1}}$ with a 1500 nm laser in altitudes from about 50 m to 1 km, depending on the atmospheric conditions and the aerosol loading. The precision is $<20\,\mathrm{cm\,s^{-1}}$ for a signal-to-noise ratio (SNR) of -17 dB. Measurements with a SNR smaller than -18.3 dB are discarded. Data from the first system that was operated in vertically-pointing mode with a temporal resolution of 1.3 s is used from March 2016 to October 2019. A second system is operated in horizontally-scanning mode since February 2019 and has a temporal resolution of 3 s, with 2 out of 7 profiles measured in vertically-pointing mode. Vertical data from this second lidar is used from November 2019 to March 2021.

We derive both the average vertical velocity in the sub-cloud layer (SCL) as the mean over 15 range gates from 75-495 m (w_{SCL}), and the vertical velocity near the sub-cloud layer top at 450 m as the mean over the four range gates from 405-495 m (w_{450}).

2.2 Machine learning classification of mesoscale cloud organization patterns

The pattern of mesoscale cloud organization at BCO for the period January 2018 to March 2021 is classified by a neural network algorithm applied to infrared satellite images from the Geostationary Operational Environmental Satellite 16 (GOES-16). We use 30-minute brightness temperature retrievals from the 10.35μm-channel at a spatial resolution of 2 km from the Advanced Baseline Imager (ABI) Level 1b data product (GOES-R Calibration Working Group and GOES-R Series Program, 2017), over a large domain including Barbados (45°W-66°W, 9.3°N-23.3°N).

The neural network based on the Retinanet algorithm (Lin et al., 2017) has been initially trained on and applied to visible images in Rasp et al. (2020), and later retrained and applied to infrared images by Schulz et al. (2021). The use of infrared images also allows study of the diurnal cycle of the mesoscale organization (Vial et al., 2021). The classifications of the neural network are rectangles of various sizes that belong to either the Sugar, Gravel, Flowers or Fish pattern. We select every classified rectangle that overlaps with the BCO location. Periods without a classification are labelled as 'No'. ~~For conditioning on cold pools, the 30-min data is downscaled to 1-min by using a given pattern for the 15 min before to after the classification time~~. If a given pattern is present for more than 75% of the duration of a cold pool, the ~~pattern is attributed to this~~ cold pool.

At any given time, multiple rectangles of different sizes of the same and of different patterns can occur. Multiple rectangles of the same pattern are combined and counted only once, while multiple rectangles of different patterns are counted separately. This leads to ~~timesteps~~ being classified e.g. as both Gravel and Flowers. Excluding situations with multiple patterns only marginally influences the results, but reduces the sample size considerably (as previously noted in Vial et al., 2021). Ambiguities in the classification can be physical—for example due to regime transitions or similarities between patterns—or related to ambiguities introduced to the neural network by disagreement in the human classifications. The occurrence of multiple patterns can be reduced if a stricter threshold is used for the agreement score representing the confidence of the neural network prediction (here set to 0.4 as in Schulz et al., 2021; Vial et al., 2021), but this again reduces the sample size.

2.3 Cold-pool detection algorithm

We detect cold pools by identifying abrupt drops in the surface temperature timeseries following Vogel (2017). We first filter the 1-min averaged temperature timeseries with an 11-minute running average. We then classify all temperature drops $\delta T = T_{\mathrm{fil}}(t) - T_{\mathrm{fil}}(t-1) < -0.05$ K (per minute) in the filtered timeseries as a cold-pool candidate (see Figure 1 for an illustration). For every candidate cold pool, we detect the time of the cold-pool front onset ($t_{\max}$), the time of the minimum temperature ($t_{\min}$), and the end of the cold pool (t_{end}) as follows:

1. $t_{\max}$: the onset of the cold-pool front $t_{\max}$ is defined as the last instance of $\delta T > 0$ K within 20 min before the initial abrupt temperature drop. If the temperature is falling continuously in this period, $t_{\max}$ is chosen as the time of the maximum temperature (that is, 20 min before the abrupt temperature drop). We refer to the smoothed temperature at $t_{\max}$ as $T_{\max}$.

2. $t_{\min}$: the time of the minimum filtered temperature $T_{\min}$ marks the end of the cold-pool front and is identified as the minimum of contiguous temperature minima. Subsequent candidate cold pools with $\delta T < -0.05\,\mathrm{K}$ occurring within 20 min of the previous minimum are combined if the temperature does not rise by more than 0.5 K above the previous minimum in between.

3. t_{end}: the end of a cold pool is defined either as the minimum of (a) the time when the filtered temperature first exceeds its minimum by $\Delta T/e$, where $\Delta T = T_{\max} - T_{\min}$, or (b) the onset of the next cold pool. If using condition (a) or (b) leads to any temperature between $t_{\min}$ and t_{end} to be smaller than $T_{\min} - 0.1\,\mathrm{K}$, then t_{end} is defined as (c) the time when the filtered temperature first decreases again after increasing for some time following $t_{\min}$. Cold pools with t_{end} defined by (a) are referred to as recovered.

The period between $t_{\max}$ and $t_{\min}$ is referred to as the cold-pool front, and the period between $t_{\min}$ and t_{end} as the cold-pool wake.

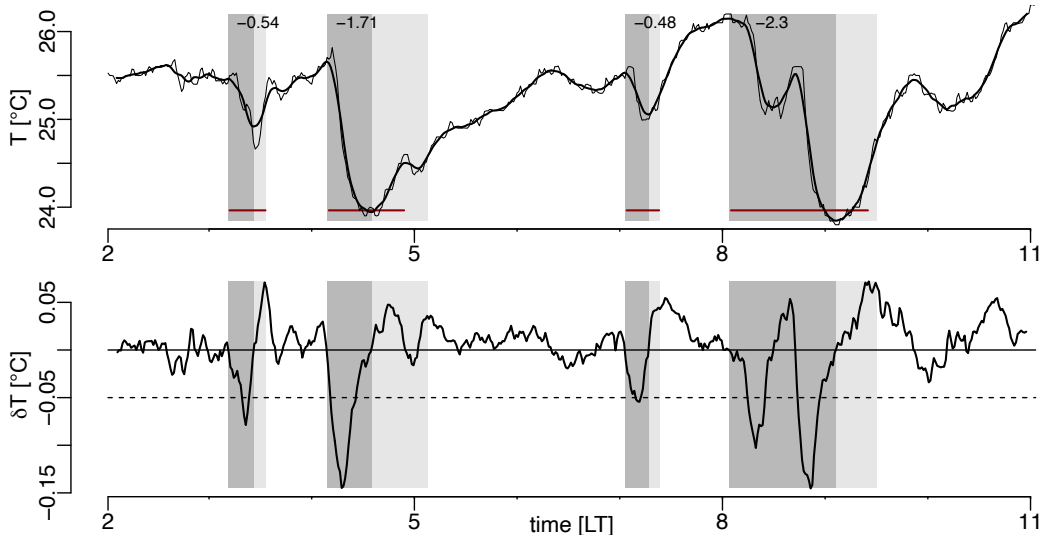

Figure 1. Illustration of the cold-pool detection algorithm. (top) 11-min filtered T_{fil} (thick line) and 1-min raw surface temperature (thin line), and (bottom) filtered temperature difference δT, along with the threshold of -0.05 K used (dashed). The detected cold-pool fronts and wakes are indicated in dark grey ($t_{\max}$ to $t_{\min}$) and light grey ($t_{\min}$ to t_{end}), with the corresponding ΔT indicated at the top. The dark red lines in the top panel show the analysis periods used for computing the diagnostics (see Section 2.5).

Our cold-pool detection algorithm is similar to the one used by de Szoeke et al. (2017), but with the important modification that we only identify cold pools for situations with abrupt temperature drops. With our algorithm we thus both filter out turbulent fluctuations and advective or diurnal patterns of temperature variability. The threshold of $\delta T < -0.05\,\mathrm{K}$ is subjectively chosen based on visual impression and represents distinct variations in temperature. For an 11-min averaging window, a δT of $-0.05\,\mathrm{K}$ corresponds to about 2% of the data. Figure 2 shows example cold pools for all patterns and illustrates the workings of the algorithm. In next subsection we briefly discuss the strengths and weaknesses of the algorithm based on these examples.

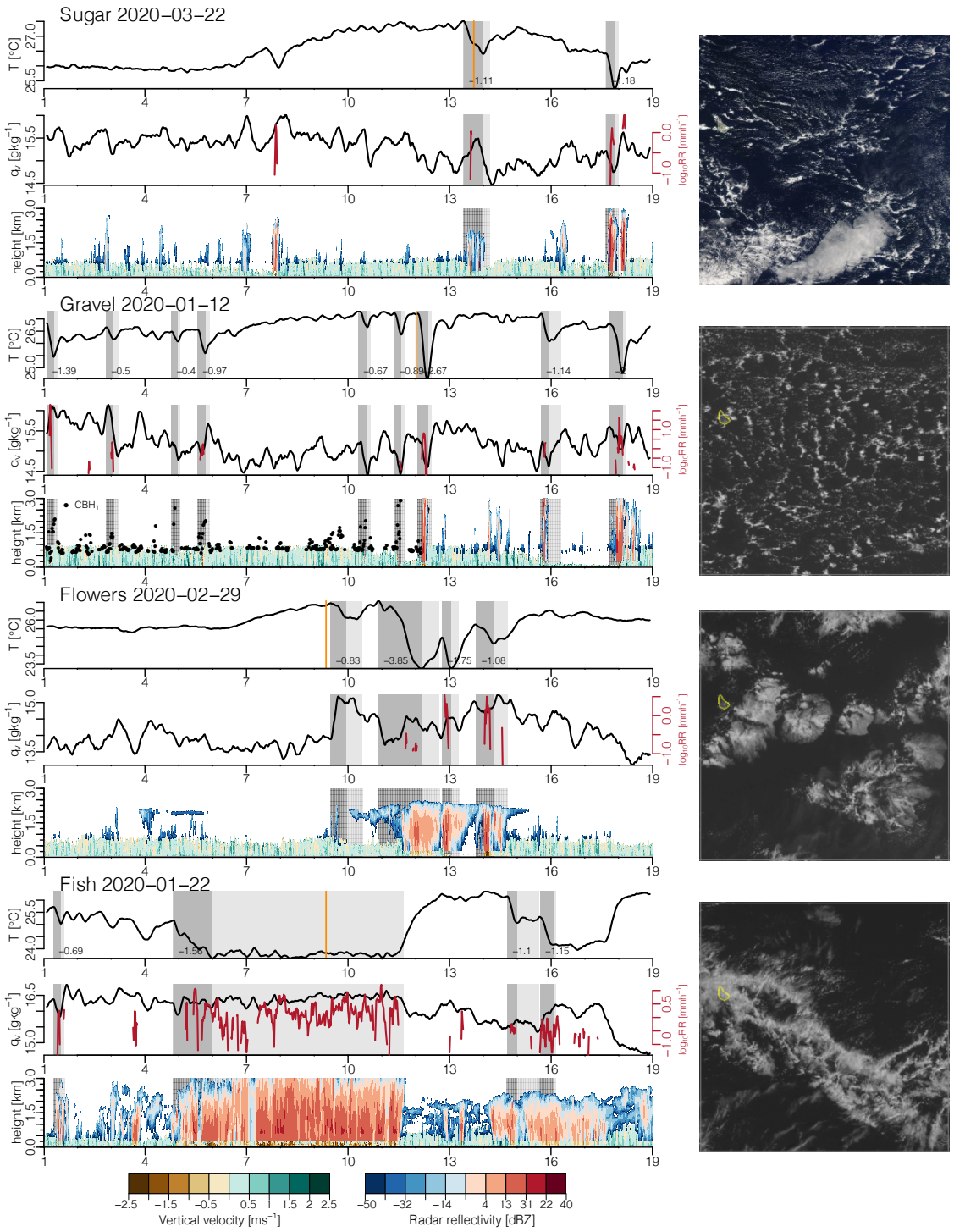

Figure 2. BCO time series and satellite images for 18 h of four cold-pool days representative of the four patterns. Shown are timeseries of filtered surface temperature and specific humidity, MRR RR, and time-height plots of Doppler lidar vertical velocity and radar reflectivity. On the Gravel day the radar did not work prior to 12 LT [illegible] the lowest CBH from the ceilometer is shown instead. The x-axis shows local time and the detected cold-pool fronts and wakes are indicated in grey and light grey, with ΔT indicated at the bottom. Visible satellite images from 10-15°N and 60-55°W from MODIS Aqua (Sugar day) and GOES-16 ABI (other days), with the respective recording times indicated by the orange lines in the temperature panels. The BCO is located near the easternmost tip of Barbados (outlined in yellow).

2.4 Example cases

Timeseries of example cold-pool days along with corresponding satellite images are shown for every pattern in Figure 2. The example cases highlight how well the detection algorithm works in these diverse situations. Abrupt strong temperature drops are reliably detected, successive fronts sensibly combined into one single cold pool, and even the 6 h long cold pool with frontal character on the Fish day is correctly identified.

The example cases also indicate some challenges of the cold-pool identification. Although they look like cold pools, some temperature drops on the Gravel and Sugar day are not identified as cold pools because they are either not abrupt enough ($\delta T > -0.05$ K) or not strong enough ($\Delta T > -0.4$ K). The difficulty in defining the end of the cold-pool wake is illustrated in the Fish case: the cold pool starting shortly before 16 LT lasts until well after 18 LT, but the temperature drop near 17 LT causes a premature end of the cold pool, as such a temperature drop could also be caused by the daily cycle in temperature. The cold-pool end definition could be improved by an additional rain or downdraft requirement, to more robustly distinguish between cold-pool activity and other processes. Because most analyses and diagnostics computed in this study focus entirely on the cold-pool front (see next section), not fully representing the wake of rare long-lasting cold pools is a minor issue and only influences the overall cold-pool fraction and the duration statistics.

As mentioned in Section 2.2, the organization pattern definition is not unambiguous and also among the example days shown in Figure 2 some cold pools pertain to multiple patterns. For the Flowers case, the 2 h at the beginning and end of the period shown are also classified respectively as Gravel and Fish. In the Sugar case, only the period between 9-16 LT is exclusively classified as Sugar, while the periods before and after are also partly classified as Gravel. Most surprisingly, the textbook Gravel day is also entirely classified as Flowers, and also setting a stricter agreement score of 0.5 leaves half of the day co-classified as Flowers. This indicates that distinguishing Gravel from Flowers can be particularly challenging (as also shown in Vial et al., 2021). The Fish day is very confidently classified and no other pattern is detected for the entire day.

2.5 Selection criteria and diagnostics

For the subsequent analyses, we apply a number of selection criteria to make the comparison of cold pools more robust. Namely, we only consider cold pools with $\Delta T < -0.4$ K and less than two missing values in the filtered temperature timeseries during the entire cold-pool duration (set *all* with 9234 cold pools). For the analyses of the cold-pool properties we further apply a criterion of no non-recovered cold pool in the hour prior to the cold-pool onset (set *noprev* with 8772 cold pools), which selects cold pools moving into an initially undisturbed atmosphere that is not modified by previous convection. For most of the analyses we also focus on the dry winter regime from December-April (set *noprevWI* with 3889 cold pools), which is characterized by steady easterlies, subsiding large-scale motion in the free troposphere and the predominance of shallow trade-wind convection (Brueck et al., 2015).

As shown in the brackets, all these selection criteria reduce the cold-pool sample size considerably. They represent a trade-off between assuring a robust and unbiased sample to address our research questions, while not being unnecessarily strict and removing too many cold pools. The selection criteria are thus somewhat subjective and also differ among studies. For example,

Chandra et al. (2018) used the criterion of no rain in the hour prior to the cold-pool onset to select cold pools unmodified by previous convection, whereas we achieve the same goal with the criterion of no non-recovered cold pool in the prior hour, which excludes about 2500 less cold pools in our case. Instead of focusing on the winter regime, we could have also set a criterion based on the cloud-top height to focus on trade cumulus cold pools. However, as this would restrict the analysis to periods when the radar is running, and—as we are relying on single-site measurements—the parent convection might not move over the BCO in its entirety, we would likely exclude too many cold pools with a CTH criterion, without even being sure that periods of deep convection are really excluded. Despite the rather strict criteria applied here, the long timeseries leads to a much larger number of cold pools analysed than in previous studies.

Another potential sampling issue regarding the single-site measurements is that it is not clear at which stage of its lifecycle we sample the cold pool, and where we sample it with respect to its center. Assuming ~~isotropic~~ wind variations around the cold-pool center, which in case of little wind shear is a good approximation (Touzè-Peiffer et al. 2021), the change in wind direction from the mean direction prior to the cold-pool onset could give a hint as to the location relative to the cold-pool center. However, due to our large sample size potential biases are likely to be small.

If not mentioned differently, the cold-pool diagnostics are computed either as the minimum difference (ΔX_{min}) or maximum difference (ΔX_{max}) of a variable X between its value at t_{max} and the values between $t_{\mathrm{max}}+1$ and min(t_{end}, $t_{\mathrm{min}}+20$). Similarly, X_{mean} or X_{max} are the mean or maximum of variable X over the same analysis period (indicated in dark red in Figure 1). For the Doppler lidar vertical velocities, we diagnose w_{maxSCL} (w_{max450}) as the maximum w_{SCL} (w_{450}) in the first half of the front (including the last 10 min before t_{max}), and w_{minSCL} as the minimum w_{SCL} in the second half of the front (including the first 10 min after t_{min}). Unless otherwise stated, the surface meteorology diagnostics are computed from the 11-min filtered timeseries.

Along with most diagnostics and composites we show the standard error (SE), which measures how well the median or mean of a given sample can be estimated. The SE of the median is computed as $IQR/\sqrt{n}$, where IQR represents the inter-quartile range and n the sample size, and the SE of the mean as $\sigma/\sqrt{n}$, where σ is the standard deviation. As not all instruments were running all the time, some diagnostics are only available for a subset of the cold pools and the sample size is adjusted accordingly when computing the SE.

3 Cold-pool climatology

In this section we present the climatology of trade cumulus cold pools detected at BCO for the winter seasons of the years 2011-2021. The first subsection presents general statistics, followed by a discussion of the composite temporal structure of the cold pools in Section 3.2. The daily cycle of cold-pool statistics is shown in Section 3.3. While our focus lies on the winter regime, Appendix B also briefly discusses the seasonal cycle of the cold-pool statistics.

3.1 General statistics

In total we detect 3889 cold pools that meet the criteria of $\Delta T < -0.4\,\mathrm{K}$ and less than two missing values in T_{fil} in the winter seasons considered. We find that cold pools are very frequent at BCO and on 73% of days at least one cold pool is detected. The BCO is on average affected by cold pools during 7.8% of the day (i.e. 112 min) and by a cold-pool front during 4.4% of the day, with the medians being about one-third smaller than the means mentioned The mean cold-pool fraction of 8.6% for January and February 2011-2021 is also very close to the 7% found by Touzè-Peiffer et al. (2021) during the EUREC^{4}A campaign in January and February 2020, despite their very different method defining cold pools in atmospheric soundings based on a mixed-layer depth criterion.

Table 1. Table showing median$\pm IQR$ of various cold-pool properties for the *noprevWI* set of cold pools, as well as the 25% strongest ($\Delta T < -1.39\,\mathrm{K}$) and weakest ($\Delta T > -0.61\,\mathrm{K}$) cold pools of this set. How the diagnostics are computed is explained in Section 2.5 and in the text.

	noprevWI	strong	weak
#	3889	972	972
ΔT [K]	-0.89±0.78	-1.82±0.67	-0.5±0.1
$\Delta T_{\mathrm{unfil}}$ [K]	-1.2±0.8	-2.16±0.66	-0.79±0.17
Δq_{min} [gkg^{-1}]	-0.43±0.65	-0.55±0.81	-0.36±0.54
Δq_{max} [gkg^{-1}]	0.2±0.41	0.29±0.51	0.12±0.3
$\Delta \theta_{\mathrm{e,min}}$ [K]	-2.05±2.08	-3.3±2.25	-1.35±1.35
$\Delta \theta_{\mathrm{v,min}}$ [K]	-0.96±0.81	-1.92±0.7	-0.55±0.14
ΔU_{max} [ms^{-1}]	1.14±1.55	2±1.97	0.7±0.99
R_{int} [mmh^{-1}]	0.9±1.76	1.45±2.42	0.41±0.95
RR_{mean} [mmh^{-1}]	0.05±0.38	0.39±1.06	0±0.04
CTH_{max} [km]	3.04±1.11	3.56±1.2	2.66±0.96
CTH_{mean} [km]	2.32±0.88	2.74±0.81	2.03±0.89
w_{minSCL} [ms^{-1}]	-0.55±1.56	-1.89±2.42	-0.27±0.51
w_{maxSCL} [ms^{-1}]	0.91±0.62	1.1±0.7	0.78±0.54
w_{max450} [ms^{-1}]	0.98±0.81	1.27±0.99	0.79±0.66
length [km]	13.34±9.49	18.65±10.94	10.01±6.03
$\Delta t_{\mathrm{nextcp}}$ [min]	117±426	85±245	158±725
dur [min]	33±22	47±29	25±12
front dur [min]	19±12	29±19	15±4

Table 1 presents statistics of the most important cold-pool properties for the set of winter cold pools with no non-recovered cold pool in the prior hour (*noprevWI*). It shows that 50% of the cold pools have a temperature drop exceeding 0.9 K across

the front (the unfiltered temperature drop is 0.3 K stronger), a $\Delta q_{\max}$ exceeding 0.2 g kg^{-1} and a $\Delta q_{\min}$ below -0.43 g kg^{-1}, decreases in θ_e and θ_v exceeding -2.1 K and -0.96 K, respectively, and a $\Delta U_{\max}$ larger than 1.14 m s^{-1}. The median rain intensity measured by the MRR is 0.9 mm h^{-1}. Furthermore, 50% of the cold pools are associated with a maximum cloud-top height exceeding 3 km, and w_{maxSCL} and w_{minSCL} of 0.9 m s^{-1} and -0.55 m s^{-1} near the onset and end of the front, respectively. The average cold-pool duration is 33 min, of which a bit more than half of the time pertains to the front. Multiplying the duration with the surface wind speed yields a median cold-pool length larger than 13.3 km.

The IQR shows that all these medians are associated with substantial variability, especially for the humidity and rain variables. However, focusing on the winter regime generally reduces the IQR of the diagnostics compared to all seasons (not shown), suggesting that this criterion indeed results in a more homogeneous cold-pool sample representative of the trade-cumulus regime. The median duration of 33 min and length of about 13.3 km of the cold pools may seem small compared to satellite imagery, in which mesoscale cold-pool arcs can easily span 100 km. Also the largest 2% of cold pools are hardly larger than 40 km. The smaller cold-pool sizes found here are likely due to the algorithm sampling mostly the edge of the cold pools, and due to the challenges of defining the cold-pool end purely based on the surface temperature timeseries (see discussion in Section 2.4).

Table 1 also compares the median$\pm IQR$ of the 25% strongest and weakest cold pools in terms of ΔT. The strongest cold pools last longer, follow each other more quickly (lower Δt_{nextcp}), and are associated with deeper clouds, more rain, stronger downdrafts, humidity drops and wind gusts, and larger positive vertical velocities at the beginning of the front compared to weaker cold pools. Similar but slightly smaller differences between stronger and weaker cold pools are found when comparing cold pools associated with the 25% strongest versus weakest downdrafts or the 25% deepest versus shallowest $CTH_{\max}$ (not shown). The downdraft strength w_{minSCL} is the diagnostic that correlates best with ΔT (R^2=0.23), and together with the front duration it explains a lot of the variability in ΔT for the *noprevWI* set (multiple R^2=0.49). The 25 and 75% quartiles of w_{minSCL} also distinguish the rain diagnostics best.

That $CTH_{\max}$ also distinguishes the cold-pool properties very well indicates that the parent convection triggering the cold pool is sampled well by the single-point measurements. The CTH usually scales with the precipitation amount for trade cumuli (Byers and Hall, 1955; Kubar et al., 2009; Nuijens et al., 2009), so other factors like the environmental humidity do not seem to influence rain evaporation and downdraft strength much further. We also compared the properties of the 25% driest and moistest cold pools in terms of $\Delta q_{\min}$ (not shown), which does not strongly distinguish other cold-pool properties, not even the RR that was shown to be particularly related to $\Delta q_{\min}$ in the literature (Barnes and Garstang, 1982). The specific humidity signal is generally also very variable and the response to the cold-pool onset hard to define in one diagnostic, as will be shown next.

3.2 Composite temporal structure

Figure 3 shows the composite mean temporal structure of the perturbations associated with the cold-pool passages. To facilitate the comparison of different cold pools, we use a normalized time coordinate in the cold-pool front with values mapped onto

20 points (the median front duration), similar to previous studies (Young et al., 1995; de Szoeke et al., 2017; Zuidema et al., 2017).

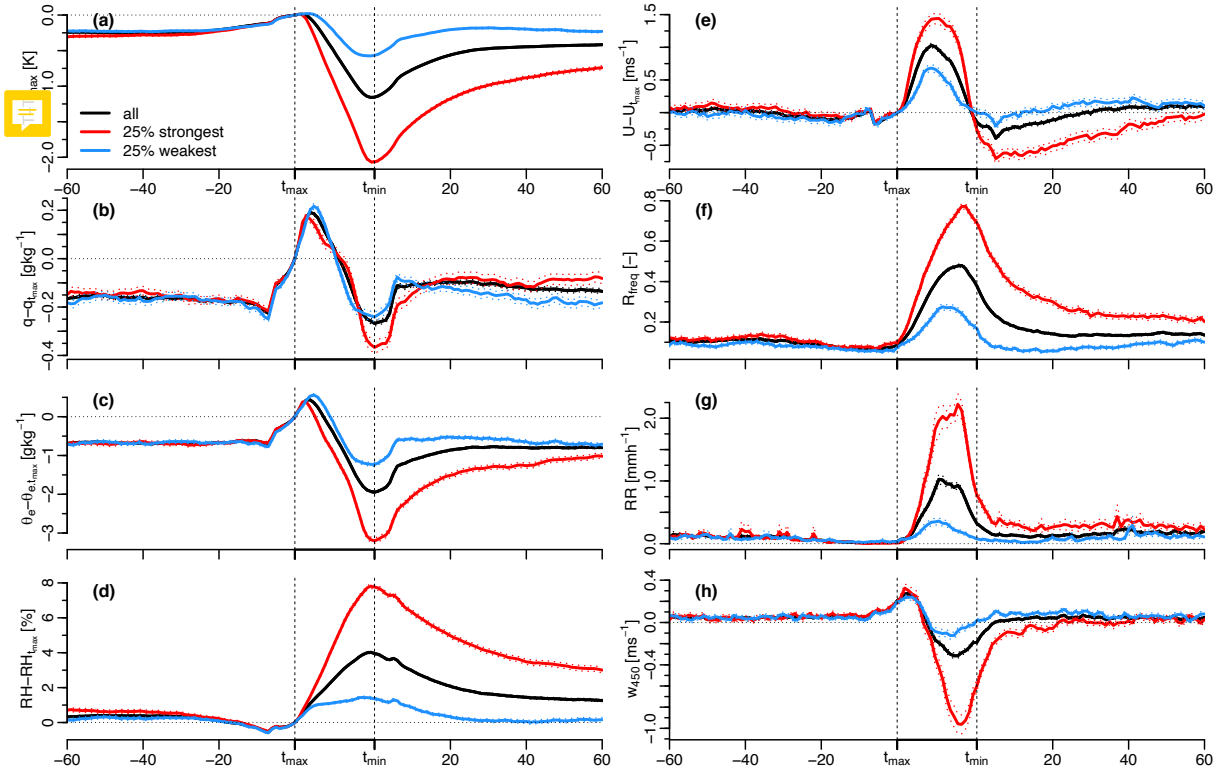

Figure 3. Composite mean temporal structure of anomalies relative to the cold-pool onset ($t_{\max}$) for the surface properties (a) temperature, (b) specific humidity, (c) equivalent potential temperature, (d) relative humidity, and (e) wind speed, as well as absolute values of (f) the MRR rain frequency and (g) rain rate, and (h) the vertical velocity at 450 m height. The black line shows the mean structure of all cold pools matching the *noprevWI* criterion, and the red and blue lines show the mean for the 25% strongest and weakest cold pools, respectively. The dotted lines show the mean±1 SE. Vertical and horizontal reference lines are added to indicate $t_{\max}$, $t_{\min}$ and 0.

The temperature of the composite-mean cold pool, after increasing slightly before $t_{\max}$, decreases rapidly in the front and recovers by $\Delta T/e$ within 16 min after $t_{\min}$. The temperature remains about 0.5 K below T_{max} in the hour after the frontal passage. The temperature drop in the front of the 25% strongest cold pools is by definition stronger, but with a mean tendency of $-0.070\,\mathrm{K\,min^{-1}}$ also more than twice as abrupt compared to the weakest cold pools. The strongest cold pools also take longer to recover than the weakest.

The temporal structure of the specific humidity response is intriguing. The composite-mean humidity starts to increase already 8 min before $t_{\max}$ and increases by about $0.2\,\mathrm{g\,kg^{-1}}$ until $t_{\max}$. In the first quarter of the front, the humidity increases by another $0.2\,\mathrm{g\,kg^{-1}}$, before it drops to its minimum of $-0.25\,\mathrm{g\,kg^{-1}}$ at $t_{\min}$, which is hardly lower than the pre-front value. The humidity recovers much more quickly than the temperature and remains slightly elevated compared to its pre-front value

in the hour after. The fast humidity recovery might be due to the trapping of surface moisture fluxes in the shallow mixed layer typically associated with cold pools (Touzè-Peiffer et al., 2021). Another reason might be continued evaporation of precipitation, which would cool and moisten the air in the cold-pool wake and thus speed up the humidity recovery but slow down the temperature recovery.

The specific humidity response of the strongest cold pools only differs significantly from the weakest cold pools at $t_{\min}$, with the humidity drop at $t_{\min}$ being about $-0.4\,\mathrm{g\,kg^{-1}}$ and thus about twice stronger than the drop for the weakest cold pools. If the entire set of cold pools including the summer season with deeper convection is used, the strongest cold pools have a significantly weaker positive humidity anomaly at the beginning of the front, and a significantly faster and stronger humidity reduction at $t_{\min}$ compared to the weakest cold pools (see Figure B1c-d). As discussed by de Szoeke et al. (2017), the humidity increase just before $t_{\max}$ might be mostly due to the increasing saturation specific humidity associated with the increasing temperature before $t_{\max}$ (as seen by the relative humidity anomaly in panel d being slightly below zero), and as such likely also related to the way we identify $T_{\max}$.

The temporal structure of the equivalent potential temperature is similar to the humidity structure, but with a stronger drop across the front, and a stronger difference between the weaker and stronger cold pools governed by the temperature drops. The relative humidity signal in the front is mostly governed by the temperature decrease, with RH being 8% larger at $t_{\min}$ for the strongest cold pools. The in-front wind speed increase has a maximum in the middle of the front. After the frontal passage, the wind speed decreases slightly below the pre-front level. The strengthening winds in the front and the slackening winds in the wake are again significantly more pronounced for the strongest cold pools, with a maximum of $1.5\,\mathrm{m\,s^{-1}}$ and a minimum smaller $-0.5\,\mathrm{m\,s^{-1}}$ in the front and wake compared to the value at $t_{\max}$. Figure 3f-g show the composite mean R_{freq} and RR measured by the MRR. Both rain variables increase rapidly after the onset of the cold pool, peak towards the middle or end of the front, and start to decrease shortly before $t_{\min}$. The strongest cold pools have much larger rain rates and rain frequencies during the entire front compared to the weakest cold pools, and the rain frequency of the strongest cold pools also remains strongly elevated until more than an hour after $t_{\min}$.

The last panel of Figure 3 shows the Doppler lidar vertical velocity averaged over four 30 m range gates with mean height of 450 m (w_{450}). The mean w_{450} peaks at the edge of the front with about $0.25\,\mathrm{m\,s^{-1}}$ and decreases rapidly to $-0.3\,\mathrm{m\,s^{-1}}$ near the end of the front, reflecting updrafts triggered at the cold-pool gust front and downdrafts driven by the evaporating precipitation inside the front, respectively. The strongest cold pools have significantly stronger downdrafts and also updrafts compared to the weakest cold pools (see also Table 1), the latter highlighting the potentially enhanced triggering of new convection by stronger cold pools. For the vertical velocity averaged over the entire sub-cloud layer (w_{SCL}), the picture is similar, but the peak w_{maxSCL} is slightly smaller for the strongest cold pools and more similar compared to the weaker cold pools (Table 1).

As already shown in Table 1, Figure 3 shows that the strongest cold pools are also the driest and the rainiest, and have the strongest wind and vertical velocity anomalies in the front. The relationships and timings discussed are mostly the same when considering all cold pools meeting the *noprev* criterion (i.e. also including summer periods), just with larger anomalies and the differences mentioned above for the humidity structure. The mean temporal structure for all variables—except for the specific humidity and partly for the wind speed—is also similar to previous observations of tropical deep convective cold pools during

the DYNAMO field campaign (de Szoeke et al., 2017; Chandra et al., 2018), just with slightly smaller anomalies at BCO due to the shallower convection. During DYNAMO, the increases in specific humidity at the beginning of the front are hardly present and the humidity minima near $t_{\min}$ are much more pronounced compared to BCO. The mean in-front wind speed increase is about $2\,\mathrm{m\,s^{-1}}$ and the wind speed also remains elevated in the wake of the DYNAMO cold pools (de Szoeke et al., 2017; Chandra et al., 2018), whereas at BCO it decreases below the value at $t_{\max}$ in the wake. What might strengthen cold pools in the trades despite the shallower parent convection is the drier cloud layer and free troposphere compared to the deep convective regions, which facilitates evaporation of precipitation and can strengthen downdrafts (Chandra et al., 2018).

The initial increase in humidity at the edge of the front at BCO might be explained by enhanced surface fluxes due to the strengthening winds (Langhans and Romps, 2015; Torri and Kuang, 2016), or by an accumulation of moisture from evaporation of precipitation of the parent convection, which was pushed to the edge of the front (Tompkins, 2001). Analyses of the various isotope measurements made during the EUREC^{4}A field campaign (Stevens et al., 2021) might help elucidate the origin of these moisture rings. This could also help understand why cloud-resolving models seem to have difficulties in representing the humidity structure in the cold-pool front correctly (Chandra et al., 2018).

The cloud radars at BCO also allow study of how the cloud properties change across the cold-pool passage (Figure 4). The mean cloud-top height (CTH) increases rapidly by $\sim 500\,\mathrm{m}$ after the cold-pool onset and peaks at the end of the front. CTH remains elevated by $\sim 300\,\mathrm{m}$ compared to the pre-front value in the following hour. The 25% strongest cold pools are associated with significantly deeper clouds throughout the entire period shown, especially so at the end of the front, when the CTH is on average higher than 3300 m. The cloud-base height (CBH) starts to decrease already slightly before $t_{\max}$ and reaches its minimum near the end of the front at $\sim 500\,\mathrm{m}$. This decrease is due to the more frequent precipitation with very low echo-base heights, and is most pronounced for the strongest cold pools.

The total hydrometeor cover (CC) increases rapidly at the beginning of the cold-pool front, remains about 25% larger compared to the pre-front value inside the front, and then decreases slowly in the wake. The mean CC of the 25% strongest cold pools reaches nearly 100% at the end of the front and is significantly larger than the CC of the weakest cold pools during the entire period shown, especially so in the wake. Figure 4d-f show that the enhanced CC of the strongest cold pools in the prior hour is entirely due to cloud segments with CBH above 1 km (CC_{aloft}), whereas the enhanced CC in the front and wake of the strongest cold pools is mostly due to precipitating cloud segments with CBH below 300 m. The rapid increase in CC_{lcl} up to its peak at $t_{\max}$ strongly contributes to the CC increase at the edge of the front. This peak is also larger for the strongest cold pools, consistent with their larger w_{450} at $t_{\max}$. CC_{lcl} and CC_{aloft} are lower at the end of the front for the strongest cold pools, as the lowest CBH is mostly below 300 m and the cloud segments thus count to the CC_{prcp} category (note that a given time can only count to one of the three categories).

In Figure 4d-f the cloud cover is split into contributions from cloud segments with different CBH without accounting for the information of the cloud entity. Based on a similar analysis that accounts for the entity information (see Appendix A), we find that the peak in CC_{lcl} at $t_{\max}$ is mainly due to edges of precipitating clouds that have a $CBH > 300\,\mathrm{m}$. Assuming that this cloud population represents the clouds evident as mesoscale arcs in satellite imagery, this suggests that the cloudiness at the gust front is mostly characterized by well-developed precipitating clouds. The entity analysis also shows that more than

355 half of the CC_{aloft} in the cold-pool wake is part of large precipitating clouds, and not from detached stratiform layers. This is also suggested by the time-height plots of the composite-mean hydrometeor fraction shown in Figure 4g-i. These panels nicely summarize what was discussed in the previous paragraphs, and again highlight the differences between the 25% strongest and weakest cold pools in terms of the cloud respons

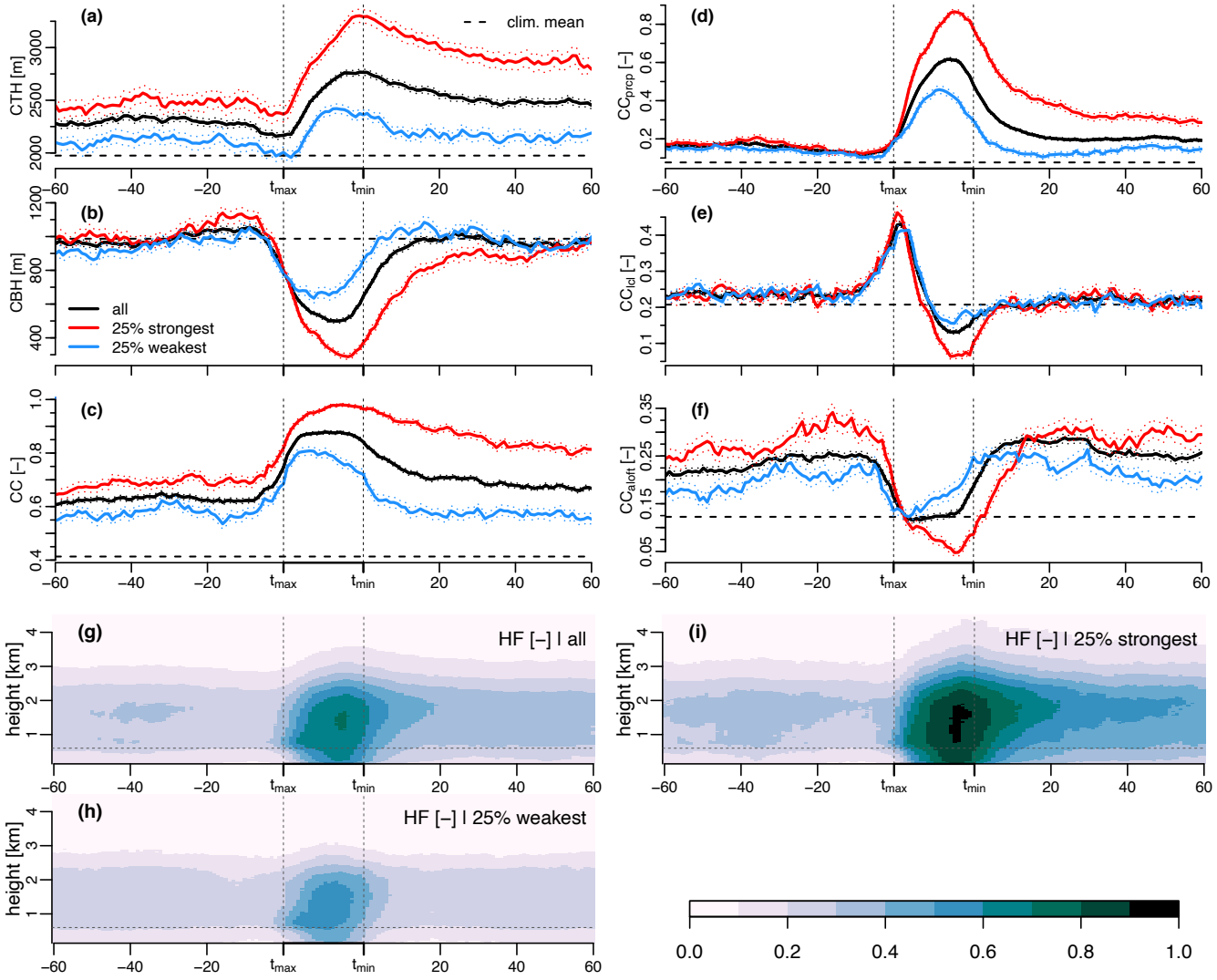

Figure 4. (a-f) Same as Figure 3, but for (a) cloud-top height, (b) cloud-base height, (c) total cloud cover, and the contribution to total cloud cover from (d) CC_{prcp}, (e) CC_{lcl} and (f) CC_{aloft}. Also indicated is the climatological mean value for the winter periods of 2012-2020. (g-i) Composite mean temporal structure of vertical hydrometeor fraction (HF) profiles for all *noprevWI* cold pools, as well as the 25% strongest and weakest. The thin dashed line at 600 m height marks the average cloud-base height.

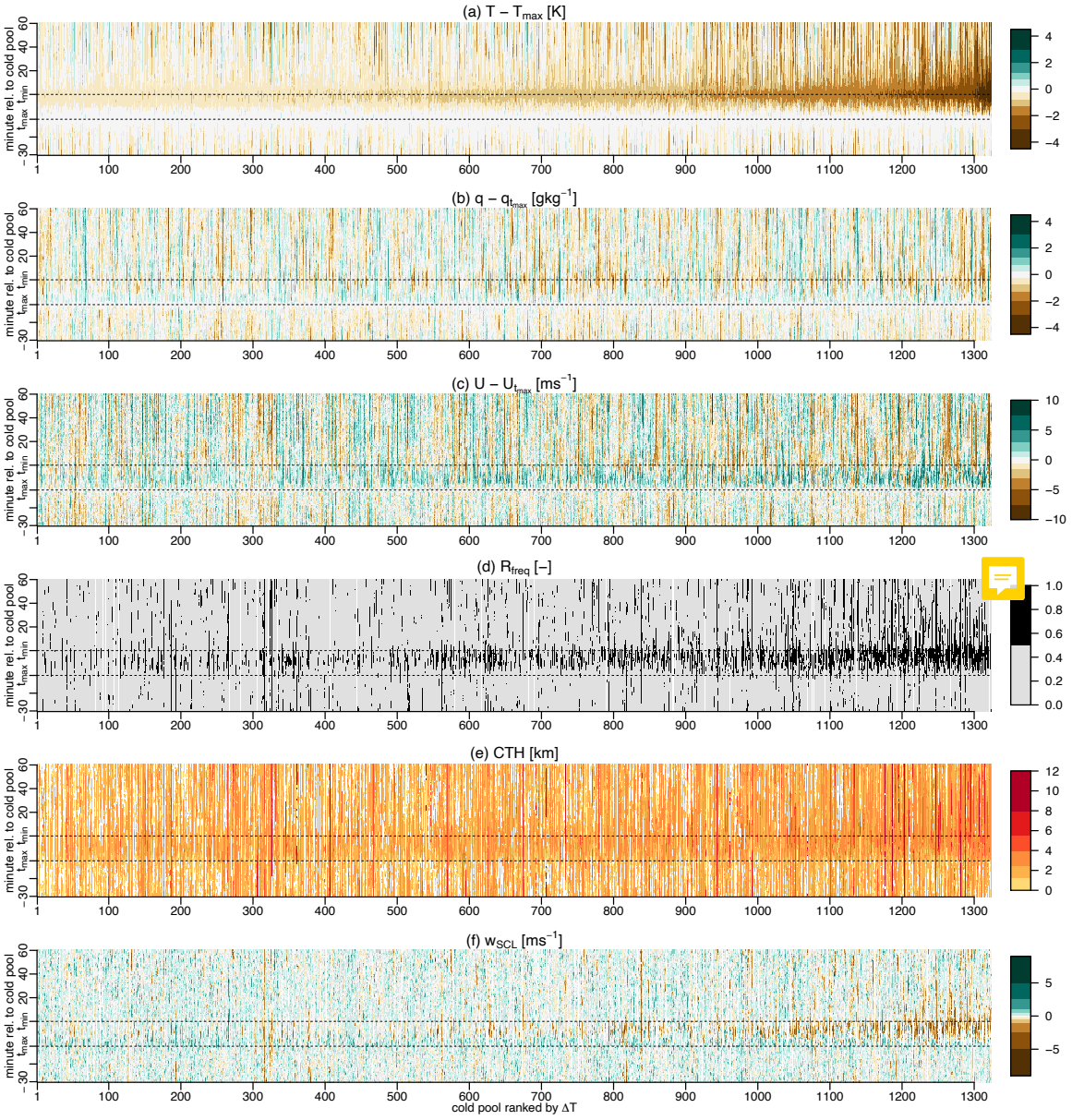

Figure 5. Temporal structure of individual cold pools ranked according to their ΔT. Shown are all cold pools of *noprevWI* that have all instruments running. The panels show anomalies relative to the cold-pool onset ($t_{\max}$) for (a) temperature, (b) specific humidity, and (c) wind speed, as well as absolute values of (d) the MRR rain frequency, (e) the cloud-top height, and (f) the vertical velocity averaged over the sub-cloud layer.

Figure 4a-f also indicate the respective mean CTH, CBH and CCs for all the winter months of the period 2012-2021. They show that cold-pool periods are much cloudier than the average winter trades. Cold-pool periods also have much deeper clouds, which is expected as ~~it needs~~ deeper precipitating clouds ~~to~~ form cold pools. The enhanced CC in the wake of cold

pools compared to the long-term mean is nevertheless surprising, as convection might be expected to be suppressed in the cold-pool wake. Mesoscale arcs encircling vast decks of deeper cumuli with stratiform layers therefore seem more representative for periods of cold-pool activity than the more classical picture of trade cumulus cold pools as mesoscale arcs enclosing broad clear-sky areas.

Despite the various significant differences between the strongest and weakest cold pools highlighted in the previous paragraphs, there is a lot of variability among individual cold pools. The variability is illustrated in Figure 5, which shows the temporal structure of the most important variables for individual cold pools ranked according to their ΔT. Especially the individual differences in humidity and wind in the front and the beginning of the wake can by far exceed the mean differences among the strongest and weakest cold pools shown in Figure 3. Tendencies of more frequent (and intense) rain, deeper clouds and stronger downdrafts near $t_{\min}$ of the stronger cold pools are nevertheless clearly evident. Especially the downdraft strength seems to be systematically increasing for stronger temperature drops. Besides showing the CTH, Figure 5e also gives an indication of the CC, again illustrating how cloudy the cold-pool periods are.

3.3 Daily cycle

The long timeseries also allows to study the variability of the cold-pool frequency and characteristics at the daily timescale. Figure 6 shows the ~~daily~~ variability of cold-pool properties for the *noprevWI* set. There are clearly fewer cold pools and a lower hourly cold-pool frequency between 16-22 LT compared to the rest of the day. Three local maxima in both the cold-pool frequency and number are present at 03, 09 and 14 LT. Also most cold-pool diagnostics show a pronounced daily variability. During nighttime between about midnight and 04 LT, cold pools are associated with significantly deeper clouds, stronger mean rain rates, stronger downdrafts and updrafts, larger CC, and slightly stronger humidity drops and weaker wind gusts compared to daytime cold pools between about 08-16 LT. There is also a hint of slightly stronger ΔT during nighttime compared to daytime, but neither in the median nor in the 25% quartiles is this daily cycle significant. It is somewhat surprising that we find no pronounced daily cycle in ΔT, ~~although~~ the daily cycle of e.g. w_{minSCL} and $CTH_{\max}$ ~~would suggest that ΔT should be stronger at nighttime compared to daytime~~. There is a climatological background daily cycle in temperature of about 1.2 K due to the daytime solar heating (minimum and maximum temperatures near 5 and 12 LT, respectively), but this should not affect the cloudy cold-pool periods much and would at best contribute to lower ΔT in the morning. Other diagnostics like $\Delta q_{\max}$ and R_{int} do not show a pronounced daily variability (not shown).

The pronounced daily variability in the cold-pool frequency and most diagnostics is not surprising given the distinct daily cycle in trade cumulus cloudiness discussed in detail in Vial et al. (2019) based on both high-resolution simulations and observations. The daily cycle of trade cumuli is characterized by larger CC and deeper clouds at the end of the night and smaller CC and shallower clouds in the afternoon. This is evident in the background climatological daily cycles indicated in Figure 6e-i. The daily cycles of most cold-pool diagnostics have a similar phase and also amplitude as their background daily cycles, but are shifted to much larger values (as indicated in the respective legends). For the vertical velocity diagnostics, also the amplitude of the daily cycle is much larger compared to the background climatology.

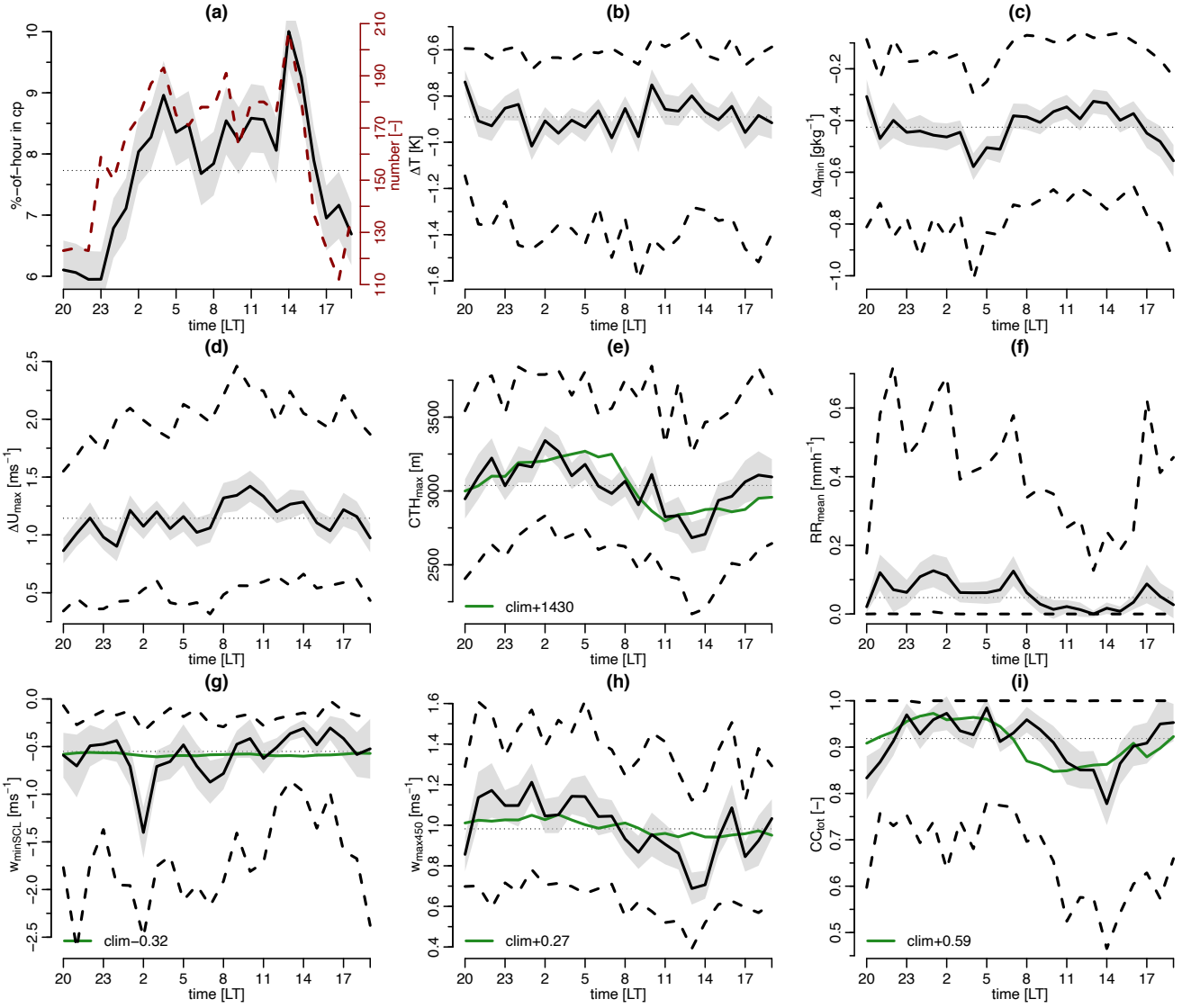

Figure 6. Daily cycles of important cold-pool diagnostics. (a) mean±1 SE of hourly cold-pool frequency as well as the number of cold pools per hour, (b) ΔT, (c) $\Delta q_{\min}$, (d) $\Delta U_{\max}$, (e) $CTH_{\max}$, (f) MRR RR_{mean}, (g) w_{minSCL} and (h) w_{max450}, and (i) CC_{tot}, with cold pools associated to a specific hour according to their $t_{\max}$. In panels b-i the lines represent the 25%, 50%, and the 75% quartiles of the respective variables and the shading represents the median±1 SE. Also indicated in green is the median climatological background daily cycle of 30-min values of (e) maximum CTH, (g) minimum w_{SCL}, (h) maximum w_{450}, and (i) mean CC, shifted by the mean difference of the climatological median compared to the cold-pool median to ease reading. Due to the infrequent rain, the median climatological RR_{mean} is always 0 and omitted in panel f.

395 The peaks in the cold-pool frequency at 09 and 14 LT are shifted by a few hours compared to the peak in the surface precipitation between 03-06 LT (Nuijens et al., 2009; Vial et al., 2019). This suggests that cold pools help extend the daily

cycle of shallow convection into the early afternoon, which could be due to cold pools reinforcing each other and triggering subsequent cold pools. This hypothesis is supported by the shorter median interval between subsequent cold pools of 121 min between 07-14 LT compared to 182 min between 22-04 LT. Also the daily cycle of cloud cover seems to be slightly extended into the morning, with CC_{tot} decreasing below the daily mean about 4 h later compared to the climatological CC.

Vial et al. (2021) also find the daily cycle of trade cumuli to be strongly linked to the daily cycle in the occurrence frequency of the mesoscale organization patterns. Whether the cold-pool characteristics and their daily cycles are related to the pattern of mesoscale organization will be discussed in the next section.

4 Relationship of cold-pool characteristics to mesoscale organization pattern

In this section we investigate whether the cold-pool frequency and characteristics depend on the pattern of mesoscale cloud organization. For this we condition the cold pools on the organization pattern present at BCO. As explained in Section 2.2, a pattern is attributed to a cold pool if it is present during $> 75\%$ of the cold-pool duration. As multiple patterns can be present at the same time, ~~a cold pool can pertain to two (or rarely even three) patterns.~~ Pattern labels are available from January 2018 to March 2021, and using the *noprevWI* criterion ~~we end up with~~ 1332 cold pools ~~to be~~ analysed.

The four example cold-pool days in Figure 2 already shed some light on the differences in the cold-pool characteristics of the four patterns. The two Sugar cold pools stem from isolated precipitating deeper cumuli. The satellite image captures the deeper cloud over BCO at the time of the first cold pool and also indicates some organization of the cumuli in lines upstream BCO, while the canonical Sugar fields of shallow cumuli pass further North.

The textbook Gravel day is characterized by many short and often weak cold pools quickly following each other, interspersed by stronger cold pools. The cold pools are associated with the presence of strongly precipitating deeper clouds (note that the radar did not work prior to 12 LT). The many cold pools present on this day clearly imprint their signature on the satellite image in the form of mesoscale arcs.

The cold pools on the Flowers day are associated with the large cloud system whose stratiform layer reaches the BCO at 10 LT. Three cold pools are directly associated with the large system, with the first one starting at 11 LT showing a very strong ΔT of -3.85 K. The large system has rain rates up to 3.6 mm h^{-1} and is announced by a weaker cold pool associated with the very thin mesoscale arc visible in the satellite image, which goes along with a strong increase in humidity of 1.3 g kg^{-1}.

The Fish day features a 6 h long cold pool associated with steady and intense rain (maximum RR of 11.6 mm h^{-1}), continued strong downdrafts and very large humidity throughout its entire duration. The temperature fully recovers within about 20 min of the cold-pool end, and 3 h later two subsequent pronounced cold pools follow that are again characterized by continued precipitation and downdrafts. The satellite image shows the fish-bone like cloud band typically associated with the Fish pattern. The occurrence of the Fish pattern is strongly connected to trailing cold fronts of extratropical origins (Aemisegger et al., 2021; Schulz et al., 2021). The more front-like character of the Fish cold pools with steady showers and downdrafts is clearly evident in the example timeseries.

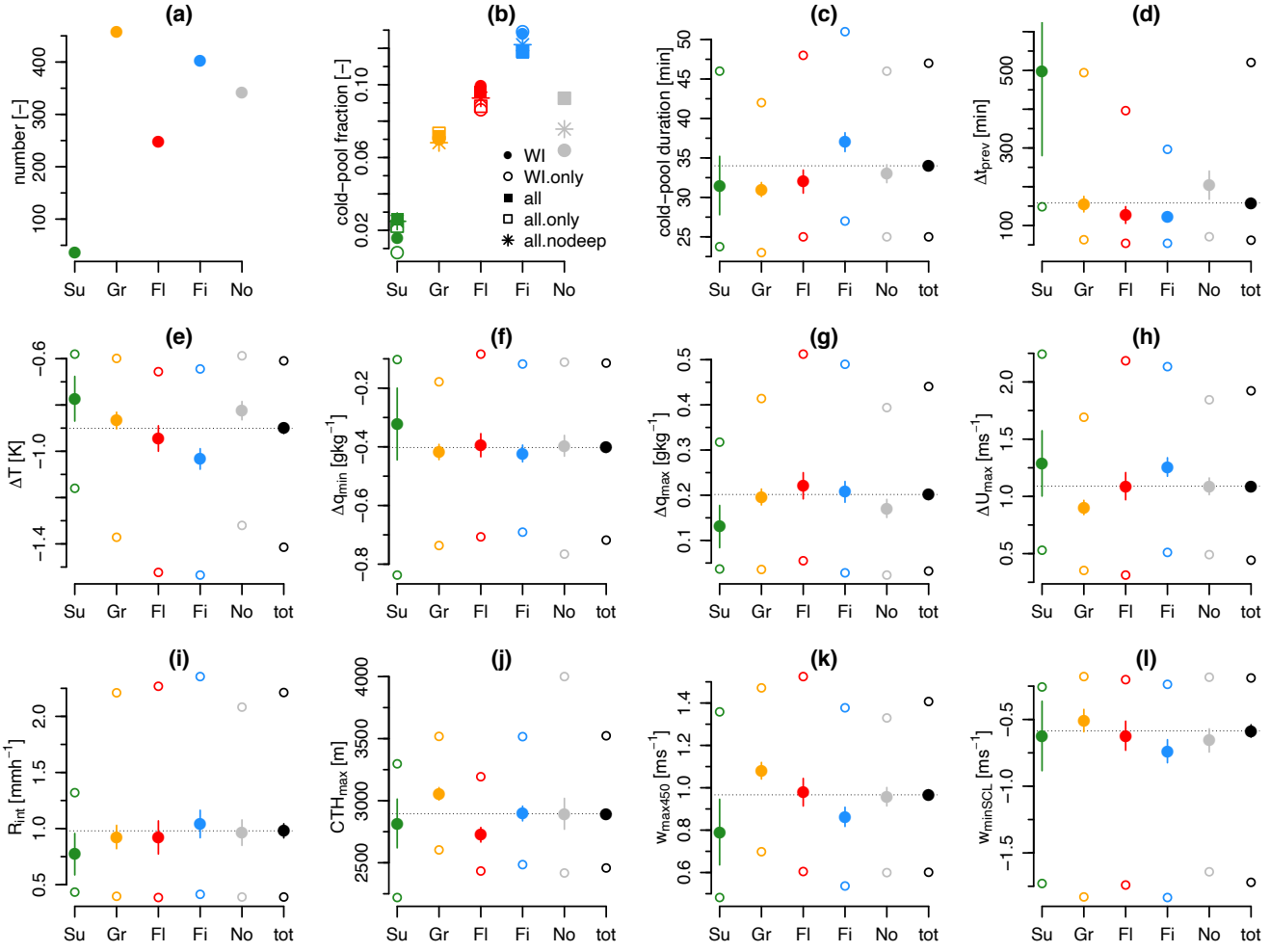

Figure 7. Distributions of various cold-pool diagnostics conditioned on the organization patterns. (a) Number of cold pools, (b) cold-pool fraction, (c) cold-pool duration, (d) time since $t_{\min}$ of the last cold pool, (e) ΔT, (f) $\Delta q_{\min}$, (g) $\Delta q_{\max}$, (h) $\Delta U_{\max}$, (i) MRR R_{int}, (j) $CTH_{\max}$, (k) $w_{\max 450}$ and (l) $w_{\min SCL}$. The different symbols in panels c-l represent the 25%, 50% and 75% quartiles of the respective variables, the solid lines represent the median$\pm$1 SE, and the dotted horizontal reference lines show the median of the entire set ('tot'). Besides the cold pools matching the *noprevWI* criterion, panel (b) also shows the fraction of cold pools for all seasons ('all'), for all seasons but without periods of deep convection ('all.nodeep'), and excluding periods with multiple organization patterns ('WI.only' and 'all.only').

Figure 7 shows distributions of several cold-pool properties for the different patterns, including the 'No' category and the union of the five categories ('tot'). The most pronounced difference among the patterns lies in the occurrence frequency of cold pools. Most cold pools detected at BCO pertain to the Gravel pattern (458), followed by Fish (402) and Flowers (248). As expected, only 36 cold pools are detected during Sugar periods. Many cold pools are also associated with the No category (341). When we look at the fraction of time a ~~given pattern is subject to a cold pool,~~ the picture changes and the Fish pattern is

associated with the largest cold-pool fraction (12.8% of time), followed by Flowers and Gravel (9.9% and 724%, respectively). Again, Sugar has clearly the lowest cold-pool fraction (1.6%).

Figure 7b also shows the cold-pool fractions using different selection criteria, namely that only one pattern is allowed at a time (*'.only'*; excluding cold pools ~~that pertain to~~ multiple patterns), that all *noprev* cold pools from all seasons are used (rather than only from the winter months; *'all'*), and that periods of deep convection in all seasons are excluded (*'all.nodeep'*; i.e. no cold pools with any radar signal between 4.5–8 km). For the Gravel pattern, these different criteria hardly influence the cold-pool fraction, whereas for Flowers and Sugar the different sets of criteria tend to change the cold-pool fraction. For Flowers, the cold-pool fraction in winter reduces to 8.6% if periods with multiple patterns and their cold pools are excluded. Only 85 cold pools are left for Flowers.only, while the rest are shared with Gravel (86), Fish (80) and a few also with Sugar (7). While excluding periods of multiple patterns more than halves the cold-pool fraction for Sugar (to 0.8%, mostly due to overlap with the Gravel pattern), considering all seasons nearly doubles the cold-pool fraction of Sugar. Despite these differences, the four patterns remain distinct in their cold-pool fractions independent of the criteria considered. The cold-pool fraction of the No category in winter is with 6.4% also substantial. The No category is particularly sensitive to the inclusion of all seasons, and in summer with more frequent deep convection most cold pools pertain to the No category (not shown). Excluding periods of deep clouds (*'all.nodeep'*) therefore mostly affects the No category, as deep convection is usually absent when patterns are detected.

That Gravel has the largest number of cold pools but only the third largest cold-pool fraction is partly due to Gravel being the most frequent pattern at BCO (a total of 178 days out of the 18 winter months considered, compared to 113 Fish, 78 Flowers and 72 Sugar days), and partly because Gravel cold pools on average last 6 min shorter than Fish cold pools (Figure 7c). ~~With a median duration of 37 min~~, Fish has the significantly longest-lasting cold pools of all patterns. Cold pools in the Fish ~~case~~ also follow each other most rapidly, with a median of 124 min separating individual cold pool fronts (Figure 7d). Also for Flowers and Gravel ~~do~~ cold pools follow each other quickly, whereas much more time passes between cold pools for Sugar and No. The same picture emerges when considering the cold-pool length (i.e. the duration multiplied by the surface wind speed): Fish cold pools are with a median size of 13.8 km slightly larger than Gravel and Flowers cold pools (both about 12.6 km, not shown).

Figure 7e-i show the differences in the surface meteorology, rain and cloud response associated with cold pools for the different patterns. Fish has the strongest median ΔT and the strongest downdrafts of all patterns, and also a stronger $\Delta U_{\max}$ compared to Gravel and Flowers. Gravel cold pools are associated with significantly larger $CTH_{\max}$ and stronger updrafts compared to the other patterns. For the humidity and rain diagnostics, the differences between Gravel, Flowers and Fish cold pools are minor. Sugar cold pools generally have the weakest cold-pool signatures. Contrastingly, the cold pools of the No category show no significant differences compared to Gravel, Fish and Flowers for most of the statistics.

If cold pools with multiple patterns are excluded, the strongest differences in the diagnostics occur for Flowers and Sugar, as their sample sizes become very small. For Flowers.only cold pools, $\Delta q_{\max}$ is significantly larger compared to the other patterns (not shown), and ΔT becomes comparable to the Fish and $w_{\max 450}$ comparable to Gravel cold pools. The Sugar.only cold-pool sample tends to have smaller cold-pool anomalies compared to when multiple patterns are allowed (except for the median $\Delta U_{\max}$ and $w_{\max 450}$), but the small sample of 11 Sugar.only cold pools does not allow for robust conclusions here. We

find similar differences in the cold-pool samples when the neural network agreement score is increased to 0.5 (instead of the default 0.4).

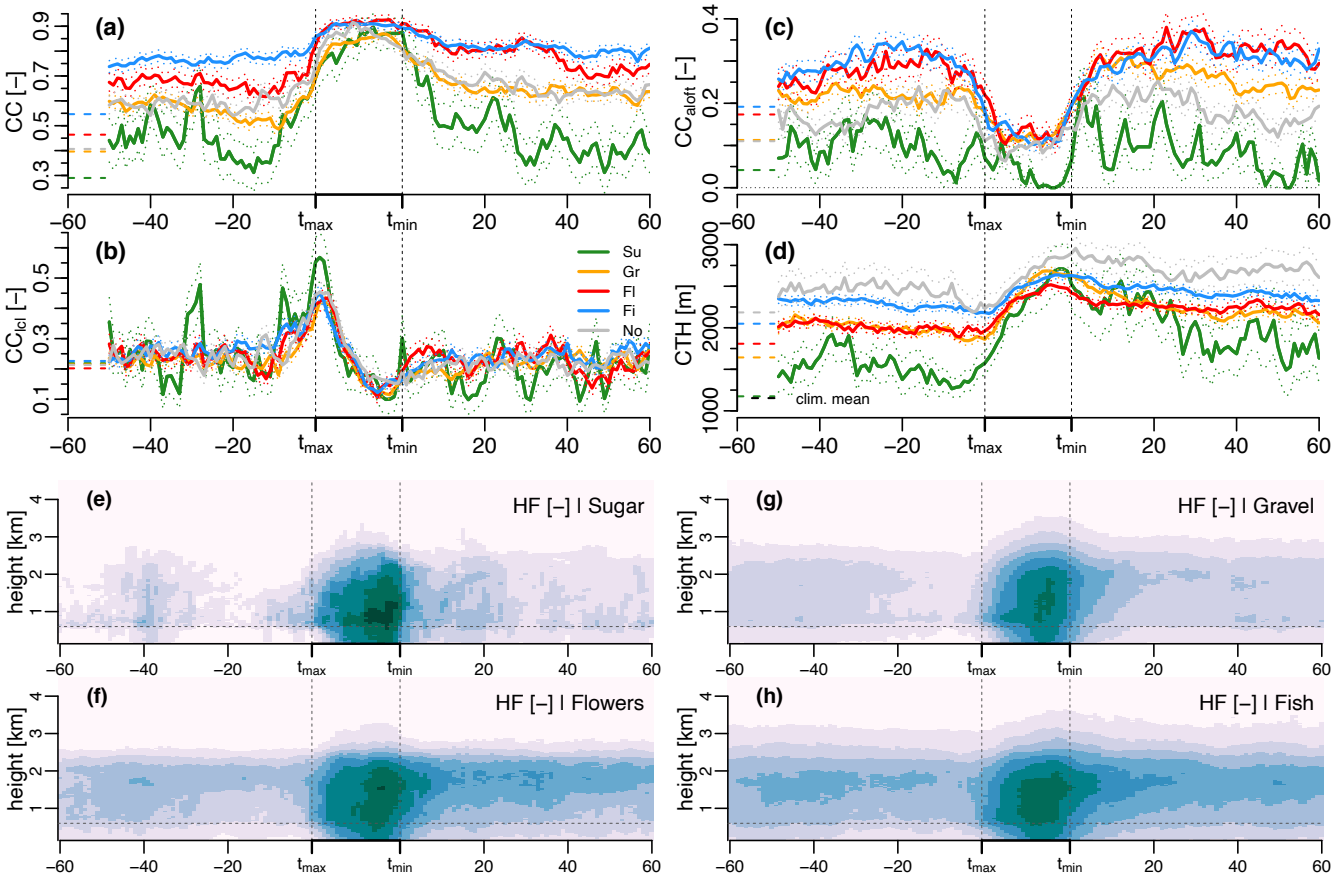

Figure 8. Composite mean temporal structure of the four organization patterns and the No category. Shown are (a) total CC, the contribution to total CC from (b) CC_{lcl} and (c) CC_{aloft}, and (d) the CTH. The dotted lines show the mean$\pm$1 SE. Also indicated on the far-left of panels a-d are the climatological mean values per pattern for the corresponding winter periods of 2018-2021. Panels e-h show the mean temporal structure of the vertical hydrometeor fraction profiles for the four patterns. The colour scale is the same as in Figure 4.

Figure 8a-d shows the differences in the temporal structures of cloud properties for the four patterns. They show that also during the cold-pool periods, the climatological differences in CC and CTH among the different patterns remain (see also Schulz et al., 2021; Vial et al., 2021; Bony et al., 2020). Fish has the largest CC, closely followed by Flowers[1], and then Gravel and Sugar. The CC differences are mostly due to the differing contributions of CC_{aloft}, whereas CC_{lcl} is fairly similar among the patterns both for the cold-pool periods and the climatological mean (Schulz et al., 2021). Also the temporal structure of

[1]Whether Fish or Flowers have the larger mean CC depends on the dataset and the period considered (Bony et al., 2020; Schulz et al., 2021; Vial et al., 2021)

CC_{prcp} is similar for all patterns during the cold-pool period (not shown), and resembles the mean structure of all cold pools shown in Figure 3d. For all patterns, the cold-pool periods are characterized by significantly deeper clouds and larger CC compared to the pattern average.

The CC of Fish cold pools hardly changes across the cold-pool passage, whereas the onset of the cold-pool front is much more clearly evident for the Gravel and even more for the Sugar CC. The CC in the wake of Sugar cold-pools also decreases most rapidly back to its pre-front value. Fish also tends to have the deepest mean CTH associated with the cold-pool periods, closely followed by Gravel and Flowers. The mean CTH of Gravel cold pools increases more rapidly in the front compared to Flowers and Fish, but also decreases a bit faster in the wake of the cold pools. Again, the cold-pool onset has the strongest CTH imprint for the Sugar pattern, with a mean CTH increase exceeding 1 km between t_{max} and t_{min}.

The differences in the cloud properties of the different patterns associated with the cold-pool passages are again summarized in the time-height composite hydrometeor fraction plots (Figure 8e-h). They show the strongly enhanced CC_{aloft} of Fish and Flowers cold pools that is mostly associated with more frequent stratiform layers near 1.5-2 km. The more pronounced influence of the cold-pool onset on the CC and CTH for Sugar and Gravel compared to Flowers and Fish, as well as the overall higher CTH for Fish are also clearly evident.

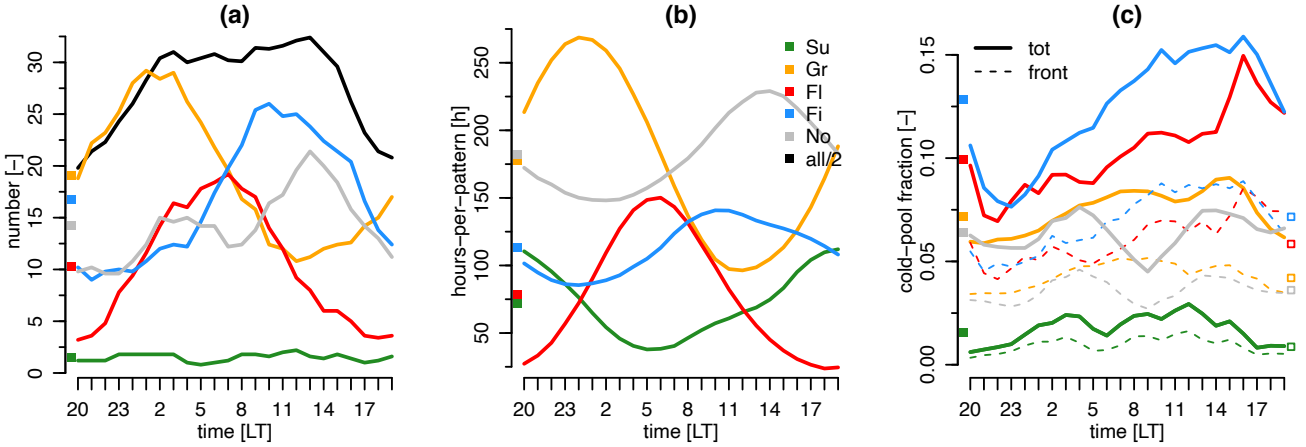

Figure 9. Daily cycles of (a) number of cold pools, (b) hours of data for the different organization patterns, and (c) hourly fraction in cold pool (solid) and in cold-pool front (dashed). A 5-hourly running mean is applied to smooth the data. The daily means are indicated on the left side of each panel.

As mentioned before, Vial et al. (2021) find the daily cycle of trade cumuli to be strongly linked to the daily cycle in the occurrence frequency of the mesoscale organization patterns. Figure 9a shows strong daily variations of the number of cold pools associated with the different patterns. These variations are strongly connected to the daily cycles in the occurrence frequency of the patterns (Figure 9b and Vial et al., 2021). The maximum number of Gravel cold pools occurs just after midnight, followed by Flowers around 7 LT, and Fish cold pools at 10 LT. The number of Sugar cold pools is very low throughout the day.

Figure 9a suggests that the extension of the daily cycle of convection into the early afternoon due to cold pools may largely be explained by the Fish pattern, together with a substantial contribution of the No category to the peak at 14 LT. Despite the strong connection between the daily phasings of Figure 9a-b, especially the Fish pattern also shows a daily cycle of the cold-pool fraction with a peak in the afternoon (Figure 9c), which is broadly in phase with the occurrence frequency. The daily cycle in the cold-pool fraction might be due to cold pools lasting a while once they are formed, which is supported by the much weaker daily cycles of the cold-pool *front* fraction (dashed lines in Figure 9c). Once present, cold pools often trigger new cold pools, as indicated by the 33% shorter interval between subsequent fronts during daytime compared to nighttime (see discussion in Section 3.3). From the present analyses, it is difficult to disentangle causal relationships between the pattern occurrence, cold pools, and the daily cycle. It is also difficult to pin down the evolution from one pattern to another, and the role of cold pools therein. As the number of cold pools per pattern and hour is quite low (especially in the case of Flowers), more data is needed to draw robust conclusions on this.

The pattern-associated daily phasing of the cold-pool number might give a clue about why ΔT varies little on the daily timescale (Figure 6c), although the daily cycle of most cold-pool properties would suggest that ΔT should be stronger at night compared to day. The daytime Fish pattern has significantly stronger ΔT compared to the nighttime Gravel pattern (Figure 7e), which might compensate for the opposite expectation due to the daily phasing of CTH_{max} and w_{minSCL}.

5 Conclusions

This paper presents a long-term climatology of trade cumulus cold pools based on more than ten years of in-situ and ground-based remote sensing data from the Barbados Cloud Observatory (BCO; Stevens et al., 2016). Cold pools are detected by abrupt drops in low-pass filtered temperature timeseries and their associated changes in surface meteorology, cloudiness and sub-cloud layer dynamics are extracted. The cold-pool climatology is combined with a neural network classification of the four mesoscale organization patterns Sugar, Gravel, Flowers and Fish (Stevens et al., 2020) based on GOES-16 ABI infrared images (Schulz et al., 2021). To focus on trade cumulus cold pools, most analyses are restricted to the set of 3889 cold pools detected in the dry winter regime from December to April that have no non-recovered cold pool in the hour prior to their onset.

We find cold pools to be ubiquitous in the winter trades—they are present about 7.8% of the time and on more than 73% of days at least one cold pool is detected. The average cold-pool passage is characterized by a 0.9 K temperature drop, a 0.2 g kg^{-1} humidity increase at the onset and a -0.4 g kg^{-1} humidity decrease at the end of the front, wind speed increases of 1.15 m s^{-1}, and rain intensities of 0.9 mm h^{-1}. The vertical velocity at the sub-cloud layer top shows a pronounced peak of 1 m s^{-1} near the cold-pool onset and sub-cloud layer averaged downdrafts of -0.55 m s^{-1} near the end of the front. Strong signals of cold-pool passages are also found for all cloud macrophysical properties analysed: cloud-top height increases, cloud-base height decreases (due to the very frequent precipitation), and cloud cover increases with the cold-pool onset. Cloudiness at the gust front is mostly due to cloud segments near the lifting-condensation level that pertain to larger precipitating cloud entities. Similarly, cloud segments with bases above 1 km in the cold-pool wake are mostly part of large precipitating clouds, and not from detached stratiform layers.

The strength of the cold-pool signature depends strongly on the intensity of the temperature drops (ΔT). Cold pools with stronger ΔT are associated with deeper clouds, stronger precipitation, downdrafts, and humidity drops, stronger wind gusts and updrafts at the edge of the front, and larger cloud cover compared to cold pools with weaker ΔT. Stronger cold pools also last significantly longer and follow each other more quickly than weaker cold pools. We find that also the minimum vertical velocity averaged over the sub-cloud layer and the maximum cloud-top height distinguish stronger and weaker cold pools very well. Especially the downdraft strength is a very robust indicator of cold-pool strength and together with the cold-pool front duration it explains 50% of the variability in ΔT.

The cold-pool frequency and characteristics also show pronounced daily variability. There are significantly less cold pools and a lower cold-pool frequency between 16-22 LT compared to the rest of the day. We find that cold pools extend the daily cycle of convection into the early afternoon, with a peak in both the cold-pool number and fraction at 14 LT. Also most cold-pool diagnostics show a pronounced daily cycle, with significantly deeper clouds, stronger mean rain rates, stronger downdrafts and updrafts, larger cloud cover, slightly stronger humidity drops and weaker wind gusts associated with nighttime compared to daytime cold pools. The phase of these daily signatures is consistent with their background climatological daily cycle, but shifted to much larger values. For the vertical velocity minima and maxima, also the amplitude of the daily cycle is much more pronounced during cold-pool periods.

In the wet summer regime, cold-pools are about 30% more frequent relative to the average winter regime. Summer cold pools are also associated with significantly stronger temperature and humidity drops, deeper clouds and stronger downdrafts—consistent with the frequent deep convection and stronger precipitation of this season (Brueck et al., 2015). On the other hand, the summer cold pools have weaker updrafts and humidity maxima at the beginning of the front, suggesting that they might be less effective in triggering new convection. While the temporal structure of cold-pool passages for most meteorological variables in both seasons resemble those of previous observations of tropical deep convective cold pools (de Szoeke et al., 2017; Chandra et al., 2018; Zuidema et al., 2017), especially the humidity structure and also the generally larger anomalies render the summer cold pools more similar to the deep convective cold pools from previous studies.

We also analysed if the cold-pool frequency and characteristics depend on the pattern of mesoscale cloud organization. The most pronounced difference among the patterns lies in the occurrence frequency of cold pools, with Fish having the largest cold-pool fraction (12.8% of time), followed by Flowers and Gravel (9.9% and 7.2%, respectively). As expected, the cold-pool fraction of Sugar is negligible (1.6%). Fish cold pools last significantly longer than cold pools from all the other patterns, and they are also associated with the strongest temperature drops and downdrafts. Gravel cold pools are associated with the strongest updrafts at the cold-pool onset and the deepest cloud-top height maxima.

Given the distinct daily cycle in the occurrence frequency of the four patterns found in Vial et al. (2021), it is not surprising that we find strong daily variations of the number of cold pools associated with the different patterns. The maximum number of Gravel cold pools occurs around midnight, followed by Flowers around 7 LT, and Fish cold pools around 10 LT, in line with the daily cycles in the occurrence frequency of the patterns. The Gravel, Flowers and Fish cold pools can thus explain a large fraction of the daily cycle in the cold-pool occurrence, as well as their extension into the early afternoon. Note also that the unclassified cold pools have a non-negligible contribution to the peak at 14 LT. Interestingly, the climatological differences in

the cloud cover and cloud-top height among the different patterns are also present during cold-pool periods—the overall cloud cover and cloud-top height for all patterns is just enhanced compared to their respective climatological values.

This study paves the way for more in-depth analyses of the cold-pool properties and their relation to the environment in the trades. Especially the complex humidity signals deserve a more detailed investigation, also using data from the recent EUREC^{4}A field campaign (Stevens et al., 2021) and from realistic large-eddy simulations. Together with the vertical velocity statistics, the humidity anomalies can help shed light on the triggering of new convection at the cold-pool front Additional measurements of the mixed-layer depth from radiosondes and the Raman or Doppler lidar could help refine the cold-pool end definition, which is only poorly constrained by the surface temperature data. Such additional data could also provide interesting insight into the cold-pool recovery process. A systematic matching with satellite imagery would also help collocate the clouds sampled at BCO with the broader view of the entire cold pool seen from space.

Overall, we find that the cold-pool periods are about 90% cloudier relative to the average winter trades. The larger cloudiness is mostly due to larger cloud cover from precipitating and stratiform cloud segments. Also the wake of cold pools is characterized by above average cloudiness, indicating that the classical image of trade cumulus cold pools as mesoscale arcs enclosing broad clear-sky areas is rather the exception than the rule. Our study suggests that a better understanding of how trade-cumulus cold pools interact with and shape their environment is important to understand the variability in cloud cover and cloud organization in the trade-wind regime.

Code and data availability. The BCO data used in the analysis and other supplementary information that may be useful to reproduce the present study are avalaible from the first author on request. The GOES-16 ABI data are publicly available online at doi.org/10.7289/V5BV7DSR. The satellite images in Figure 2 are retrieved from the imagery of the Earth Observing System Data and Information System (EOSDIS) Worldview Snapshots application (https://wvs.earthdata.nasa.gov, last access: 21 March 2021), and from the NASA ATOMIC-EUREC^{4}A GOES-16 ABI imagery (https://satcorps.larc.nasa.gov/cgi-bin/site/showdoc?docid=22&lkdomain=Y&domain=FEXP-ATOMIC-SATIMG, last access 21 March 2021).

Appendix A: Cloud cover contributions from different types of cloud entities

The contributions to total cloud cover from clouds at different height levels can either be computed by classifying every radar profile independently based on its CBH (see Figure 4d-f), or—if a cloud segmentation mask is available—by classifying the entire cloud entities according to their cbh_{ID} (i.e. their overall lowest CBH). As both approaches can provide valuable insights, Figure A1 also shows the temporal structure of the cold-pool signatures for the latter classification method. For this, the cloud cover is again split up into contributions from precipitating clouds with $cbh_{\mathrm{ID}} \leq 300\,\mathrm{m}$ ($CC_{\mathrm{ID.prcp}}$), LCL clouds ($CC_{\mathrm{ID.lcl}}$; $300\,\mathrm{m} < cbh_{\mathrm{ID}} \leq 1\,\mathrm{km}$), and stratiform clouds ($CC_{\mathrm{ID.aloft}}$; $1\,\mathrm{km} < cbh_{\mathrm{ID}} \leq 4\,\mathrm{km}$). The difference between $CC_{\mathrm{ID.prcp}}$ and CC_{prcp} is that edges or slanted sides of precipitating clouds that have a $CBH > 300\,\mathrm{m}$ are counted in their entirety to the $CC_{\mathrm{ID.prcp}}$ category, while they would be counted in the CC_{lcl} or CC_{aloft} category if the cloud ID was not considered. Due to

the potential presence of cloud entities at different heights, the sum of the three height categories ($CC_{\mathrm{ID.tot}}$) can be larger than one.

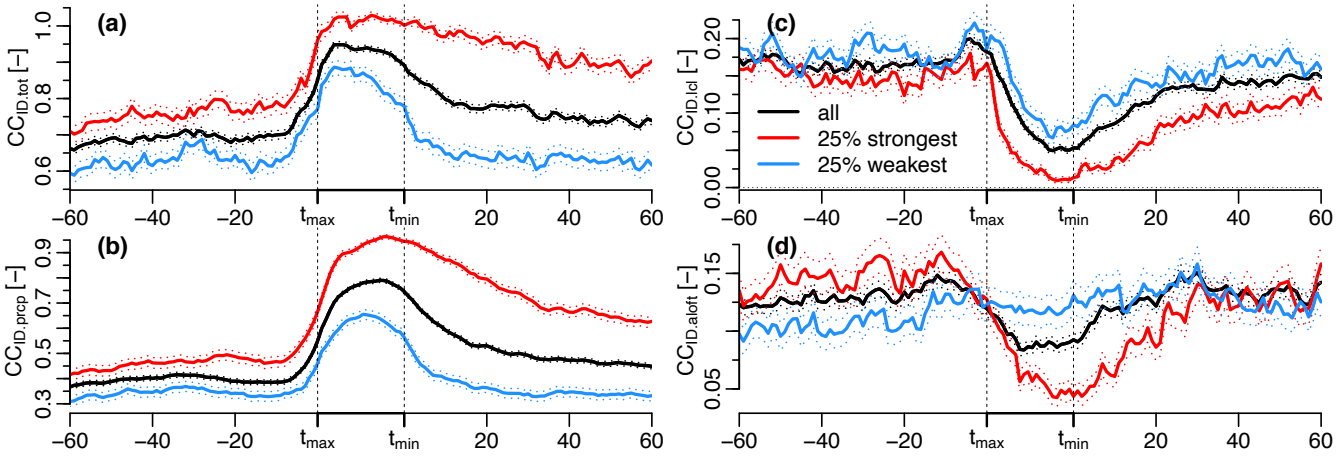

Figure A1. Same as Figure 3, but for (a) $CC_{\mathrm{ID.tot}}$, (b) $CC_{\mathrm{ID.prcp}}$, (c) $CC_{\mathrm{ID.lcl}}$, (d) $CC_{\mathrm{ID.aloft}}$, for all cold pools of *noprevWI* and the 25% strongest and weakest cold pools.

$CC_{\mathrm{ID.prcp}}$ already starts to increase before $t_{\max}$ and continues to increase until the middle of the front for all the cold-pool sets shown. For the 25% strongest cold pools, the end of the front is entirely covered by precipitating clouds. $CC_{\mathrm{ID.lcl}}$ in Figure A1c for all sets is relatively stable at about 17.5% before the cold-pool onset, decreases abruptly after $t_{\max}$ to a minimum near $t_{\min}$, and then slowly recovers back to the pre-front value. $CC_{\mathrm{ID.lcl}}$ shows the strongest impact when the cloud entities are considered through the cbh_{ID} and thus the strongest difference to the structure of CC_{lcl} (Figure 4e). The absence of a peak in $CC_{\mathrm{ID.lcl}}$ near $t_{\max}$ indicates that the CC_{lcl} peak there is almost entirely due to edges of precipitating clouds with a $CBH > 300$ m, and not due to (not-yet or) non-precipitating trade cumuli.

The temporal structure of $CC_{\mathrm{ID.aloft}}$ resembles the structure of CC_{aloft} (Figure 4f), yet with substantially lower coverage as most cloud segments with $CBH > 1$ km are connected to a precipitating core. This shows that nearly half of the CC_{aloft} in the cold-pool wake is part of large precipitating clouds, and not from detached stratiform layers.

Appendix B: Seasonal cycle of cold-pool characteristics

While this study focuses on the cold-pool climatology of the winter regime, it is also interesting to look at the seasonal cycle of the cold-pool characteristics at BCO. Using all cold pools of the *noprev* category, we find the largest median *%-of-day in cold pool* in the summer months from July-November, and another peak in January (Figure B1a). Only 13% of days have no cold pool at all in summer, compared to 27% in winter. The same monthly variability is found for the *%-of-day in front*, but with 45% lower values due to the shorter duration of the front compared to the entire cold pool (not shown).

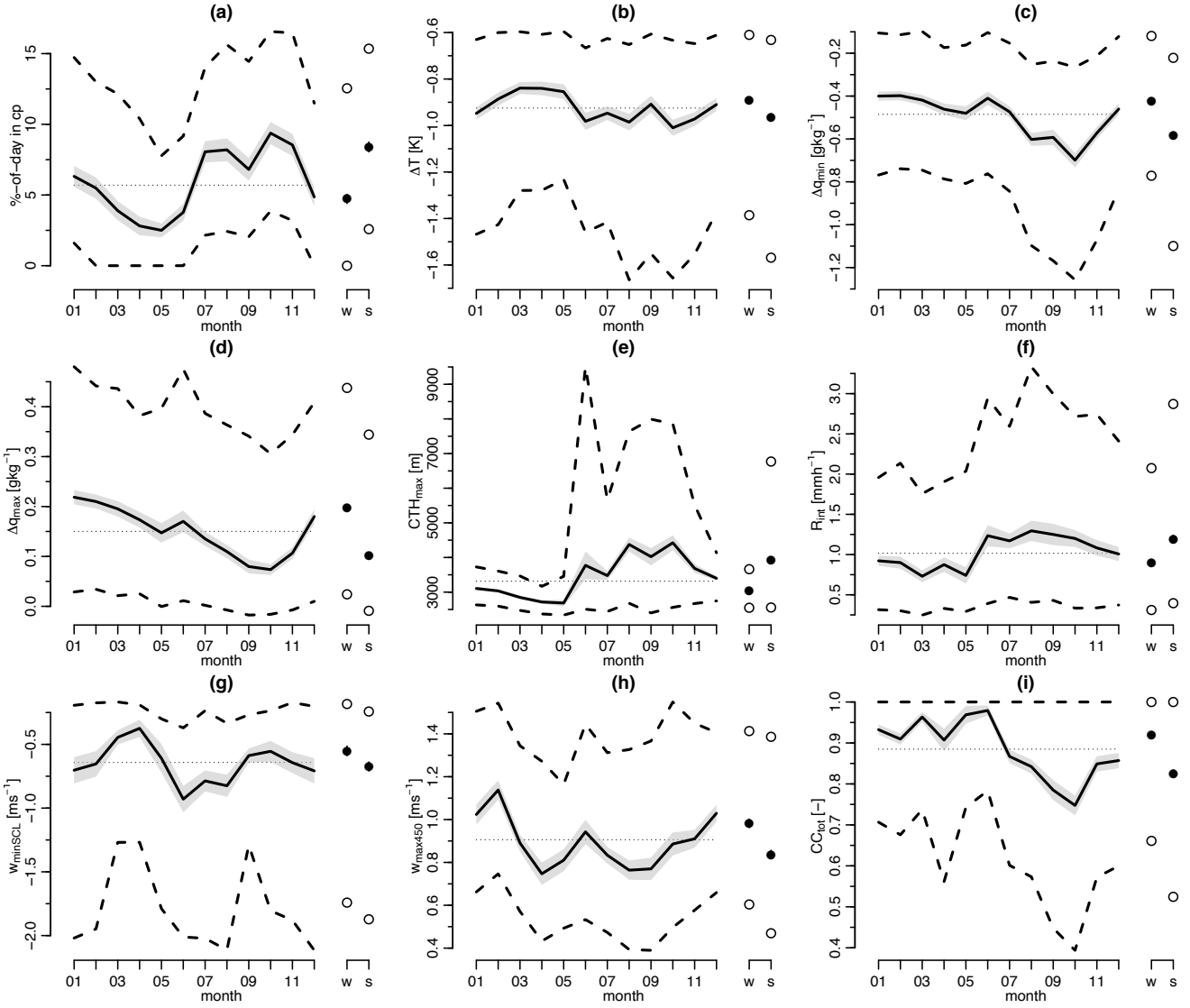

Figure B1. Monthly and seasonal distribution of important cold-pool diagnostics. (a) *%-of-day in cold-pool*, (b) ΔT, (c) $\Delta q_{\min}$, (d) $\Delta q_{\max}$, (e) $CTH_{\max}$, (f) MRR R_{int}, (g) w_{minSCL} and (h) w_{max450}, and (i) CC_{tot}. The lines represent the 25%, 50%, and the 75% quartiles of the respective variables, the shading represents the median$\pm$1 SE, and the points show the average distribution for the five winter (w; December-April) and summer months (s; July-November).

Figure B1b-i show the monthly distributions of various cold-pool properties, as well as averages over the five winter and summer months, respectively. They show that the summer cold pools are on average characterized by significantly stronger $\Delta q_{\min}$, $CTH_{\max}$ and R_{int}, as well as slightly stronger ΔT and w_{minSCL}, consistent with the relationships discussed in Section 3. However, w_{max450} is significantly lower by 0.2 m s^{-1} and $\Delta q_{\max}$ by 0.1 g kg^{-1} in summer compared to winter, indicating that cold pools in summer might be less successful in triggering new convection. Furthermore, CC_{tot} of summer cold pools

is also significantly smaller compared to winter cold pools by about 10%. The differences in the cold-pool characteristics between the summer and winter regime are not surprising, as the summer regime is referred to as the *wet* season in Barbados and characterized by frequent deep convection and much larger precipitation (Brueck et al., 2015). When excluding periods of deep convection (defined by the presence of a radar signal between 4.5–8 km), the number of cold pools detected in summer strongly decreases compared to winter, and the median summer cold pool also becomes weaker compared to the median winter cold pool (not shown).

Author contributions. RV initiated the project in exchange with PZ. HK prepared the radar cloud mask and HS the neural network classifications of the organization patterns. RV developed the cold-pool detection algorithm, performed the analyses and wrote the manuscript. All co-authors contributed to the interpretation of the results and commented on the manuscript.

Competing interests. The authors declare that they have no conflict of interest.

Disclaimer. TEXT

Acknowledgements. Many thanks go to the Tropical Cloud Observation group at MPI for maintaining the BCO infrastructure. We thank Nicolas Rochetin, Ludovic Touzé-Pfeiffer, Cathy Hohenegger, Bjorn Stevens, and the EUREC^{4}A science team at LMD and MPI for interesting discussions. RV thanks Louise Nuijens for motivating to look at cold pools at end of the PhD thesis. RV acknowledges funding from the European Research Council (ERC) under the European Union's Horizon 2020 research and innovation programme (grant agreement No 694768). HK has received funding from HALO SPP (DFG HALO SPP 1294). PZ acknowledges support from NOAA Climate Program Office award NA19OAR4310379.

References

Aemisegger, F., Vogel, R., Graf, P., Dahinden, F., Villiger, L., Jansen, F., Bony, S., Stevens, B., and Wernli, H.: How Rossby wave breaking modulates the water cycle in the North Atlantic trade wind region, Weather and Climate Dynamics, 2, 281–309, https://doi.org/10.5194/wcd-2-281-2021, 2021.

Barnes, G. M. and Garstang, M.: Subcloud layer energetics of precipitating convection, Mon. Wea. Rev., 110, 102–117, 1982.

Bony, S. and Dufresne, J.-L.: Marine boundary layer clouds at the heart of tropical cloud feedback uncertainties in climate models, Geophys. Res. Lett., 32, L20 806, https://doi.org/10.1029/2005GL023851, 2005.

Bony, S., Stevens, B., Ament, F., Bigorre, S., Chazette, P., Crewell, S., Delanoë, J., Emanuel, K., Farrell, D., Flamant, C., Gross, S., Hirsch, L., Karstensen, J., Mayer, B., Nuijens, L., Ruppert, J. H., Sandu, I., Siebesma, P., Speich, S., Szczap, F., Totems, J., Vogel, R., Wendisch, M., and Wirth, M.: EUREC4A: A Field Campaign to Elucidate the Couplings Between Clouds, Convection and Circulation, Surveys in Geophysics, https://doi.org/10.1007/s10712-017-9428-0, 2017.

Bony, S., Schulz, H., Vial, J., and Stevens, B.: Sugar, Gravel, Fish, and Flowers: Dependence of Mesoscale Patterns of Trade-Wind Clouds on Environmental Conditions, Geophysical Research Letters, 47, e2019GL085 988, https://doi.org/10.1029/2019GL085988, 2020.

Brueck, M., Nuijens, L., and Stevens, B.: On the seasonal and synoptic time-scale variability of the north atlantic trade wind region and its low-level clouds, J. Atmos. Sci., 72, 1428–1446, https://doi.org/10.1175/JAS-D-14-0054.1, 2015.

Byers, H. R. and Hall, R. K.: A census of cumulus-cloud height versus precipitation in the vicinity of Puerto Rico during the winter and spring of 1953-1954, Journal of the Atmospheric Sciences, 12, 176–178, https://doi.org/10.1175/1520-0469(1955)012<0176:ACOCCH>2.0.CO;2, 1955.

Chandra, A. S., Zuidema, P., Krueger, S., Kochanski, A., de Szoeke, S. P., and Zhang, J.: Moisture Distributions in Tropical Cold Pools From Equatorial Indian Ocean Observations and Cloud-Resolving Simulations, Journal of Geophysical Research: Atmospheres, 123, 11,445–11,465, https://doi.org/10.1029/2018JD028634, 2018.

de Szoeke, S. P., Skyllingstad, E. D., Zuidema, P., and Chandra, A. S.: Cold Pools and Their Influence on the Tropical Marine Boundary Layer, Journal of the Atmospheric Sciences, 74, 1149 – 1168, https://doi.org/10.1175/JAS-D-16-0264.1, 2017.

Feng, Z., Hagos, S., Rowe, A. K., Burleyson, C. D., Martini, M. N., and de Szoeke, S. P.: Mechanisms of convective cloud organization by cold pools over tropical warm ocean during the AMIE/DYNAMO field campaign, Journal of Advances in Modeling Earth Systems, 7, 357–381, https://doi.org/https://doi.org/10.1002/2014MS000384, 2015.

GOES-R Calibration Working Group and GOES-R Series Program: NOAA GOES-R Series Advanced Baseline Imager (ABI) Level 1b Radiances, https://doi.org/10.7289/V5BV7DSR, online; accessed on 15 July 2020, 2017.

Klingebiel, M., Ghate, V. P., Naumann, A. K., Ditas, F., Pöhlker, M. L., Pöhlker, C., Kandler, K., Konow, H., and Stevens, B.: Remote Sensing of Sea Salt Aerosol below Trade Wind Clouds, Journal of the Atmospheric Sciences, 76, 1189 – 1202, https://doi.org/10.1175/JAS-D-18-0139.1, 2019.

Konow, H.: BCO Cloudmask Code, https://doi.org/10.5281/zenodo.4312818, 2020.

Kubar, T. L., Hartmann, D. L., and Wood, R.: Understanding the Importance of Microphysics and Macrophysics for Warm Rain in Marine Low Clouds. Part I: Satellite Observations, Journal of the Atmospheric Sciences, 66, 2953–2972, https://doi.org/10.1175/2009JAS3071.1, 2009.

Langhans, W. and Romps, D. M.: The origin of water vapor rings in tropical oceanic cold pools, Geophysical Research Letters, 42, 7825–7834, 2015.

Lin, T., Goyal, P., Girshick, R. B., He, K., and Dollár, P.: Focal Loss for Dense Object Detection, CoRR, abs/1708.02002, http://arxiv.org/abs/1708.02002, 2017.

Medeiros, B. and Nuijens, L.: Clouds at Barbados are representative of clouds across the trade wind regions in observations and climate models, Proceedings of the National Academy of Sciences, 113, E3062–E3070, https://doi.org/10.1073/pnas.1521494113, 2016.

Nuijens, L., Stevens, B., and Siebesma, A. P.: The environment of precipitating shallow cumulus convection, J. Atmos. Sci., 66, 1962–1979, 2009.

Nuijens, L., Serikov, I., Hirsch, L., Lonitz, K., and Stevens, B.: The distribution and variability of low-level cloud in the North Atlantic trades, Quart. J. Roy.Meteor.Soc., 140, 2364–2374, https://doi.org/10.1002/qj.2307, 2014.

Rasp, S., Schulz, H., Bony, S., and Stevens, B.: Combining Crowdsourcing and Deep Learning to Explore the Mesoscale Organization of Shallow Convection, Bulletin of the American Meteorological Society, 101, E1980–E1995, https://doi.org/10.1175/BAMS-D-19-0324.1, 2020.

Rochetin, N., Hohenegger, C., Touzé-Peiffer, L., and Villafranque, N.: A physically-based robust definition of convectively generated density currents: detection and characterization in convection-permitting simulations, submitted to JAMES, 2021.

Rowe, A. K. and Houze Jr., R. A.: Cloud organization and growth during the transition from suppressed to active MJO conditions, Journal of Geophysical Research: Atmospheres, 120, 10,324–10,350, https://doi.org/10.1002/2014JD022948, 2015.

Schlemmer, L. and Hohenegger, C.: The Formation of Wider and Deeper Clouds as a Result of Cold-Pool Dynamics, J. Atmos. Sci., 71, 2842–2858, https://doi.org/10.1175/JAS-D-13-0170.1, 2014.

Schulz, H., Eastman, R. M., and Stevens, B.: Characterization and Evolution of Organized Shallow Convection in the Trades, https://doi.org/10.1002/essoar.10505836.1, 2021.

Stevens, B., Farrell, D., Hirsch, L., Jansen, F., Nuijens, L., Serikov, I., Brügmann, B., Forde, M., Linne, H., Lonitz, K., and Prospero, J. M.: The Barbados Cloud Observatory: Anchoring Investigations of Clouds and Circulation on the Edge of the ITCZ, Bulletin of the American Meteorological Society, 97, 787–801, https://doi.org/10.1175/BAMS-D-14-00247.1, 2016.

Stevens, B., Satoh, M., Auger, L., Biercamp, J., Bretherton, C. S., Chen, X., Düben, P., Judt, F., Khairoutdinov, M., Klocke, D., Kodama, C., Kornblueh, L., Lin, S.-J., Neumann, P., Putman, W. M., Röber, N., Shibuya, R., Vanniere, B., Vidale, P. L., Wedi, N., and Zhou, L.: DYAMOND: the DYnamics of the Atmospheric general circulation Modeled On Non-hydrostatic Domains, Progress in Earth and Planetary Science, https://doi.org/10, 2019.

Stevens, B., Bony, S., Brogniez, H., Hentgen, L., Hohenegger, C., Kiemle, C., L'Ecuyer, T. S., Naumann, A. K., Schulz, H., Siebesma, P. A., Vial, J., Winker, D. M., and Zuidema, P.: Sugar, gravel, fish and flowers: Mesoscale cloud patterns in the trade winds, Quarterly Journal of the Royal Meteorological Society, 146, 141–152, https://doi.org/10.1002/qj.3662, 2020.

Stevens, B., Bony, S., and Farrell, D. e. a.: EUREC^{4}A, Earth System Science Data Discussions, 2021, 1–78, https://doi.org/10.5194/essd-2021-18, 2021.

Tompkins, A. M.: Organization of Tropical Convection in Low Vertical Wind Shears: The Role of Cold Pools, J. Atmos. Sci., 58, 1650–1672, https://doi.org/10.1175/1520-0469(2001)058<0529:OOTCIL>2.0.CO;2, 2001.

Torri, G. and Kuang, Z.: Rain evaporation and moist patches in tropical boundary layers, Geophys. Res. Lett., 43, 9895–9902, 2016.

Touzè-Peiffer, L., Vogel, R., and Rochetin, N.: Detecting cold pools from soundings during EUREC4A, https://arxiv.org/abs/2104.09146, 2021.

Vial, J., Dufresne, J. L., and Bony, S.: On the interpretation of inter-model spread in CMIP5 climate sensitivity estimates, Clim. Dyn., pp. 3339–3362, https://doi.org/10.1007/s00382-013-1725-9, 2013.

Vial, J., Vogel, R., Bony, S., Stevens, B., Winker, D. M., Cai, X., Hohenegger, C., Naumann, A. K., and Brogniez, H.: A New Look at the Daily Cycle of Trade Wind Cumuli, Journal of Advances in Modeling Earth Systems, 11, 3148–3166, https://doi.org/10.1029/2019MS001746, 2019.

Vial, J., Vogel, R., and Schulz, H.: On the daily cycle of mesoscale cloud organization in the winter trades, accepted for *QJRMS*, 2021.

Vogel, R.: The influence of precipitation and convective organization on the structure of the trades (Doctoral dissertation, Universität Hamburg), Berichte zur Erdsystemforschung, https://doi.org/10.17617/2.2503092, 2017.

Young, G. S., Perugini, S. M., and Fairall, C. W.: Convective Wakes in the Equatorial Western Pacific during TOGA, Monthly Weather Review, 123, 110, https://doi.org/10.1175/1520-0493(1995)123<0110:CWITEW>2.0.CO;2, 1995.

Zuidema, P., Li, Z., Hill, R. J., Bariteau, L., Rilling, B., Fairall, C., Brewer, W. A., Albrecht, B., and Hare, J.: On Trade Wind Cumulus Cold Pools, J. Atmos. Sci., 69, 258–280, https://doi.org/10.1175/JAS-D-11-0143.1, 2012.

Zuidema, P., Torri, G., Muller, C., and Chandra, A.: A Survey of Precipitation-Induced Atmospheric Cold Pools over Oceans and Their Interactions with the Larger-Scale Environment, Surveys in Geophysics, https://doi.org/10.1007/s10712-017-9447-x, 2017.